Studies on TiO_2 Photocatalysis for C–C Bond Formation

Shimpei Naniwa

Preface

Over the past few decades, the world has experienced a dramatic growth of the economy with the development in technology. At the same time, the growth brought out some serious problems in the environment such as air and water pollution and global warming. Technology, as a cause of the economic growth, should, and is expected to give a solution to these problems. Photocatalysis is one such technology, which allows conversions of various chemical substances under mild conditions by utilizing light energy, or more favorable, by using sunlight. The present work is devoted to studies on photocatalysis over TiO_2 for C–C bond formation for the development and understanding of the photocatalysis. The work was conducted in the Graduate School of Human and Environmental Studies, Kyoto University, Japan under the supervision of Prof. Hisao Yoshida.

The author expresses his sincere gratitude to Prof. Hisao Yoshida for his invitation to the field of photocatalysis, constant support and insightful comments, and kindness to allow me to do my research. The author is also grateful to Dr. Akira Yamamoto, assistant professor in Hisao Yoshida laboratory, for his accurate advice, valuable discussions, and continuous encouragement. Deep appreciation to Prof. Akira Yamakata and Dr. Kosaku Kato at Toyota Technological Institute for transient absorption measurements. Thanks should also be made to Prof. Ken-ichi Fujita and his laboratory members for helping to synthesize specific compounds. Heartfelt thanks to Dr. Tsutomu Kiyomura at Kyoto University for technical assistance with the TEM measurements.

Many thanks to Ms. Yuri Bonnitcha, secretary in Hisao Yoshida laboratory for her kind aids in official affairs. Special thanks to seniors of Hisao Yoshida laboratory, Dr. Akanksha Tyagi, Dr. Emiko Wada, Mr. Tomoya Matsumoto, Mr. Tomoyuki Ohara for their help in my early carrier. The author also thanks his colleagues, Dr. Akihiko Anzai, Mr. Surya Puratap Singh, and Mr. Wirya Sarwana, Mr. Daichi Takami, and Mr. Yuuki Kitagawa for their friendship and sharing difficulty and pleasure of research and to all of the members in the laboratory for providing a healthy and comfortable environment all these years.

Finally, the author shows his deep gratitude to his parents, brothers, and Ms. Saki Kuze for their encouragement and understanding. This whole journey would be impossible without their encouragement and understanding.

This thesis is a conclusion of the author's journey over nine years at Kyoto University. However, this is not the end but just the beginning of a new journey toward his dream.

Shimpei Naniwa
31st January, 2022
Kyoto, Japan

CONTENTS

General Introduction

Titanium dioxide (TiO_2) is one of the most practical photocatalysts with high performance and low cost. Photocatalysis over TiO_2 is first discovered by Honda and Fujishima, who studied photoelectrochemical water splitting into hydrogen and oxygen using a TiO_2 photoanode with an external bias.[1] This is called the Honda Fujishima effect. The discovery of the Honda Fujishima effect opened a new field of chemistry, that is, photocatalysis, and triggered a great number of successive studies. As a result, a variety of photocatalytic materials has been developed and now the application of photocatalysis has been extended to various chemical processes such as self-cleaning,[2,3] purification of water and air,[3–12] artificial photosynthesis,[13,14,23,24,15–22] and organic synthesis.[25–31] Nevertheless, TiO_2, the first semiconductor photocatalyst, still gains much interest as both a promising material for applied research and standard material for fundamental research, as is evident in the increasing annual number of related research papers year by year (Figure 1).

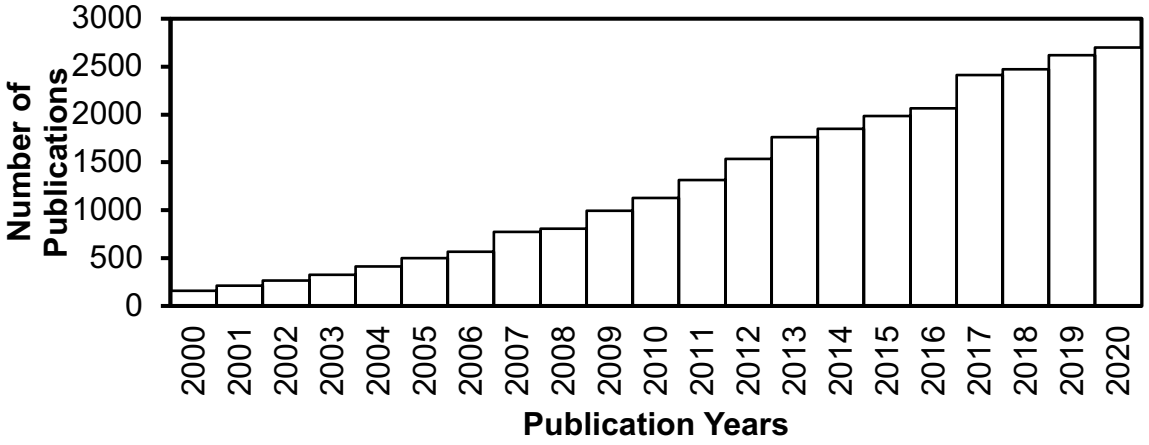

Figure 1 Number of publications per year related to TiO_2 photocatalysis in the past two decades. The data was taken from a web of science search by "TiO_2 photocatalysis" on November 1, 2021.

The high photocatalytic performance of TiO_2 photocatalysts arises from its strong oxidation ability. In typical photocatalysis, irradiation of light of which energy equals or exceeds the bandgap energy of the photocatalyst excites an electron (e^-) in the valence band (V.B.) to the conduction band (C.B.) (Figure 2). As a result, the valence band has a positive charge, which is called hole (h^+). These photogenerated electron and hole migrate to the surface of the photocatalyst and reduce or oxidize reactants to drive photocatalysis. The reducing power of the electrons and oxidizing power of the holes depend on the band edge positions;

the higher the conduction band bottom edge, the higher reducing power electrons have, and the lower the valence band top edge, the higher oxidation power the holes have. In TiO_2, the holes have strong oxidation ability because of the deep position of the valence band edge, which can oxidize most organic molecules. Consequently, TiO_2 photocatalysis had been applied mainly to the degradation of pollutants for many years.[11,32] Recently, the advantage of this strong oxidation ability has started to manifest in synthetic use.[33–35] Coupling reactions are one of the striking examples. The strong oxidation ability of TiO_2 allows direct activation of inert chemical bonds such as C–H bond.[36–38] Therefore, coupling of organic molecules to form a C–C bond is possible under mild conditions without using harmful additives. This is a promising green approach to constructing organic molecules.

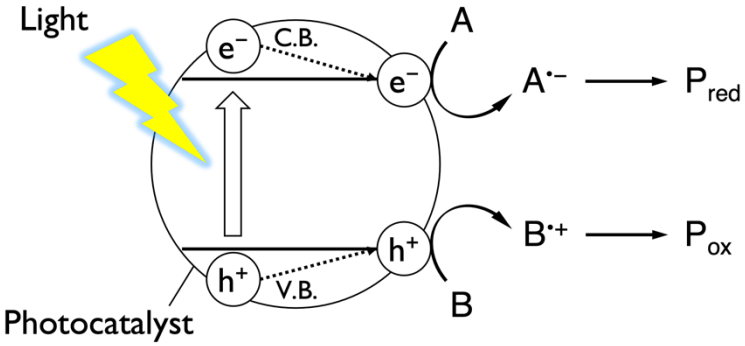

Figure 2 A schematic image of the mechanism of typical photocatalysis. A and B are reactant molecules and P_{red} and P_{ox} are reduction and oxidation products, respectively.

Application of TiO_2 photocatalysis to C–C bond formation in a synthetic manner faces several issues which must be overcome. One of the issues is its low selectivity. As mentioned above, the strong oxidation ability allows direct activation of stable chemical bonds. However, it also leads to random oxidation of the reactants, making the reaction unselective. This inhibits the application of TiO_2 photocatalysis to synthetic C–C bond formation. Another critical issue is a lack of quantitative understanding of the relationship between the activity of photocatalysts and structural and physicochemical parameters. Most studies on the relationship have been made in a qualitative manner, in which the effect of each parameter on the activity is discussed individually. This cannot be a valid approach to understand the structure-property-activity relationship comprehensively when considering a variety of activity-controlling factors of photocatalysis as well as their correlation and interdependency. In this thesis, we attacked these two issues.

In Part I, we developed a series of selective C–C bond formation reactions utilizing a new style of photocatalysis, the surface complex system. The system utilizes ligand-to-metal

charge transfer (LMCT) surface complex on TiO_2 to achieve selective C–C bond formation under visible light irradiation. In Part II, we studied the structure-property and property-activity relationship. We first carried out time-resolved visible-to-midIR absorption spectroscopy to investigate the relationship between specific surface area and the energy states and dynamics of photogenerated carriers in TiO_2, both of which are important factors of the activity of the photocatalysts. We next studied the relationship of these factors to photocatalytic activity in a quantitative manner using a statistical approach based on a simple kinetic model. This thesis showed the potential of the surface complex system for selective C–C bond formation by TiO_2 photocatalysis and proposed a quantitative approach to study the structure-property-activity relationship in photocatalysis.

References

1. Fujishima, A. & Honda, K. Electrochemical Photolysis of Water at a Semiconductor Electrode. *Nature* **238**, 37–38 (1972).
2. Zhang, L., Dillert, R., Bahnemann, D. & Vormoor, M. Photo-induced hydrophilicity and self-cleaning: Models and reality. *Energy Environ. Sci.* **5**, 7491–7507 (2012).
3. Devi, L. G. & Kavitha, R. A review on non metal ion doped titania for the photocatalytic degradation of organic pollutants under UV/solar light: Role of photogenerated charge carrier dynamics in enhancing the activity. *Appl. Catal. B Environ.* **140**–**141**, 559–587 (2013).
4. Herrmann, J. M. Heterogeneous photocatalysis: State of the art and present applications. *Top. Catal.* **34**, 49–65 (2005).
5. Nakata, K. & Fujishima, A. TiO_2 photocatalysis: Design and applications. *J. Photochem. Photobiol. C Photochem. Rev.* **13**, 169–189 (2012).
6. Dong, H. *et al.* An overview on limitations of TiO_2-based particles for photocatalytic degradation of organic pollutants and the corresponding countermeasures. *Water Res.* **79**, 128–146 (2015).
7. Rivera, A. P., Tanaka, K. & Hisanaga, T. Photocatalytic degradation of pollutant over TiO_2 in different crystal structures. *Appl. Catal. B, Environ.* **3**, 37–44 (1993).
8. Turchi, C. S. & Ollis, D. F. Photocatalytic degradation of organic water contaminants: Mechanisms involving hydroxyl radical attack. *J. Catal.* **122**, 178–192 (1990).
9. Kumar, A. A Review on the Factors Affecting the Photocatalytic Degradation of Hazardous Materials. *Mater. Sci. Eng. Int. J.* **1**, 1–10 (2017).
10. Rauf, M. A. & Ashraf, S. S. Fundamental principles and application of heterogeneous photocatalytic degradation of dyes in solution. *Chem. Eng. J.* **151**, 10–18 (2009).

11. Gaya, U. I. & Abdullah, A. H. Heterogeneous photocatalytic degradation of organic contaminants over titanium dioxide: A review of fundamentals, progress and problems. *J. Photochem. Photobiol. C Photochem. Rev.* **9**, 1–12 (2008).
12. Zuo, G. M., Cheng, Z. X., Chen, H., Li, G. W. & Miao, T. Study on photocatalytic degradation of several volatile organic compounds. *J. Hazard. Mater.* **128**, 158–163 (2006).
13. Kudo, A. & Miseki, Y. Heterogeneous photocatalyst materials for water splitting. *Chem. Soc. Rev.* **38**, 253–278 (2009).
14. Maeda, K. Direct splitting of pure water into hydrogen and oxygen using rutile titania powder as a photocatalyst. *Chem. Commun.* **49**, 8404–8406 (2013).
15. Hisatomi, T., Takanabe, K. & Domen, K. Photocatalytic Water-Splitting Reaction from Catalytic and Kinetic Perspectives. *Catal. Letters* **145**, 95–108 (2015).
16. Abe, R., Sayama, K., Domen, K. & Arakawa, H. A new type of water splitting system composed of two different TiO_2 photocatalysts (anatase, rutile) and a IO_3^-/I^- shuttle redox mediator. *Chem. Phys. Lett.* **344**, 339–344 (2001).
17. Takanabe, K. Photocatalytic Water Splitting: Quantitative Approaches toward Photocatalyst by Design. *ACS Catal.* **7**, 8006–8022 (2017).
18. Ni, M., Leung, M. K. H., Leung, D. Y. C. & Sumathy, K. A review and recent developments in photocatalytic water-splitting using TiO_2 for hydrogen production. *Renew. Sustain. Energy Rev.* **11**, 401–425 (2007).
19. Takata, T. *et al.* Photocatalytic water splitting with a quantum efficiency of almost unity. *Nature* **581**, 411–414 (2020).
20. Kočí, K. *et al.* Effect of silver doping on the TiO_2 for photocatalytic reduction of CO_2. *Appl. Catal. B Environ.* **96**, 239–244 (2010).
21. Nakanishi, H., Iizuka, K., Takayama, T., Iwase, A. & Kudo, A. Highly Active $NaTaO_3$-Based Photocatalysts for CO_2 Reduction to Form CO Using Water as the Electron Donor. *ChemSusChem* **10**, 112–118 (2017).
22. Pang, R., Teramura, K., Asakura, H., Hosokawa, S. & Tanaka, T. Highly selective photocatalytic conversion of CO_2 by water over Ag-loaded $SrNb_2O_6$ nanorods. *Appl. Catal. B Environ.* **218**, 770–778 (2017).
23. Habisreutinger, S. N., Schmidt-Mende, L. & Stolarczyk, J. K. Photocatalytic reduction of CO_2 on TiO_2 and other semiconductors. *Angew. Chemie - Int. Ed.* **52**, 7372–7408 (2013).
24. Zhao, H., Pan, F. & Li, Y. A review on the effects of TiO_2 surface point defects on CO_2 photoreduction with H_2O. *J. Mater.* **3**, 17–32 (2017).
25. Palmisano, G., Augugliaro, V., Pagliaro, M. & Palmisano, L. Photocatalysis: a promising route for 21st century organic chemistry. *Chem. Commun.* **0**, 3425–3437 (2007).

26. Palmisano, G. *et al.* Advances in selective conversions by heterogeneous photocatalysis. *Chem. Commun.* **46**, 7074–7089 (2010).
27. Friedmann, D., Hakki, A., Kim, H., Choi, W. & Bahnemann, D. Heterogeneous photocatalytic organic synthesis: state-of-the-art and future perspectives. *Green Chem.* **18**, 5391–5411 (2016).
28. Chen, J., Cen, J., Xu, X. & Li, X. The application of heterogeneous visible light photocatalysts in organic synthesis. *Catal. Sci. Technol.* **6**, 349–362 (2016).
29. Kisch, H. Semiconductor Photocatalysis for Chemoselective Radical Coupling Reactions. *Acc. Chem. Res.* **50**, 1002–1010 (2017).
30. Wu, X., Jaatinen, E., Sarina, S. & Zhu, H. Y. Direct photocatalysis of supported metal nanostructures for organic synthesis. *J. Phys. D. Appl. Phys.* **50**, (2017).
31. Riente, P. & Noël, T. Application of metal oxide semiconductors in light-driven organic transformations. *Catal. Sci. Technol.* **9**, 5186–5232 (2019).
32. Sun, Q. & Xu, Y. Evaluating intrinsic photocatalytic activities of anatase and rutile TiO2 for organic degradation in water. *J. Phys. Chem. C* **114**, 18911–18918 (2010).
33. Augugliaro, V. *et al.* TiO_2-Based Photocatalysis for Organic Synthesis. in *Environmentally Benign Photocatalysts: Applications of Titanium Oxide-based Materials* 623–645 (2010). doi:10.1007/978-0-387-48444-0.
34. Hoffmann, N. Photocatalysis with TiO_2 Applied to Organic Synthesis. *Aust. J. Chem* **68**, 1621–1639 (2015).
35. Oi, L. E. *et al.* Recent advances of titanium dioxide (TiO_2) for green organic synthesis. *RSC Adv.* **6**, 108741–108754 (2016).
36. Fagnoni, M., Dondi, D., Ravelli, D. & Albini, A. Photocatalysis for the formation of the C-C bond. *Chem. Rev.* **107**, 2725–2756 (2007).
37. Wang, Y. *et al.* TiO_2 Photocatalyzed C–H Bond Transformation for C–C Coupling Reactions. *Catalysts* **8**, 355 (2018).
38. Liu, A., Lu, C., Chen, C., Li, S. & Ma, D. TiO_2 photocatalysis for C–C bond formation. *Catal. Sci. Technol.* **8**, 2030–2045 (2018).

Part I

Selective C-C Bond Formation through Ligand-to-Metal Charge Transfer on Titanium Dioxide

Introduction of Part I

Organic Transformation and Heterogeneous Photocatalysis

Organic compounds are essential in the chemical industry; they are used in various chemical products such as pharmaceuticals, agrochemicals, plastics, and other functional materials such as liquid crystals. Consequently, the synthesis of organic compounds has been one of the main topics in the field of chemistry. In modern organic synthesis, a green chemical approach, that aims to reduce the impacts of chemical processes on the environment, seems a prerequisite due to increasing awareness of environmental issues. Especially, how to reduce toxic additives and energy costs has been studied extensively in recent years. In this regard, heterogeneous photocatalysis has gained importance in the field of organic synthesis.[1–5] Mechanism of photocatalysis is as follows. Upon irradiation of light whose photon energy exceeds the bandgap of the photocatalyst, which is mostly semiconductor materials such as metal oxides and sulfides, electrons in the valence band are excited to the conduction band to leave holes. These photogenerated carriers reduce or oxidize molecules adsorbed on the surface of the photocatalyst to promote photocatalytic reactions. The use of photon energy allows the transformation to proceed under mild conditions without using highly reactive additives and sometimes to be endergonic, which is difficult by conventional transition metal catalysis. The use of materials with sufficiently smaller band gap or suitable band engineering enables visible light absorption to use sunlight as a driving force of the reaction. All these advantages make photocatalysis promising in the synthesis of organic molecules.

Organic synthesis by photocatalysis covers a broad range of reactions including oxidative and reductive transformations as well as coupling reactions. The most studied reaction is oxidation. This includes hydroxylation of aromatics,[6–9] oxygenation of olefines,[10–12] and oxidation of alcohols.[13–20] These reactions are carried out mostly under aerobic conditions which often causes overoxidation of the reactant. If the reaction is carried out under anaerobic conditions, the product yield is drastically decreased but the overoxidation can be avoided. In such conditions, direct introduction of a hydroxyl group to a benzene ring is possible using water as an oxidant.[21] Reductive transformation is less studied than oxidation. The reaction often requires a sacrificial reagent such as alcohols to suppress back reactions. Reductions of some compounds such as aldehydes,[22] nitro-aromatic compounds,[23,24] and CO_2[25] are reported. Coupling reactions are a good example that shows the potential of

photocatalysis.[26] Photocatalysis allows direct activation of chemical bonds under mild conditions to promote several coupling reactions. Especially, titanium oxide (TiO_2), which has a strong oxidation power, can break extremely inert bonds such as C–H bond to promote direct or dehydrogenative coupling of various molecules.[27,28] Dehydrogenative coupling by heterogeneous catalysis proceeds in an actual dehydrogenative manner, in which the byproduct is hydrogen gas which is a promising energy carrier.[29] This is different from that in transition metal or photoredox catalysis, where the reaction often proceeds in an oxidative manner by using external oxidants such as molecular oxygen to give water as the byproduct.[30]

Problems of Photocatalytic Organic Transformation and Their Solutions

Although several papers successfully demonstrated the potential use of photocatalysis in organic synthesis and transformation, photocatalysis still has several obstacles to expanding its application.

One of the problems is low selectivity. In photocatalysis, photogenerated electrons and holes, which are produced by photoexcitation of the photocatalyst, activate reactants. If the reactivity of these carriers is too high, the reactants undergo undesired transformations such as overoxidation. This is often the case if the reaction is carried out under aerobic conditions, where reactive oxygen species (ROS) are generated. Especially in TiO_2, one of the most studied and practical photocatalysts, photogenerated holes have strong oxidation power due to the deep position of the valence band edge. These strong oxidative holes often cause unselective oxidation, leading to a loss of reactants and products. Thus, how to improve selectivity is one of the big issues in the synthetic use of heterogeneous photocatalysis. Several strategies have been proposed to achieve selective organic transformation by photocatalysis. Briefly, they can be divided into two: modification of photocatalyst and change of reaction conditions.[31] Modification of photocatalysts includes cocatalyst loading such as Pd[32] and Au,[33] syntheses of photocatalysts with a well-defined structure such as mesoporous and exposed crystal facets, and surface modification such as acid/base modification. Reaction conditions are also important such as temperature, pH, solvent, and atmosphere. In either case, the strategies mainly control the adsorption of the reactant on the photocatalysts.

Another problem is the use of visible light. Commonly used photocatalysts such as TiO_2 are not available under visible light because of their wide band gap energy. This is problematic to achieve solar-light-driven organic transformation. Visible light sensitization of photocatalysis has been studied for a long time and several approaches are reported. One of

them is doping.[34,35] Doping of other elements such as N and S into a photocatalyst generates a new energy state from which electrons are excited to the conduction band, allowing visible light excitation of the photocatalyst. Although many researchers reported successful examples of this approach, the doping sometimes changes the morphology of the photocatalyst such as specific surface area and crystallinity, which decreases photocatalytic activity. Dye sensitization is another approach to utilize visible light.[36,37] However, this approach suffers from the decomposition of dye during the reaction.

Organic Transformation through Photoexcitation of Surface Complex

Recently, some researchers reported a new type of photocatalysis that can achieve both high selectivity and visible light responsibility at the same time: Surface complex system. The system utilizes a photoexcitation of the surface complex to initiate the reaction. Surface complex forms when a molecule has a strong interaction with a surface metal atom of the photocatalyst. The interaction generates a new electronic orbital that originates from unoccupied orbitals of the surface metal atoms on the photocatalyst and the highest occupied molecular orbitals (HOMO) of the adsorbate, which allows visible light excitation of the complex through ligand-to-metal charge transfer (LMCT) mechanism. Unlike in dye sensitization, not the adsorbate itself but the surface complex absorbs visible light in this system. Therefore, relatively simple molecules are available as a reactant in this system such as alcohols,[38,39] amines,[40,41] sulfides,[42] and simple aromatics.[43–46] Another important aspect of the system is high selectivity of the reaction. In semiconductor photocatalysis, electrons in the valence band are excited to the conduction band (CB) to leave photogenerated holes in the valence band (VB) (Fig. 1A). On the other hand, in the surface complex system, electrons are injected from a surface complex to the conduction band of the photocatalyst to leave a hole on the adsorbate (Fig. 1B). This charge transfer process allows milder oxidation of the adsorbate than that in the photocatalysis, leading to selective transformation. For example, selective oxidation of primary alcohols into aldehydes has been reported.[38,47,48]

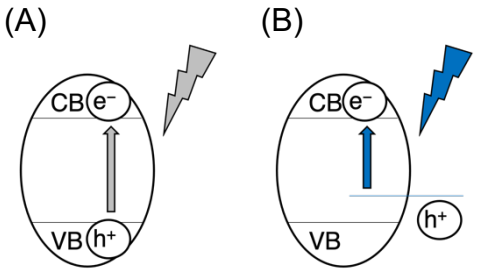

Fig. 1 Schematic illustration of photocatalysis (A) and surface complex system (B).

Outlines of Part I

Although the surface complex system is appealing to achieve selective transformation of organic molecules, its application was limited to oxidative or reductive transformation. In this regard, we recently reported the first example of the surface complex system for C–C bond formation: a selective dehydrogenative cross-coupling between benzene and cyclohexane utilizing a ligand-to-metal charge transfer benzene complex on TiO_2.[45] The system utilizes photoexcitation of a surface complex consists of an adsorbed benzene molecule and the surface of TiO_2 to promote selective cross-coupling with cyclohexane. However, the system suffers from low efficiency due to a weak interaction between benzene and TiO_2 as well as deactivation of the photocatalyst due to the polymerization of benzene. These problems are difficult to be solved merely by modification of the TiO_2 or the reaction condition since they are originated from the property of the adsorbate (benzene) itself. Therefore, other adsorbates are preferred to achieve selective C–C bond formation through photoexcitation of surface complex with high efficiency.

Investigating the substrate scope is also important in organic synthesis. Especially in the surface complex system, the effect of multiple adsorbates should be investigated. As mentioned above, the formation of surface complexes has been reported with various molecules. Therefore, how the system performs and whether the selectivity can be improved even in the presence of multiple adsorbates should be investigated to extend the application of the surface complex system for C–C bond formation. In Part I, we studied three types of surface complex systems to address these issues.

In Chapter 1, we used pyridine as an adsorbate, which adsorbs on TiO_2 through an acid-base interaction. We found that the dehydrogenative coupling between pyridine and cyclohexane proceeds selectively through a visible-light excitation of the pyridine-TiO_2 surface complex. Pyridine radical cation formed by the excitation of the surface complex selectively oxidizes cyclohexane to a cyclohexyl radical to promote the cross-coupling with higher selectivity compared with that in photocatalysis by TiO_2 under UV irradiation.

In Chapter 2, we studied Minisci-type functionalization[49] of pyridine with tetrahydrofuran through a photoexcitation of surface Ti-peroxo species. In this study, H_2O_2 is used as both an additive to improve efficiency and an adsorbate to form a surface complex. We found that the addition of H_2O_2 under acidic conditions can improve the yield of the reaction by 21 times. We also found that visible-light excitation of surface Ti-peroxo complex, formed upon contact of H_2O_2 with the surface of TiO_2, doubled the selectivity than that with UV-light

excitation of TiO_2. Scavenging tests suggests that the active species is reactive oxygen species (ROS) produced by reduction of H_2O_2 by electrons excited from the peroxo species. The higher selectivity under visible light is due to suppression of the hole oxidation of H_2O_2, which causes undesired oxidation of THF.

In Chapter 3, dehydrogenative coupling using TiO_2 photocatalyst was carried out between pyridine and benzene,[45] both of which are reported as adsorbates for surface complexation. We found that the dehydrogenative coupling can proceed selectively in the presence of an excess amount of benzene. Pyridine strongly adsorbs on the TiO_2 to form the surface complex, which favors homo-coupling of pyridine even under visible light irradiation. The use of an excess amount of benzene is necessary to suppress the homo-coupling and thus to promote the cross-coupling selectively.

References

1. Palmisano, G., Augugliaro, V., Pagliaro, M. & Palmisano, L. Photocatalysis: a promising route for 21st century organic chemistry. *Chem. Commun.* 3425–3437 (2007).
2. Hoffmann, N. Photocatalysis with TiO_2 Applied to Organic Synthesis. *Aust. J. Chem* **68**, 1621–1639 (2015).
3. Oi, L. E. *et al.* Recent advances of titanium dioxide (TiO_2) for green organic synthesis. *RSC Adv.* **6**, 108741–108754 (2016).
4. Friedmann, D., Hakki, A., Kim, H., Choi, W. & Bahnemann, D. Heterogeneous photocatalytic organic synthesis: state-of-the-art and future perspectives. *Green Chem.* **18**, 5391–5411 (2016).
5. Riente, P. & Noël, T. Application of metal oxide semiconductors in light-driven organic transformations. *Catal. Sci. Technol.* **9**, 5186–5232 (2019).
6. Mossanega, M.-N. & Pichat, J. M. H. et P. OXYDATION D'ALKYLTOLUENES EN ALKYLBENZALDEHYDES AU CONTACT DE TiO_2 IRRADIE SOUS UV. *Tetrahedron Lett.* **18**, 2965–2966 (1977).
7. Fujihira, M., Satoh, Y. & Osa, T. Heterogeneous photocatalytic oxidation of aromatic compounds on TiO_2. *Nature* **293**, 206–208 (1981).
8. Gonzalez, M. A., Howell, S. G. & Sikdar, S. K. Photocatalytic selective oxidation of hydrocarbons in the aqueous phase. *J. Catal.* **183**, 159–162 (1999).
9. Augugliaro, V. *et al.* TiO_2-Based Photocatalysis for Organic Synthesis. in *Environmentally Benign Photocatalysts: Applications of Titanium Oxide-based Materials* 623–645 (2010).
10. Yoshida, H., Murata, C. & Hattori, T. Photocatalytic epoxidation of propene by molecular oxygen over monoatomic metal oxide species dispersed in silica. *Chem.*

Commun. 1551–1552 (1999).

11. Li, X. & Kutal, C. Photocatalytic selective epoxidation of styrene by molecular oxygen over highly dispersed titanium dioxide species on silica. *J. Mater. Sci. Lett.* **21**, 1525–1527 (2002).
12. Shiraishi, Y., Morishita, M. & Hirai, T. Acetonitrile-assisted highly selective photocatalytic epoxidation of olefins on Ti-containing silica with molecular oxygen. *Chem. Commun.* 5977–5979 (2005).
13. Pillai, U. R. & Sahle-Demessie, E. Selective oxidation of alcohols in gas phase using light-activated titanium dioxide. *J. Catal.* **211**, 434–444 (2002).
14. Palmisano, G., Yurdakal, S., Augugliaro, V., Loddo, V. & Palmisano, L. Photocatalytic selective oxidation of 4-methoxybenzyl alcohol to aldehyde in aqueous suspension of home-prepared titanium dioxide catalyst. *Adv. Synth. Catal.* **349**, 964–970 (2007).
15. Augugliaro, V. *et al.* Photocatalytic oxidation of aromatic alcohols to aldehydes in aqueous suspension of home prepared titanium dioxide 2. Intrinsic and surface features of catalysts. *Appl. Catal. A Gen.* **349**, 189–197 (2008).
16. Zhang, M. *et al.* Oxygen atom transfer in the photocatalytic oxidation of alcohols by tio2: Oxygen isotope studies. *Angew. Chemie - Int. Ed.* **48**, 6081–6084 (2009).
17. Yurdakal, S., Palmisano, G., Loddo, V., Augugliaro, V. & Palmisano, L. Nanostructured rutile TiO_2 for selective photocatalytic oxidation of aromatic alcohols to aldehydes in water. *J. Am. Chem. Soc.* **130**, 1568–1569 (2008).
18. Furukawa, S., Shishido, T., Teramura, K. & Tanaka, T. Photocatalytic Oxidation of Alcohols over TiO_2 Covered with Nb_2O_5. *ACS Catal.* **2**, 175–179 (2012).
19. Imamura, K. *et al.* Simultaneous production of aromatic aldehydes and dihydrogen by photocatalytic dehydrogenation of liquid alcohols over metal-loaded titanium(IV) oxide under oxidant- and solvent-free conditions. *Appl. Catal. A Gen.* **450**, 28–33 (2013).
20. Tsukamoto, D. *et al.* Selective photocatalytic oxidation of alcohols to aldehydes in water by TiO_2 partially coated with WO_3. *Chem. - A Eur. J.* **17**, 9816–9824 (2011).
21. Yoshida, H. *et al.* Photocatalytic hydroxylation of aromatic ring by using water as an oxidant. *Chem. Commun.* 4634–4636 (2008) doi:10.1039/b811555a.
22. Joyce-pruden, C., Pross, J. K. & Li, Y. Photoinduced Reduction of Aldehydes on Titanium Dioxide. *J. Org. Chem.* **57**, 5087–5091 (1992).
23. Mahdavi, F., Bruton, T. C. & Li, Y. Photoinduced Reduction of Nitro Compounds on Semiconductor Particles. *J. Org. Chem.* **58**, 744–746 (1993).
24. Wang, H., Yan, J., Chang, W. & Zhang, Z. Practical synthesis of aromatic amines by photocatalytic reduction of aromatic nitro compounds on nanoparticles N-doped TiO2. *Catal. Commun.* **10**, 989–994 (2009).
25. Habisreutinger, S. N., Schmidt-Mende, L. & Stolarczyk, J. K. Photocatalytic reduction of CO_2 on TiO_2 and other semiconductors. *Angew. Chemie - Int. Ed.* **52**, 7372–7408

(2013).
26. Fagnoni, M., Dondi, D., Ravelli, D. & Albini, A. Photocatalysis for the formation of the C-C bond. *Chem. Rev.* **107**, 2725–2756 (2007).
27. Wang, Y. *et al.* TiO_2 Photocatalyzed C–H Bond Transformation for C–C Coupling Reactions. *Catalysts* **8**, 355 (2018).
28. Liu, A., Lu, C., Chen, C., Li, S. & Ma, D. TiO_2 photocatalysis for C–C bond formation. *Catal. Sci. Technol.* **8**, 2030–2045 (2018).
29. Mazloomi, K. & Gomes, C. Hydrogen as an energy carrier: Prospects and challenges. *Renew. Sustain. Energy Rev.* **16**, 3024–3033 (2012).
30. Liu, C. *et al.* Oxidative Coupling between Two Hydrocarbons: An Update of Recent C-H Functionalizations. *Chem. Rev.* **115**, 12138–12204 (2015).
31. Kou, J. *et al.* Selectivity Enhancement in Heterogeneous Photocatalytic Transformations. *Chem. Rev.* **117**, 1445–1514 (2017).
32. Tyagi, A., Matsumoto, T., Kato, T. & Yoshida, H. Direct C–H bond activation of ethers and successive C–C bond formation with benzene by a bifunctional palladium-titania photocatalyst. *Catal. Sci. Technol.* **6**, 4577–4583 (2016).
33. Naya, S., Teranishi, M., Isobe, T. & Tada, H. Light wavelength-switchable photocatalytic reaction by gold nanoparticle-loaded titanium(iv) dioxide. *Chem. Commun.* **46**, 815–817 (2010).
34. Asahi, R., Morikawa, T., Ohwaki, T. & Taga, Y. Visible-Light Photocatalysis in Nitrogen-Doped Titanium Oxides. *Science.* **293**, 269–271 (2001).
35. Kumar, S. G. & Devi, L. G. Review on modified TiO_2 photocatalysis under UV/visible light: Selected results and related mechanisms on interfacial charge carrier transfer dynamics. *J. Phys. Chem. A* **115**, 13211–13241 (2011).
36. Zhang, X., Peng, T. & Song, S. Recent advances in dye-sensitized semiconductor systems for photocatalytic hydrogen production. *J. Mater. Chem. A* **4**, 2365–2402 (2016).
37. Etacheri, V., Di Valentin, C., Schneider, J., Bahnemann, D. & Pillai, S. C. Visible-light activation of TiO_2 photocatalysts: Advances in theory and experiments. *J. Photochem. Photobiol. C Photochem. Rev.* **25**, 1–29 (2015).
38. Higashimoto, S. *et al.* Selective photocatalytic oxidation of benzyl alcohol and its derivatives into corresponding aldehydes by molecular oxygen on titanium dioxide under visible light irradiation. *J. Catal.* **266**, 279–285 (2009).
39. Zhu, S. *et al.* Ultrathin nanosheets of molecular sieve SAPO-5: A new photocatalyst for efficient photocatalytic reduction of CO_2 with H_2O to methane. *Appl. Catal. B Environ.* **187**, 11–18 (2016).
40. Higashimoto, S. *et al.* Selective Photocatalytic Oxidation of Benzyl Amine By O_2 Into N-Benzylidenebenzylamine on TiO_2 Using Visible Light. *Curr. Org. Chem.* **17**, 2374–

2381 (2013).

41. Lang, X. *et al.* Visible-light-induced selective photocatalytic aerobic oxidation of amines into imines on TiO_2. *Chem. - A Eur. J.* **18**, 2624–2631 (2012).
42. Lang, X. *et al.* Tertiary amine mediated aerobic oxidation of sulfides into sulfoxides by visible-light photoredox catalysis on TiO_2. *Chem. Sci.* **6**, 5000–5005 (2015).
43. Kamegawa, T., Seto, H., Matsuura, S. & Yamashita, H. Preparation of hydroxynaphthalene-modified TiO_2 via formation of surface complexes and their applications in the photocatalytic reduction of nitrobenzene under visible-light irradiation. *ACS Appl. Mater. Interfaces* **4**, 6635–6639 (2012).
44. Kamegawa, T., Matsuura, S., Seto, H. & Yamashita, H. A visible-light-harvesting assembly with a sulfocalixarene linker between dyes and a Pt-TiO_2 photocatalyst. *Angew. Chemie - Int. Ed.* **52**, 916–919 (2013).
45. Yamamoto, A., Ohara, T. & Yoshida, H. Visible-light-induced photocatalytic benzene/cyclohexane cross-coupling utilizing a ligand-to-metal charge transfer benzene complex adsorbed on titanium oxides. *Catal. Sci. Technol.* **8**, 2046–2050 (2018).
46. Naniwa, S., Tyagi, A., Yamamoto, A. & Yoshida, H. Visible-light photoexcitation of pyridine surface complex, leading to selective dehydrogenative cross-coupling with cyclohexane. *Phys. Chem. Chem. Phys.* **20**, 28375–28381 (2018).
47. Furukawa, S., Shishido, T., Teramura, K. & Tanaka, T. Selective Aerobic Oxidation of Primary Alcohols to Aldehydes over Nb_2O_5 Photocatalyst with Visible Light. *ChemPhysChem* **15**, 2665–2667 (2014).
48. Li, C. J., Xu, G. R., Zhang, B. & Gong, J. R. High selectivity in visible-light-driven partial photocatalytic oxidation of benzyl alcohol into benzaldehyde over single-crystalline rutile TiO_2 nanorods. *Appl. Catal. B Environ.* **115**–**116**, 201–208 (2012).
49. Minisci, F., Bernardi, R., Bertini, F., Galli, R. & Perchinummo, M. Nucleophilic character of alkyl radicals—VI A NEW CONVENIENT SELECTIVE ALKYLATION OF HETEROAROMATIC BASES. *Tetrahedron* **27**, 3575–3579 (1971).

Chapter 1

Visible-light photoexcitation of pyridine surface complex, leading to selective dehydrogenative cross-coupling with cyclohexane

Abstract

Upon photoirradiation with visible light, a pyridine molecule adsorbed on a TiO_2 surface can be photoexcited to give a pyridine radical cation via ligand-to-metal charge transfer (LMCT) between pyridine and titanium. This leads to dehydrogenative cross-coupling (DCC) between pyridine and cyclohexane with concomitant hydrogen evolution. Since the radical cation can selectively oxidize cyclohexane to a cyclohexyl radical, the cross-coupling between pyridine and cyclohexane proceeds with higher selectivity compared with that in photocatalysis by TiO_2 under UV irradiation.

Introduction

Titanium oxide (TiO_2) is one of the most practical photocatalyst because of its abundance, chemical stability and strong oxidation ability, and thus many applications have been studied in both environmental and energy fields.[1] In addition, many studies have been reported about organic synthesis by TiO_2 photocatalyst.[2–6] One of the problems of TiO_2 photocatalyst is, however, difficulty in selective oxidation because of its strong oxidation ability that arises from the highly positive potential of its valence band. In this regard, several recent studies have developed photoexcitation of surface complex consisting of adsorbed molecules and the surface of TiO_2, since they can be excited by visible light to promote various selective photooxidation reactions of various compounds such as alcohol,[7,8] amine,[9,10] and sulfides.[11] The key feature of these systems is the use of a localized photoformed positive hole on the molecule to prevent undesired oxidation.

Although cross-coupling reactions have been studied well both in homogeneous and heterogeneous catalysis,[12–14] no one had applied the surface complex systems to cross-coupling reactions. We recently discovered that when benzene adsorbed *via* π-interaction with the TiO_2 surface is excited under visible light, a positive hole is generated in the benzene (a benzene radical cation) to promote direct photocatalytic dehydrogenative cross-coupling (DCC) reaction between benzene and cyclohexane to yield phenylcyclohexane and hydrogen.[15]

In the present study, we propose a new type of photoactive surface complex, which is an acid-base interacted heteroaromatic surface complex. As a simple example, we employed pyridine as an adsorbate and found for the first time that a DCC between pyridine and cyclohexane can take place with high selectivity (>99% at 3.0 % yield) through a novel and unique reaction mechanism, which starts from a visible light excitation of the surface complex consisting of pyridine and TiO_2 surface.

Experimental

Catalyst preparation

Various TiO_2 powder samples employed were donated by the Catalysis Society of Japan as JRC-TIO-8, JRC-TIO-14 (these are equivalent, anatase phase, 338 $m^2 g^{-1}$), JRC-TIO-6 (rutile phase, 100 $m^2 g^{-1}$), JRC-TIO-4 (a mixture of rutile and anatase phases, 50 $m^2 g^{-1}$) and JRC-TIO-2 (anatase phase, 18 $m^2 g^{-1}$). All metal-loaded TiO_2 catalysts were prepared by a photodeposition method using the TiO_2 powder and an aqueous methanol solution of an appropriate metal precursor such as $PdCl_2$ (Kishida, 99%), $H_2PtCl_6 \cdot 6H_2O$ (Wako, 99.9%), and

$RhCl_3 \cdot 3H_2O$ (Kishida, 99%), as follows. The TiO_2 powder (4.0 g) was dispersed in ion-exchanged water (300 ml) and was irradiated with a ceramic xenon lamp (PE300BUV) for 30 min. Then, methanol (100 ml) and the desired amount of the metal precursor solution were added to the suspension and the contents were magnetically stirred for 15 min without irradiation, followed by stirring in the light for 1 h. It was then filtered off with suction, washed with ion-exchanged water, and dried at 323 K for 12 h so as to obtain the metal-loaded TiO_2 photocatalysts. The catalysts were referred to as M(x)/TiO_2, where M indicates Pt, Pd, or Rh, and x indicates the loading amount in weight %.

Reaction tests

Materials. All of the chemicals employed for the photocatalytic reaction tests were of analytical grade and were used without further purification; pyridine (Nacalai Tesque, 99.7 %), cyclohexane (Nacalai Tesque, 99.5 %), 4-cyclohexylpyridine (Santa Cruz Biotechnology), 2,2'-bipyridyl (Wako Pure Chemicals, 99.5 %), 2,3'-bipyridine (Sankyo Chemical Industry), 2,4'-bipyridyl (Wako Pure Chemicals, 97 %), bicyclohexyl (Tokyo Kasei Kogyo, >99 %), cyclohexanone (Nacalai Tesque, 97 %), cyclohexanol (Kishida Chemical, >99 %), pyridine-d_5 (Euriso-Top, 99.5 %) and cyclohexane-d_{12} (Sigma-Aldrich, 99.6 %).

Most of the authentic samples were purchased to make the GC-MS calibration curve for the quantitative analysis of the products in the reaction experiments, while an authentic sample of the main cross-coupling product from pyridine and cyclohexane, 2-cyclohexylpyridine (2-CHP), was synthesized in the manner reported in the literature.[16] For quantification of 3-cyclohexylpyridine (3-CHP) and tri-coupled products, the calibration curve of 2-CHP was tentatively used.

Procedure for the reaction tests. Before a photocatalytic reaction test, the M(x)/TiO_2 sample (0.1 g) in a Pyrex glass tube (20 mL) was subjected to pre-treatment for 30 min under the light from the xenon lamp to clean its surface. Then, the reactants were added into the test tube, followed by sealing of the reactor with a rubber septum and bubbling argon for 10 min. The reaction mixture was irradiated by using the 300 W xenon lamp with stirring for the desired reaction time at room temperature. The irradiation wavelength was limited by a cut-off filter. After the irradiation, 0.5 mL of the gaseous phase was collected by an air-tight syringe and analyzed by a GC-TCD (Shimadzu, GC-8A). The reaction mixture in the liquid phase was sampled by a syringe with a PTFE filter to remove the M(x)/TiO_2 sample, and then analyzed by a GC-MS (Shimadzu, GCMS-QP2020).

Mechanistic studies. To get an insight into the reaction mechanism, some photocatalytic reaction tests for reaction kinetic study were performed with isotopically labelled compounds such as deuterated pyridine and deuterated cyclohexane.

Temperature controlled photocatalytic reactions were also carried out, where a beaker was used as a water bath to keep the desired reaction temperature in the range of 310–328 K. A mixture of pyridine (0.61 mmol) and cyclohexane (9.0 mmol) was used as the substrates.

Diffuse reflectance UV-vis spectroscopy

UV-vis spectra of the powder samples were recorded in a diffuse reflectance (DR) mode. For the measurements the samples were prepared as follows. A mixture of TiO_2 (JRC-TIO-14, 0.3 g) and $BaSO_4$ (2.97 g) was well mixed in a mortar for 15 min so as to give a 100 times diluted TiO_2 sample. For the samples with an adsorbate, 50 μL of pyridine or cyclohexane was added to 0.15 g of the diluted samples or $BaSO_4$, followed by 30 min of stirring. Then, desired amount of the sample (typically 0.13 g) was taken into the cell so as to fix the amount of TiO_2 in the samples and the spectrum was measured using a UV-vis spectrophotometer (JASCO V-570) equipped with an integrating sphere, where $BaSO_4$ was used as a reference.

Results and discussion

The reaction took place to give 2-cyclohexylpyridine (2-CHP), 3-cyclohexylpyridine (3-CHP), and 4-cyclohexylpyridine (4-CHP) as the DCC products (CHPs), as well as the homo-coupling products from pyridine (bipyridyls (BPs): 2-BP, 3-BP, and 4-BP) and cyclohexane (bicyclohexyl: BCH), and very small amount of tri-coupled products whose mass numbers were 238 and 243, *i.e.*, possibly formed from two pyridine and one cyclohexane and from one pyridine and two cyclohexane. Tiny amounts of cyclohexanone and cyclohexanol were also formed, which would be produced in the photocatalytic oxidation by the surface hydroxyl group or adsorbed water as reported.[17] The reaction did not proceed in the dark or in the absence of the photocatalyst.

Optimization of photocatalyst

We first optimized the photocatalyst. The reaction tests were carried out with various Pt(0.1)/TiO_2 samples for the dehydrogenative cross-coupling (DCC) reaction under visible light irradiation ($\lambda > 422$ nm). The results are shown in Table 1. Among these catalysts, the Pt(0.1)/JRC-TIO-8 sample (Table 1, entry 1, ST-01, anatase, 338 $m^2\ g^{-1}$) and the Pt(0.1)/JRC-TIO-6 sample (Table 1, entry 2, rutile, 100

m^2 g^{-1}) showed high activity and selectivity. Among the two, the former gave a less amount of cyclohexanone and cyclohexanol than the latter, leading to the higher selectivity to CHPs based on cyclohexane (S_{Cy}= 91%). JRC-TIO-4 and JRC-TIO-2 (Table 1, entries 3 and 4), which have lower specific surface area, provided less active photocatalysts than JRC-TIO-8 and JRC-TIO-6. Therefore, we employed JRC-TIO-8 as the TiO_2 photocatalyst in the following experiments.

Table 1 Results of the reaction tests under photoirradiation with various Pt(0.1)/TiO_2 photocatalysts[a]

Entry	TiO_2	Crystal phase	Specific surface area / m^2 g^{-1}	Products / μmol [b]				Selectivity (%) [c]	
				CHPs	BPs	BCH	CHOs	S_{Py}	S_{Cy}
1	JRC-TIO-8	Anatase	338	1.2	0.11	0.011	0.098	83	91
2	JRC-TIO-6	Rutile	100	1.2	0.058	0.038	0.27	91	78
3	JRC-TIO-4	Anatase, rutile	50	0.46	0.042	0.015	0.24	85	63
4	JRC-TIO-2	Anatase	8	0	0	0	0.25	-	-

[a] Reaction conditions: pyridine (0.10 mL, 1.2 mmol) and cyclohexane (1.9 mL, 18 mmol) with the Pt(0.1)/TiO_2 photocatalyst (0.1 g) were used, the reaction time was 2 h, the light intensity was 130 mW cm^{-2} measured at 395 ± 35 nm in wavelength, and the irradiation wavelength was $\lambda > 422$ nm. [b] CHPs: total amount of 2-CHP, 3-CHP, and 4-CHP. BPs: total amount of 2,2'-BP, 2,3'-BP, and 2,4'-BP. CHOs: total amount of cyclohexanone and cyclohexenol. [c] DCC selectivity based on pyridine was calculated as: S_{py} = [100 × CHPs (μmol)]/[(CHPs + 2 × BPs) (μmol)]; DCC selectivity based on cyclohexane as: S_{cy} = [100 × CHPs (μmol)]/[(CHPs + 2 × BHC + CHOs) (μmol)].

Next, we examined some kinds of metal co-catalyst on the TiO_2 (JRC-TIO-8) photocatalyst for the DCC reaction under visible light irradiation ($\lambda > 400$ nm, Table 2). Generally, it is considered that metal co-catalyst on photocatalysts can suppress the recombination of the photogenerated electrons and holes.[18–20] The Pt loaded photocatalyst (Table 2, entry 2) showed higher activity than the non-metal loaded photocatalyst (Table 2, entry 1). This suggests that the loaded Pt species actually worked as a charge separator to enhance the photocatalytic activity. Among various metal loaded catalysts (Table 2, entries 3–5), the Pt loaded catalyst showed the best activity and selectivity (Table 2, entry 3). Interestingly, a Pd loaded sample promoted the homo-coupling of pyridine rather than the cross-coupling while Pt and Rh loaded samples showed similarly good activities toward the cross-coupling. Since we previously reported that Pd co-catalyst on TiO_2 can activate benzene ring for the addition of photogenerated radicals in several photocatalytic reactions,[15,21–23] it can be assumed that pyridine, one of heteroaromatics, is also activated by Pd co-catalyst to promote its homo-coupling through the radical addition-elimination mechanism.

Also, we optimized the loading amount of Pt on the photocatalyst (Table 3). Decreasing the loading amount from 0.1 wt% did not affect so much the amount of the cross-coupling products but it increased the amount of by-products such as cyclohexanone and cyclohexanol (Table 3, entries 1–3). This indicates that more surface hydroxyl groups were exposed with decreasing the loading amount of Pt and this could enhance the photocatalytic oxidation of cyclohexane.[2] On the other hand, the cross-

coupling yield was decreased with increasing the loading amount from 0.1 wt% (Table 3, entries 5 and 6). This might be due to a variation of the particle size or the number of Pt nanoparticles deposited on the TiO_2 surface.

Table 2 Results of the reaction tests under photoirradiation with various M(0.1)/TiO_2 photocatalysts[a]

Entry	Metal	Products / μmol [b]				Selectivity (%) [c]	
		CHPs	BPs	BCH	CHOs	S_{Py}	S_{Cy}
1	-	1.3	0.080	0.12	0.31	89	70
2	Pt	3.5	0.27	0.47	0.18	87	76
3	Pt	4.4	6.2	0.029	0.084	26	97
4	Rh	4.0	6.8	0.029	0.15	23	95
5	Pd	1.7	9.3	0	0.22	8.0	88

[a] Reaction conditions: pyridine (1.2 mmol) and cyclohexane (18 mmol) with the M(0.1)/TIO-8 photocatalyst (0.1 g) were used, the reaction time was 2 h, the light intensity was 130 mW cm^{-2} measured at 395 ± 35 nm in wavelength, and the irradiation wavelength was $\lambda > 400$ nm. [b] See the caption of Table 1. [c] Pyridine (12 mmol) and cyclohexane (9.3 mmol) were used.

Table 3 Results of the reaction tests under photoirradiation with various Pt(x)/TiO_2 photocatalysts [a]

Entry	x (wt%)	Products / μmol [b]				Selectivity (%) [c]	
		CHPs	BPs	BCH	CHOs	S_{Py}	S_{Cy}
1	0.001	1.4	0.0048	0.061	0.36	99	74
2	0.01	1.4	0.0092	0.058	0.35	99	75
3	0.025	1.7	0.0059	0.053	0.15	99	87
4	0.1	1.5	trace	0.041	0.020	>99	94
5	0.2	1.0	0	0.019	0.0067	>99	96
6	0.5	0.68	trace	0.013	0.087	>99	86

[a] Reaction conditions: pyridine (0.31 mmol) and cyclohexane (18 mmol) with the Pt(x)/TIO-8 photocatalyst (0.1 g) were used, the reaction time was 2 h, the light intensity was 160 mW cm^{-2} measured at 395 ± 35 nm in wavelength, and the irradiation wavelength was $\lambda > 422$ nm. [b] See the caption of Table 1.

Finally, according to these results, the Pt(0.1)/TIO-8 was employed as the best catalyst.

Effect of irradiation wavelength

Under the light including both UV and visible light ($\lambda > 350$ nm, Table 4, entry 1), the selectivity to the DCC products was low such as 37% and 33% based on the products from pyridine (S_{py}) and cyclohexane (S_{cy}), respectively, in this irradiation condition, which originated from the formation of undesired products such as BPs, BCH and so on. The unselective formation of them suggests that both pyridyl ($^{\cdot}C_5H_4N$) and cyclohexyl ($^{\cdot}C_6H_{11}$) radicals were formed by the photocatalytic hole oxidation of these reactants on the UV-light-activated TiO_2 photocatalyst, followed by their successive radical coupling.

In contrast, under visible light irradiation ($\lambda > 400$ and 422 nm), the selectivity to the DCC products was higher (Table 4, entries 2 and 3), especially under the further limited light irradiation ($\lambda > 422$ nm)

S_{py} and S_{cy} were 83% and 91%, respectively (Table 4, entry 3), although the production rates were lower due to the limited photon numbers compared with the case including UV light. Lower concentration of pyridine provided higher selectivity (S_{py}>99%) due to a suppression of homo-coupling of pyridine (Table 4, entry 4) and the selectivity maintained for a long time even after the yield reached to 3.0 % (Table 4, entry 5 and Figure 1). This indicates the presence of different reaction mechanism from that under the irradiation including UV light. A decrease in the slope of the product yield curve with time might be due to successive reactions of the products or adsorption of the products disturbing the surface active sites. Additionally, it was found that the regioselectivity of CHPs was almost the same in most cases regardless of the irradiation wavelength, *i.e.*, about 65 % of 2-CHP, 10 % of 3-CHP, and 25 % of 4- CHP, which is almost consistent with the C–H bond dissociation energy (BDE) of pyridine (439.3 kJ mol^{-1} for the site 2 and 468.6 kJ mol^{-1} for the sites 3 and 4).[24] We also observed enough amount of hydrogen production, confirming that the reaction underwent dehydrogenatively. Although it was difficult to determine the accurate amount in all the reaction tests, the amount was larger than that expected from those of the detected organic products as is clear in the large value in the H_2 balance. This could be due to the presence of undetected strongly-adsorbed products on the catalyst surface or the progress of side reactions such as dehydrogenation of cyclohexane or successive reactions of the products to larger oligomers.

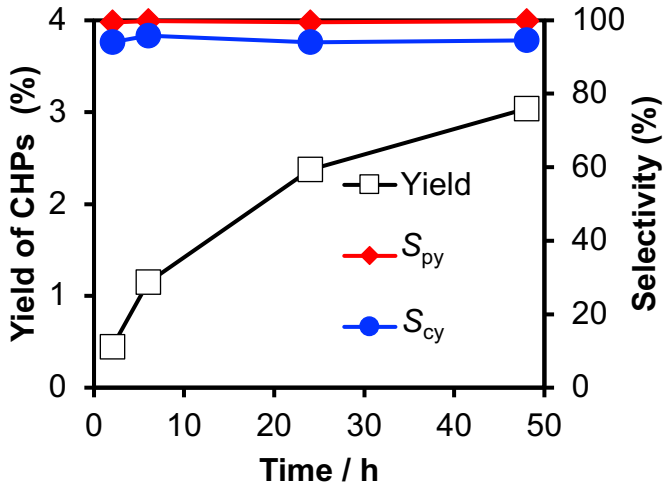

Fig. 1 Time course of the cross-coupling reaction between pyridine and cyclohexane. Pyridine (0.025 mL, 0.31 mmol) and cyclohexane (1.975 mL, 18 mmol) with the Pt(0.1)/TiO_2 photocatalyst (0.1 g) were used. The irradiation wavelength was λ > 422 nm in wavelength. See the caption of Table 4 for the definitions for the DCC selectivities, S_{py} and S_{cy}.

Table 4 Results of reaction tests under photoirradiation in the light of variously limited wavelength [a]

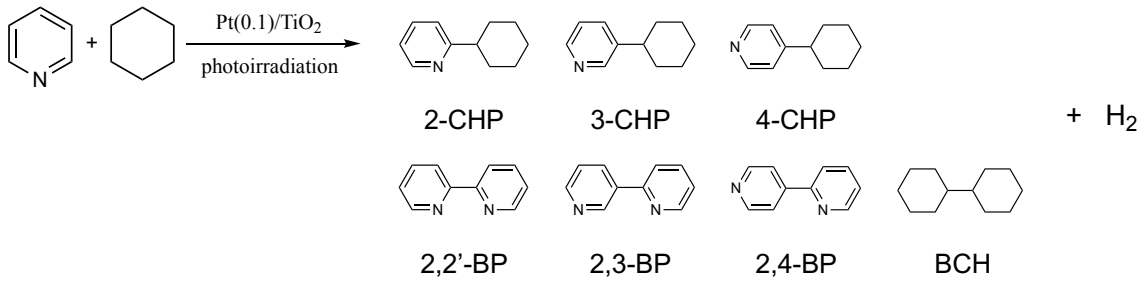

Entry	Substrate / mmol		λ / nm	Time / h	Products / μmol [b]						Conv. (%) [e]	Yield of CHPs (%) [f]	Selectivity (%) [g]	
	C_5H_5N	C_6H_{12}			CHPs	BPs	BCH	CHOs	Tri-coupled [c]	H_2 (balance [d])			S_{py}	S_{cy}
1	1.2	18	>350	2	8.7	7.6	8.8	0.15	0.12	210 (8.3)	2.0	0.73	37	33
2	1.2	18	>400	2	5.5	1.3	0.47	0.17	0.0027	32 (4.4)	0.68	0.46	68	78
3	1.2	18	>422	2	1.2	0.11	0.011	0.065	0.00	14 (11)	0.12	0.10	83	91
4	0.31	18	>422	2	1.4	0.0034	0.033	0.00	0.00	17 (12)	0.45	0.44	>99	94
5	0.31	18	>422	48	9.4	0.013	0.27	0.00	0.00	60 (6.2)	3.0	3.0	>99	94

[a] Reaction conditions: pyridine (0.10 mL, 1.2 mmol) and cyclohexane (1.9 mL, 18 mmol) with the Pt(0.1)/TiO_2 photocatalyst (0.1 g) were used, the light intensity was 130 mW cm^{-2} measured at 395 ± 35 nm in wavelength. [b] CHPs: total amount of 2-CHP, 3-CHP, and 4-CHP. BPs: total amount of 2,2'-BP, 2,3'-BP, and 2,4'-BP. CHOs: total amount of cyclohexanone and cyclohexanol. [c] The mass numbers were 238 and 243. [d] H_2 balance was calculated as: [Actual amount of H_2 (μmol)] / [Expected amount of H_2 (CHPs + BPs + BCH + 2 × Tri-coupled) (μmol)]. [e] Conversion of pyridine was calculated as: [100 × (CHPs+ 2 × BHC) (μmol)]/[C_5H_5N (μmol)]. [f] Yield of CHPs based on the introduced pyridine. [g] DCC selectivity. Selectivity based on the products from pyridine was calculated as: S_{py} = [100 × CHPs (μmol)]/[(CHPs + 2 × BPs) (μmol)]; selectivity based on cyclohexane as: S_{cy} = [100 × CHPs (μmol)]/[(CHPs + 2 × BHC + CHOs) (μmol)].

Diffuse reflectance UV-vis spectroscopy

As well known, the TiO_2 photocatalyst itself cannot work under visible light irradiation. To investigate the origin of the photoexcitation under visible light, we carried out diffuse reflectance UV-vis spectroscopy. The powder TiO_2 samples were diluted by $BaSO_4$ to decrease the absorption for accurate discussion. Fig. 2A shows DR UV-vis spectra of the TiO_2 sample, the pyridine adsorbed TiO_2 sample, the pyridine adsorbed $BaSO_4$, and the difference spectrum of the pyridine adsorbed samples, and Fig. 2B shows their enlarged view and the transmission spectra of various cut-off filters ($\lambda > 350$, 400, and 422 nm) used in the reaction tests.

The spectrum of the pyridine adsorbed $BaSO_4$ (Fig. 2Ac) was almost similar to the absorption spectrum of molecular pyridine in a cyclohexane solution (Fig. 3Aa). Cyclohexane exhibited no absorption in the spectrum (Fig. 3Ab). The spectrum of cyclohexane adsorbed sample was almost same with TiO_2 itself (Fig. 3Bc). Thus, the absorption band at 250–300 nm in wavelength shown in Fig. 2Ac is assignable to pyridine molecule adsorbed physically or that in liquid phase.

It is notable that the pyridine adsorbed TiO_2 sample exhibited a large absorption band (Fig. 2Ab) and the absorption edge was extended to longer than 400 nm (Fig. 2Bb) while TiO_2 itself only absorbed UV light less than 380 nm (Figs. 2Aa and 2Ba). Comparison of the spectra of the pyridine adsorbed samples with and without TiO_2 (Figs. 2Ab and 2Ac) confirmed that the pyridine-adsorbed TiO_2 exhibited a new broad absorption band centered around 300 nm, shown as the difference spectrum (Fig. 2Ad), that should appear as a result of the interaction between pyridine and TiO_2. It can be proposed that this absorption band is attributed to LMCT excitation of the surface complex of the adsorbed pyridine and the TiO_2 surface as with those reported other adsorbates such as catechol, alcohol[8] and amine.[9,10] Pyridine as a base molecule can be adsorbed by an acid-base interaction on the surface Lewis acid sites (Ti^{4+} cation) on TiO_2 surface.[25] The present LMCT would occur in the N–Ti coordination bond in analogy with other amine-TiO_2[9,10] and NH_3-TiO_2[26] surface complex systems.

If the LMCT transition occurs from HOMO of the adsorbed pyridine to the conduction band of TiO_2, which is not a sharp energy distribution but a rather wide band, its spectrum shape should be cliff-shaped as with that of TiO_2 absorption band. However, the shape is bell-shaped. Thus, it is suggested that the LMCT transition occurs not to the conduction band of TiO_2 but to the localized 3d orbital of the surface Ti cation interacted with pyridine. The excited electron finally would be transferred to the conduction band of TiO_2, which is supported by the Pt-promoting hydrogen production as mentioned later. Furthermore, since HOMO of pyridine consists of mainly the lone pair of nitrogen,[27] an electron would be excited from the lone pair of nitrogen to the Ti cation. This means

that the excited state of the surface complex would be a radical cation (Ti–$C_5H_5N^{\cdot+}$) as shown in the scheme in Fig. 2A. The LMCT absorption band was extended to longer than 400 nm in wavelength (Fig. 2Bd). Thus, the first photoactivated species in the reaction system under visible light irradiation is related to not cyclohexane nor TiO_2 itself but the adsorbed pyridine on the TiO_2 surface, in other words, the DCC reaction under visible light starts with the generation of pyridine radical cation through the LMCT excitation of the acid-base interacted surface complex on the TiO_2 surface.

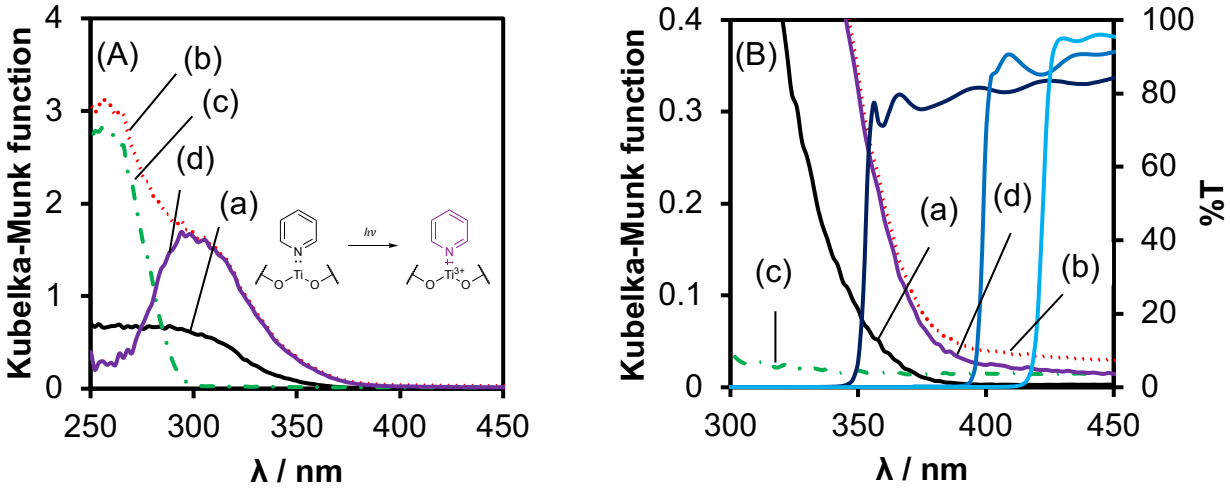

Fig. 2 (A) DR UV-vis spectra of the $BaSO_4$ diluted TiO_2 sample (a), the pyridine adsorbed diluted TiO_2 sample (b), $BaSO_4$ with pyridine (c) and the difference spectrum of b−c (d). Embedded scheme represents the possible photoexcitation of the pyridine-TiO_2 surface complex. (B) The enlarged view of Fig. 2A with the transmission spectra of the cut-off filters (λ > 350, 400, and 422 nm) used in reaction tests.

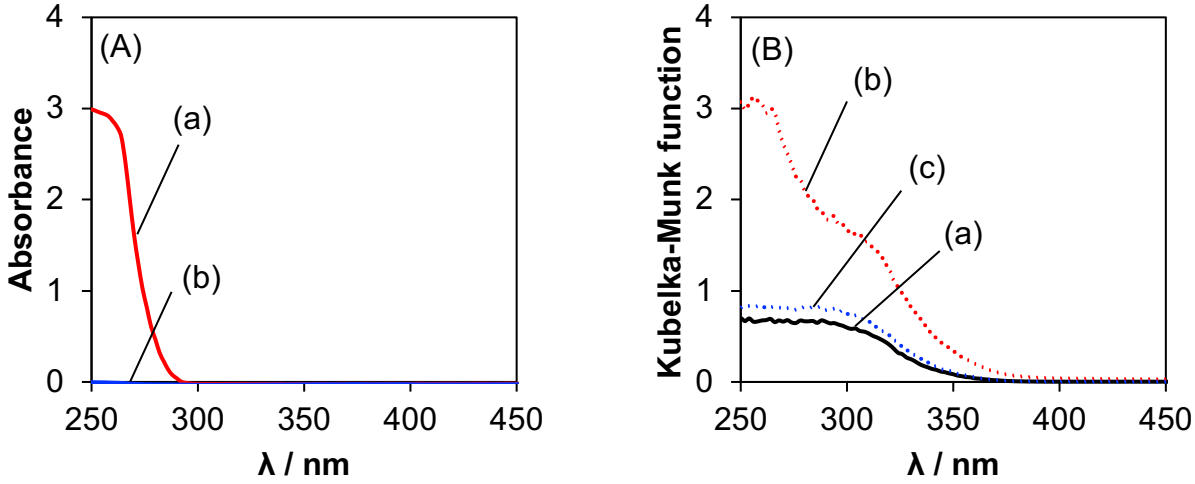

Fig. 3 (A) Absorption spectra of pyridine (a) and cyclohexane (b) recorded in a transmission mode. Pyridine was diluted by cyclohexane solvent. (B) Diffuse reflectance UV-vis spectra of the $BaSO_4$ diluted TiO_2 sample (a), that with pyridine (b), and that with cyclohexane (c).

Isotopic experiment

To elucidate the difference in the reaction mechanism under the alternative irradiation conditions, isotope experiments were carried out. Table 2 shows the results. In the presence of UV light, the yields of CHPs and BCH in the reaction between pyridine and cyclohexane-d_{12} were smaller than those in the reaction with normal reagents (Table 5, entries 1 and 2), where the k_H/k_D values were more than unity, i.e., 1.8 and 3.7 for CHPs and BCH, respectively (kinetic isotope effects, KIEs). Thus, the rate determining step (RDS) in their formation reactions under the light including UV light should be the C–H bond cleavage in cyclohexane. Similarly, the KIE for BPs in the reaction with pyridine-d_5 (Table 5, entry 3, k_H/k_D = 2.1) evidenced that the C–H bond cleavage in pyridine is the RDS of the homo-coupling of pyridine. The formation of both BPs and BCH and these KIEs propose a radical–radical coupling mechanism for the formation of CHPs, in which both pyridine and cyclohexane were activated to become their radical species before their coupling.

In contrast, the k_H/k_D value was less than unity for the homo-coupling of the non-deuterated compound (0.68 for BPs in entry 2 and 0.85 for BCH in entry 3), which can be recognized as the inverse KIEs. In the proposed radical coupling mechanism, both two molecules should be oxidized by the photogenerated holes to become their radical species, meaning that the two oxidation processes competitively consume the limited number of the holes. Therefore, since C–D bond is stronger than C–H bond, the replacement by the deuterated compound would slow down its oxidation rate and instead enhance the oxidation of the other compound, resulting these inverse KIEs for these homo-coupling reactions. This explanation can also be applied to the inverse KIE for CHPs with pyridine-d_5 (Table 5, entry 3, k_H/k_D = 0.87), *i.e.*, the use of pyridine-d_5 would accelerate the oxidation of cyclohexane, which is the RDS in the DCC, and as a result, the formation rate of CHPs was increased.

Considering that both pyridine and cyclohexane are oxidized by holes, it may seem unreasonable that the RDS of the DCC is the C–H bond cleavage in cyclohexane since the amount of cyclohexane is excess and the C–H bond cleavage in cyclohexane is easier than in pyridine in terms of C–H BDE (416.3 kJ mol^{-1} for cyclohexane and 439.3 kJ mol^{-1} for site 2 of pyridine).[24] However, this can be explained by the availability of holes on the TiO_2 surface as follows. In the control experiments, the amount of BCH decreased drastically when the same amount of pyridine was introduced (Table 5), while that of BPs decreased slightly even when cyclohexane was coexistent, meaning that pyridine is preferentially absorbed and oxidized on the TiO_2 surface compared with cyclohexane. Thus, the hole oxidation of cyclohexane was the RDS in the DCC even in this condition. Based on these results, it is clarified that, in the presence of UV light, the DCC reaction starts from the hole oxidation of each molecule to form the radical species followed by a radical coupling.

Table 5 Results of the photocatalytic reaction tests with neat pyridine, neat cyclohexane, and a mixture of them [a]

Entry	Substrate	Products / μmol [b]			
		CHPs	BPs	BCH	CHO
1 [c]	Pyridine	0	51	0	0
2 [d]	Cyclohexane	0	0	40	0.11
3 [e]	Pyridine (50%) + Cyclohexane (50%)	10	31	1.5	0.23

[a] Reaction conditions: the Pt(0.1)/TIO-14 photocatalyst (50 mg) was used, the reaction time was 1 h, the light intensity was 160 mW cm^{-2} measured at 395 ± 35 nm in wavelength, and the irradiation wavelength was $\lambda > 350$ nm. [b] See the caption of Table S1. [c] Pyridine (12 mmol) was used. [d] Cyclohexane (9.3 mmol) was used. [e] Pyridine (5.3 mmol) and cyclohexane (5.3 mmol) were used.

Under visible light irradiation, the hole oxidation by the TiO_2 photocatalyst less occurs. In this condition, the amounts of homo-coupling products were small. The KIEs were observed for yielding CHPs and BCH in the reaction with cyclohexane-d_{12} (entry 5, k_H/k_D = 2.1 and 5.0, respectively), which evidenced that the RDS for their formation reactions under visible light is also the C–H bond cleavage in cyclohexane as well as the case including UV light. The change in the amount of BCH in entry 4 and 6 was too small to discuss. Importantly, almost no change was observed in the yield of CHPs when pyridine-d_5 was used (entry 6, k_H/k_D = 1.0 for CHPs). This clearly different trend from that in the presence of UV light indicates that the reaction mechanism should be different, *i.e.*, the oxidation of pyridine and cyclohexane was not competitive under visible light irradiation.

Table 6 Results of isotope experiments [a]

Entry	λ /nm	Deuterated compound	Product / μmol, (k_H/k_D)[b]				
			CHPs	BPs		BCH	
1	> 350	-	5.4	5.0		5.2	
2		C_6D_{12}	3.2 (1.8)	7.4	(0.68)	1.4	(3.7)
3		C_6D_5N	6.2 (0.87)	2.4	(2.1)	6.1	(0.85)
4	> 400	-	2.9	1.2		0.33	
5		C_6D_{12}	1.4 (2.1)	1.9	(0.63)	0.066	(5.0)
6		C_6D_5N	2.8 (1.0)	0.55	(2.2)	0.37	(0.89)

[a] Reaction conditions: pyridine (0.05 mL, 0.62 mmol) and cyclohexane (0.95 mL, 9.0 mmol) with the Pt(0.1)/TiO_2 photocatalyst (50 mg) were used, the reaction time was 1 h, and light intensity was 160 mW cm^{-2} measured at 395 ± 35 nm in wavelength. [b] The values in parentheses: k_H/k_D = (amount of the products in entry 1) / (that in entry 2 or 3) or (that in entry 4) / (that in entry 5 or 6).

As mentioned above, the DR UV-vis spectroscopy revealed that pyridine forms the surface complex with TiO_2 to be photoexcited even under visible light while cyclohexane does not. Along with the LMCT excitation, pyridine radical cation is generated, and it would be able to react with pyridine or cyclohexane molecules (eqs. 1 and 2). From a calculation of the change of free energy in these reactions (Fig. 4), the reaction with cyclohexane (eq. 2) was found to be more thermodynamically favorable than that with pyridine (eq. 1). It is also confirmed that a direct deprotonation from the pyridine cation radical (eq. 3) is less thermodynamically favored compared with the reaction with cyclohexane (eq. 2).

Moreover, the amount of cyclohexane is in an excess of that of pyridine (typically, the molar ratio of cyclohexane to pyridine was 14.5). Thus, pyridine radical cation would go through the reaction with cyclohexane to give cyclohexyl radical rather than that with pyridine or the deprotonation.

Successively, the DCC reaction would take place in a radical addition-elimination mechanism, where the cyclohexyl radical attacks to pyridine molecule to form an sp^3–centered transition state and a hydrogen radical is eliminated from it. In this case, it seems reasonable that the cleavage of C–D bond in pyridine-d_5 moiety of this transition state would not be the RDS (entry 6, $k_H/k_D = 1.0$ for CHPs). The inverse KIE for BPs yield in the reaction with cyclohexane-d_{12} (entry 5, $k_H/k_D = 0.63$) could be due to an increase in the competitive formation of pyridyl radical via the reaction between the radical cation and pyridine molecules (eq. 1), or a deprotonation of the cation radical (eq. 3), which might be promoted by the other species such as surface hydroxyl group (eq. 4).

$$C_5H_5N^{\bullet+} + C_5H_5N \rightarrow C_5H_5N + {}^{\bullet}C_5H_4N + H^+ \quad (1)$$

$$C_5H_5N^{\bullet+} + C_6H_{12} \rightarrow C_5H_5N + {}^{\bullet}C_6H_{11} + H^+ \quad (2)$$

$$C_5H_5N^{\bullet+} \rightarrow {}^{\bullet}C_5H_4N + H^+ \quad (3)$$

$$C_5H_5N^{\bullet+} + OH_{sur} \rightarrow {}^{\bullet}C_5H_4N + {}^{+}OH_{2,\,sur} \quad (4)$$

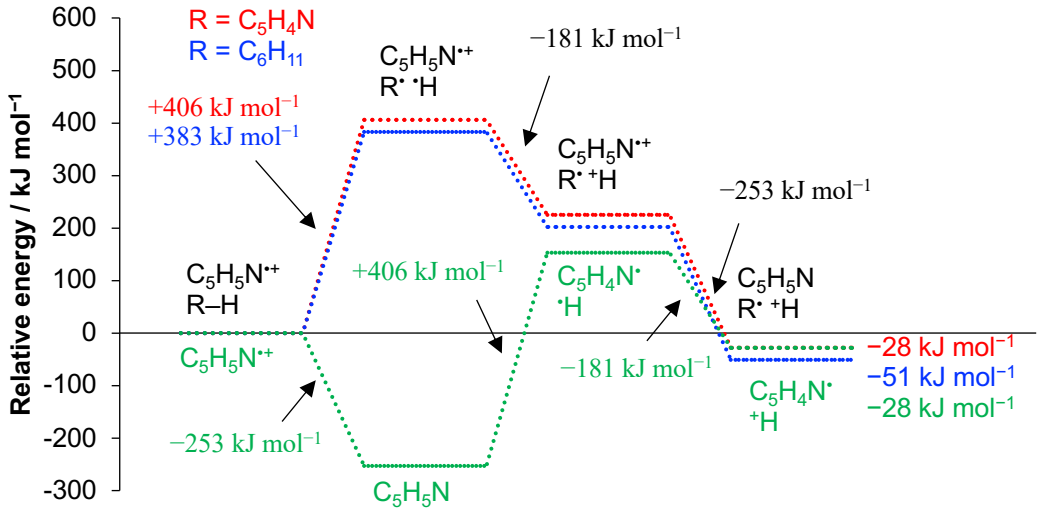

Fig. 4 Energy diagram used for the calculation of the Gibbs energy changes. Gibbs energy in the C–H bond dissociation of pyridine and cyclohexane were calculated to be 406 and 383 kJ mol^{-1}, respectively, where the values were given from the BDEs in pyridine and cyclohexane (439.3 for site 2 and 416.3 kJ mol^{-1}, respectively) minus the entropy factor ($T\Delta S$, taken in all the cases as 33 kJ mol^{-1} at 298 K).[28,29] The oxidation potential of H$^{\cdot}$ to H$^+$ was −1.87 V (vs SCE) in acetonitrile,[28,29] which is the same for the two reactions. The one electron oxidation potential of pyridine was 1.82 V (vs Ag/Ag$^+$),[30] which is also the same.

Temperature control test

In this system, without the deposited metal nanoparticles, the bare TiO_2 photocatalyst was less active (Table 2, entry 1). The addition of Pt on the TiO_2 photocatalyst enhanced the reaction rate (Table 2, entry 2), and Pt was most suitable among the metal cocatalyst tested (Table 2, entries 3–5). It is well accepted that metal nanoparticles loaded on photocatalysts are considered to act as an electron receiver to promote charge separation in the excited photocatalyst,[18–20,31] while it has been noticed that in some cases they can also work as a metal catalyst, *e.g.*, for C–H activation of hydrocarbons.[32] Thus, we carried out temperature control tests under the alternative irradiation conditions to elucidate the possibility of Pt metal catalysis in the DCC between pyridine and cyclohexane. Fig. 5 showed the results in the pseudo-Arrhenius plots for the production rate of CHPs in the reactions with a pristine or Pt loaded sample under photoirradiation of UV and visible light (Fig. 5A) or only visible light (Fig. 5B). The yield of CHPs increased with increasing the reaction temperature regardless of the irradiation condition and the sample. The plots for each reaction system were almost in a straight line. The thermal activation energies were calculated from the slopes of the approximation lines and summarized in Table 3. The activation energies for the DCC reaction with the pristine and Pt loaded samples were almost the same values, *i.e.*, 41 and 40 kJ mol^{-1} under UV and visible light (Table 7, entries 1 and 2) and 22 and 28 kJ mol^{-1} under visible light (Table 7, entries 3 and 4). This indicates that Pt did not contribute to the thermal activation process, *i.e.*, the reaction takes place without Pt metal catalysis. Also, the Pt loaded sample showed better activity than the pristine sample for the reaction in both irradiation condition (Fig. 5, A and B). This means that the Pt nanoparticles contribute to the higher reaction rate except for the thermal catalysis. Therefore, the role of Pt should be the electron receiver to suppress the recombination of electrons and holes under both irradiation conditions. Furthermore, the activation energies obtained under UV and visible light (Table 7, entries 1 and 2) was larger than that under visible light (Table 7, entries 3 and 4). This means that the dark process requires more energy in the TiO_2 photocatalysis as a main reaction under UV light. It could be due to the difference in the place where holes are generated. Since holes are generated in bulk TiO_2 under the light including UV light, they need thermal energy to migrate to the surface before the reaction with the substrates. On the other hand, under visible light, holes are generated in the adsorbed pyridine to form the radical cation on the TiO_2 surface. This means that the holes can be directly used without migration. This would be the reason why the thermal energy required under visible light was smaller than that under the light of UV and visible.

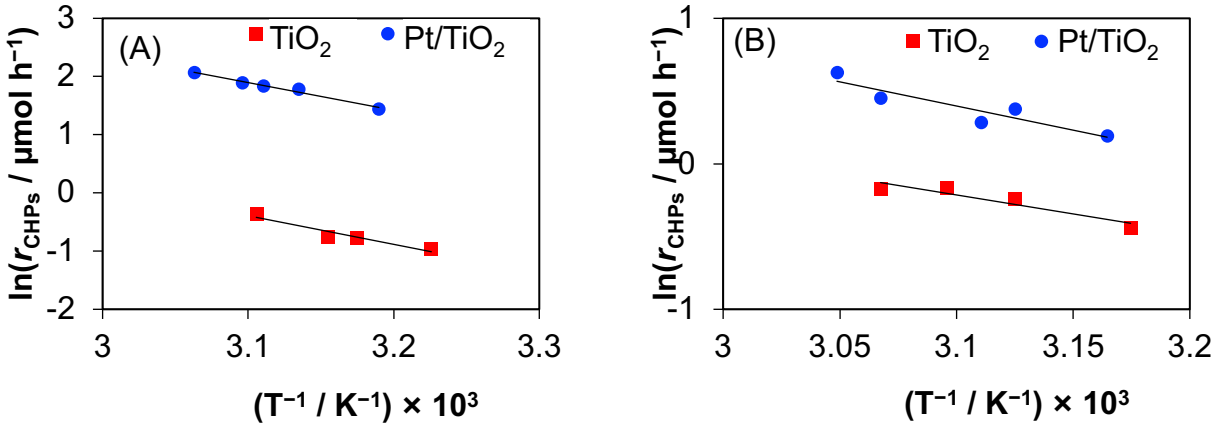

Fig. 5 Pseudo-Arrhenius plots of the CHPs formation rate (r_{CHPs}) for the temperature controlled reactions between pyridine and cyclohexane with a pristine TiO_2 (red squares) or Pt(0.1)/TiO_2 (blue circles) under UV and visible light (A) and visible light (B). The amount of CHPs at the initial stage with low conversion was used for the calculation of the formation rate of CHPs.

Table 7 Summary of the activation energy for the formation of CHPs

Entry	λ / nm	Photocatalyst	$E_{a,\ CHPs}$ / kJ mol^{-1}
1	> 350	TiO_2	41
2		Pt(0.1)/TiO_2	40
3	> 400	TiO_2	22
4		Pt(0.1)/TiO_2	28

Reaction mechanism

Based on all the results, we propose tentative reaction mechanism as follows.

Under the irradiation including UV light (Fig. 6A), the TiO_2 photocatalyst is excited to give the photogenerated electrons and holes in the conduction band and the valence band, respectively. The electrons were transferred to the Pt nanoparticles while the holes were trapped on the TiO_2 surface (scheme i). Pyridine and cyclohexane are competitively oxidized by the holes to the corresponding radical species (schemes ii and iii). Then, the radical-radical coupling of these radicals affords the DCC products (CHPs, scheme iv) as well as the homo-coupling products (BPs and BCH, schemes v and vi). Protons are reduced by the electrons on the Pt co-catalyst to give a molecular hydrogen (scheme vii). This is a two-photon process (Fig. 6A). Role of Pt cocatalyst is a charge separator to suppress the recombination of the electrons and holes. Although the visible light excitation of the surface pyridine complexes should also occur at the same time and partially contribute to the DCC product formation, the TiO_2 photocatalysis mentioned above would be predominant.

On the other hand, under visible light irradiation (Fig. 6B), the surface complex consisting of adsorbed pyridine and Ti cation, in which the acid-base N–Ti coordination bond is formed by using a lone pair of nitrogen (scheme viii), is photoexcited to generate an excited electron from the lone pair

and a hole remains in a pyridine radical cation (scheme ix). The electron is injected to the conduction band of TiO_2 *via* the surface Ti cation, followed by a transfer to the deposited Pt nanoparticles. The pyridine radical cation (the hole) oxidizes cyclohexane to form cyclohexyl radical and a proton (scheme x), and the DCC proceeds between the cyclohexyl radical and the pyridine molecule in a radical addition-elimination process, *i.e.*, the attack of the radical species to the pyridine to form an sp^3-centered transition state and an elimination of hydrogen radical from the transition state (scheme xi and xii). The hydrogen elimination from the transition state would be more preferred than other possibilities, for example, although one may consider another possibility that the second photon absorption may occur on the sp^3-centered radical species to release a proton, the photoexcitation of the transition state is usually difficult. Although the possibility that the other species may facilitate the release of the hydrogen radical is not excluded, the scheme xii itself would be thermodynamically favorable since the molecule regain its aromaticity by releasing a H radical. Apart from the LMCT sites, the proton is reduced by the electron on the Pt nanoparticle, followed by the reaction with the hydrogen radical to give a molecular hydrogen (scheme xiii).

The reaction under visible light should be a one-photon process (Fig. 6B). In this mechanism, the generation of pyridine radical cation takes place instead of hole oxidation of pyridine, and the pyridine radical cation is responsible for the oxidation of cyclohexane. Since thus produced cyclohexyl radical should be close to the pyridine when it was formed (scheme x), the collision frequency between the two (scheme xi) would be large, and this could explain the suppression of homo-coupling of cyclohexane. Pt co-catalyst works as the electron receiver to suppress the recombination of the electrons and the cation radical.

In the presence of UV light

$$Pt/TiO_2 + h\nu \rightarrow e^-_{Pt} + h^+_{TiO2} \quad \text{(i)}$$

$$C_5H_5N + h^+_{TiO2} \rightarrow {}^{\bullet}C_5H_4N + H^+ \quad \text{(ii)}$$

$$C_6H_{12} + h^+_{TiO2} \rightarrow {}^{\bullet}C_6H_{11} + H^+ \quad \text{(iii)}$$

$${}^{\bullet}C_5H_4N + {}^{\bullet}C_6H_{11} \rightarrow C_{11}H_{10}N \text{ (CHPs)} \quad \text{(iv)}$$

$${}^{\bullet}C_5H_4N + {}^{\bullet}C_5H_4N \rightarrow C_{10}H_8N_2 \text{ (BPs)} \quad \text{(v)}$$

$${}^{\bullet}C_6H_{11} + {}^{\bullet}C_6H_{11} \rightarrow C_{12}H_{22} \text{ (BCH)} \quad \text{(vi)}$$

$$2H^+ + e^-_{Pt} \rightarrow H_2 \quad \text{(vii)}$$

Under visible light

$$C_5H_5N + TiO_2 \rightarrow C_5H_5N–TiO_2 \text{ (surface complex)} \quad \text{(viii)}$$

$$C_5H_5N–TiO_2 \text{ (surface complex)} \rightarrow C_5H_5N^{\bullet+} + TiO_2 (e^-_{Pt}) \quad \text{(ix)}$$

$$C_5H_5N^{\bullet+} + C_6H_{12} \rightarrow C_5H_5N + {}^{\bullet}C_6H_{11} + H^+ \quad \text{(x)}$$

$$C_5H_5N + {}^{\bullet}C_6H_{11} \rightarrow [C_5H_5N–C_6H_{11}]^{\bullet} \quad \text{(xi)}$$

$$[C_5H_5N–C_6H_{11}]^{\bullet} \rightarrow C_{11}H_{10}N \text{ (CHPs)} + H^{\bullet} \quad \text{(xii)}$$

$$H^+ + H^{\bullet} + e^-_{Pt} \rightarrow H_2 \quad \text{(xiii)}$$

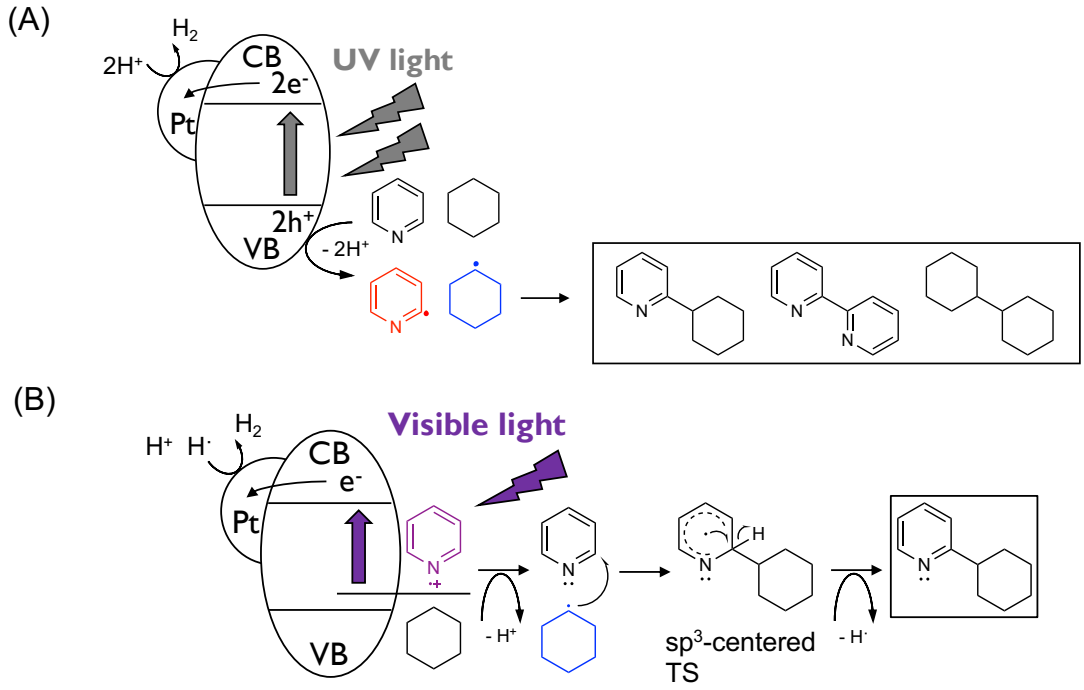

Fig. 6 Schematic image of tentative reaction mechanism under UV and visible light (A), and visible light (B). 2-CHP and 2,2'-BP were chosen as representative products among CHPs and BPs, respectively.

In each reaction tests, the yield was low. One of the reasons for that could be an insufficient number of the LMCT complex due to a limited number of the adsorption site. Thus, further study could be made to increase the LMCT sites by some methods such as surface treatment. Another reason could be an insufficient use of the LMCT band. In the current system, severe limitation of the irradiation wavelength was required to exclude the TiO_2 photoexcitation due to the large overlap of the absorption bands of LMCT and TiO_2, resulting in the limited use of the LMCT band, which leads to the low activity. Thus, to shift the LMCT band toward lower energy, surface modification of TiO_2 or use of

the molecules having higher HOMO level than that of pyridine might be helpful. If it is possible to use other photocatalyst having a positive valance band than TiO_2, it is more preferred.

Conclusion

Selective DCC reaction between pyridine and cyclohexane can be achieved by the unique reaction mechanism through the LMCT excitation of the acid-base interacted heteroaromatic surface complex consisting of pyridine and TiO_2 under visible light irradiation. Although the yield of the reaction is not satisfying, this study showed the possibility of wide use of aromatic-semiconductor surface complex system for DCC, in which the selectivity can be improved just by changing the irradiation wavelength without any additives or modification of the photocatalyst.

References

1. Hashimoto, K., Irie, H. & Fujishima, A. TiO_2 Photocatalysis: A Historical Overview and Future Prospects. *Jpn. J. Appl. Phys.* **44**, 8269–8285 (2005).
2. Fox, M. A. & Dulay, M. T. Heterogeneous Photocatalysis. *Chem. Rev.* **93**, 341–357 (1993).
3. Carp, O., Huisman, C. L. & Reller, A. Photoinduced reactivity of titanium dioxide. *Prog. Solid State Chem.* **32**, 33–177 (2004).
4. Palmisano, G., Augugliaro, V., Pagliaro, M. & Palmisano, L. Photocatalysis: a promising route for 21st century organic chemistry. *Chem. Commun.* 3425–3437 (2007).
5. Kisch, H. Semiconductor photocatalysis - Mechanistic and synthetic aspects. *Angew. Chemie Int. Ed.* **52**, 812–847 (2013).
6. Oi, L. E. *et al.* Recent advances of titanium dioxide (TiO_2) for green organic synthesis. *RSC Adv.* **6**, 108741–108754 (2016).
7. Higashimoto, S. *et al.* Selective photocatalytic oxidation of benzyl alcohol and its derivatives into corresponding aldehydes by molecular oxygen on titanium dioxide under visible light irradiation. *J. Catal.* **266**, 279–285 (2009).
8. Zhang, G., Kim, G. & Choi, W. Visible light driven photocatalysis mediated via ligand-to-metal charge transfer ({LMCT}): an alternative approach to solar activation of titania. *Energy Environ. Sci.* **7**, 954–966 (2014).
9. Higashimoto, S. *et al.* Selective Photocatalytic Oxidation of Benzyl Amine By O_2 Into N-Benzylidenebenzylamine on TiO_2 Using Visible Light. *Curr. Org. Chem.* **17**, 2374–2381 (2013).
10. Lang, X. *et al.* Visible-light-induced selective photocatalytic aerobic oxidation of amines into imines on TiO_2. *Chem. - A Eur. J.* **18**, 2624–2631 (2012).
11. Lang, X. *et al.* Tertiary amine mediated aerobic oxidation of sulfides into sulfoxides by visible-light photoredox catalysis on TiO_2. *Chem. Sci.* **6**, 5000–5005 (2015).

12. Liu, C., Liu, D. & Lei, A. Recent advances of transition-metal catalyzed radical oxidative cross-couplings. *Acc. Chem. Res.* **47**, 3459–3470 (2014).
13. Yeung, C. S. & Dong, V. M. Catalytic dehydrogenative cross-coupling: Forming carbon-carbon bonds by oxidizing two carbon-hydrogen bonds. *Chem. Rev.* **111**, 1215–1292 (2011).
14. Fagnoni, M., Dondi, D., Ravelli, D. & Albini, A. Photocatalysis for the formation of the C-C bond. *Chem. Rev.* **107**, 2725–2756 (2007).
15. Yamamoto, A., Ohara, T. & Yoshida, H. Visible-light-induced photocatalytic benzene/cyclohexane cross-coupling utilizing a ligand-to-metal charge transfer benzene complex adsorbed on titanium oxides. *Catal. Sci. Technol.* **8**, 2046–2050 (2018).
16. Cui, X. & Brown, R. S. Mechanistic Evaluation of the Halocyclization of 4-Penten-1-ol by Some Bis (2-substituted pyridine) and Bis (2 , 6-disubstituted pyridine) bromonium Triflates. *J. Org. Chem.* **65**, 5653–5658 (2000).
17. Almeida, A. R., Moulijn, J. a & Mul, G. Photocatalytic Oxidation of Cyclohexane over TiO_2 : Evidence for a Mars-van Krevelen. *J. Phys. Chem. C* **115**, 1330–1338 (2011).
18. Wang, C. M., Heller, A. & Gerischer, H. Palladium catalysis of O_2 reduction by electrons accumulated on TiO_2 particles during photoassisted oxidation of organic compounds. *J. Am. Chem. Soc.* **114**, 5230–5234 (1992).
19. Subramanian, V., Wolf, E. E. & Kamat, P. V. Catalysis with TiO_2/Gold Nanocomposites. Effect of Metal Particle Size on the Fermi Level Equilibration. *J. Am. Chem. Soc.* **126**, 4943–4950 (2004).
20. Yang, J., Wang, D., Han, H. & Li, C. Roles of cocatalysts in photocatalysis and photoelectrocatalysis. *Acc. Chem. Res.* **46**, 1900–1909 (2013).
21. Yoshida, H., Fujimura, Y., Yuzawa, H., Kumagai, J. & Yoshida, T. A heterogeneous palladium catalyst hybridised with a titanium dioxide photocatalyst for direct C-C bond formation between an aromatic ring and acetonitrile. *Chem. Commun.* **49**, 3793–3795 (2013).
22. Tyagi, A., Matsumoto, T., Kato, T. & Yoshida, H. Direct C – H bond activation of ethers and successive C – C bond formation with benzene by a bifunctional palladium-titania photocatalyst. *Catal. Sci. Technol.* **6**, 4577–4583 (2016).
23. Wada, E. *et al.* Direct cyanomethylation of aliphatic and aromatic hydrocarbons with acetonitrile over a metal loaded titanium oxide photocatalyst. *Catal. Sci. Technol.* **7**, 2457–2466 (2017).
24. Ruo, Y. R. *Comprehensive Handbook of Chemical Bond Energies*. (CRC Press, 2007).
25. Bezrodna, T. *et al.* Pyridine-TiO_2 surface surface interaction as a probe for surface active centers analysis. *Appl. Surf. Sci.* **214**, 222–231 (2003).
26. Shishido, T., Teramura, K. & Tanaka, T. A unique photo-activation mechanism by “in situ doping” for photo-assisted selective NO reduction with ammonia over TiO_2 and photooxidation of alcohols over Nb_2O_5. *Catal. Sci. Technol.* **1**, 541 (2011).
27. Heilbronner, E., V.Hornung, R.Pinkerton, F. & Thames, S. F. Photoelectron Spectra of

Azabenzenes and Azanaphthalenes: III. The Orbital Sequence in Methyl- and Trimethylsilyl-Substituted Pyridines. *Helv. Chim. Acta* **55**, 289–302 (1972).

28. Baciocchi, E., Del Giacco, T. & Elisei, F. Proton-Transfer Reactions of Alkylaromatic Cation Radicals. The Effect of α-Substituents on the Kinetic Acidity of p-Methoxytoluene Cation Radicals. *J. Am. Chem. Soc.* **115**, 12290–12295 (1993).
29. Baciocchi, E., Del Giacco, T., Lanzalunga, O., Mencarelli, P. & Procacci, B. Photosensitized oxidation of alkyl phenyl sulfoxides. C-S bond cleavage in alkyl phenyl sulfoxide radical cations. *J. Org. Chem.* **73**, 5675–5682 (2008).
30. Weinberg, N. L. & Weinberg, H. R. Electrochemical oxidation of organic compounds. *Chem. Rev.* **68**, 449–523 (1968).
31. Bard, A. J. Photoelectrochemistry. *Science.* **207**, 139–144 (1980).
32. Tyagi, A., Yamamoto, A., Kato, T. & Yoshida, H. Bifunctional property of Pt nanoparticles deposited on TiO_2 for the photocatalytic sp^3 C–sp^3 C cross-coupling reactions between THF and alkanes. *Catal. Sci. Technol.* **7**, 2616–2623 (2017).

Chapter 2

Minisci-type reaction between pyridine and tetrahydrofuran through a photoexcitation of surface Ti-peroxo species

Abstract

Photocatalytic Minisci-type functionalization of pyridine with tetrahydrofuran (THF) proceeded using hydrogen peroxide (H_2O_2) and a TiO_2 photocatalyst under acidic conditions. Under UV light (λ = 360 nm), the reaction selectivity based on pyridine (S_{py}) was >99% while the selectivity based on THF (S_{THF}) was low such as 19%. In contrast, under visible light (λ = 400 or 420 nm) S_{py} was similarly high (>99%) and S_{THF} was two times higher than that under UV light. A surface peroxo complex formed upon contact of hydrogen peroxide with the TiO_2 surface can be selectively photoexcited by visible light to inject the photoexcited electron to the conduction band of TiO_2. The electron can reduce H_2O_2 to a reactive oxygen species (ROS) and promote selectively the Minisci-type cross-coupling reaction between pyridinium ions and THF. A reaction test with a hole scavenger (methanol) evidenced that the hole oxidation of H_2O_2 under UV light is responsible for the lower selectivity, in other words, the higher selectivity under visible light would be due to suppression of the hole oxidation of H_2O_2. These results demonstrate a novel way to improve the selectivity of the photocatalytic cross-coupling reaction by using H_2O_2 as an oxidant with the photoexcitation of surface Ti-peroxo species on TiO_2.

Introduction

Titanium dioxide (TiO_2), the first semiconductor photocatalyst, has attracted much attention as one of the most practical photocatalyst with high oxidation ability, chemical stability, and low cost.[1,2] In typical oxidation process with TiO_2 photocatalyst, reactive oxygen species (ROS) such as hydrogen peroxide, hydroxyl radical, and superoxide anion radical, has been considered as key intermediates,[3,4] which strongly correlates with efficiency of the system.[5] For instance, hydrogen peroxide can be used to accelerate the formation of hydroxyl radical and improve the activity in photocatalytic degradation of organic wastes.[6]

There is no doubt that these ROS formed with TiO_2 photocatalyst are available for not only degradation but also other synthetic reactions such as oxidative cross-coupling reactions, which is one of the most important reactions to build a carbon–carbon bond in organic molecules. Only a few studies, however, have been reported for the oxidative cross-coupling reactions so far,[7,8] which would be because of low selectivity. To apply the TiO_2 photocatalysis to cross-coupling under high ROS concentration, the selectivity to the coupling must be improved.

One of the ways to improve the selectivity of the TiO_2 photocatalysis is to use photoexcitation of ligand-to-metal charge transfer (LMCT) complex consisting of adsorbed molecules and the surface of photocatalyst.[9] The LMCT complex systems have achieved several selective photooxidation reactions of various compounds such as alcohols,[10] amines,[11,12] and sulphides.[13] Recently, we found that the LMCT system can also be applied to sp^2C–sp^3C cross-coupling between aromatic ring and alkane through the LMCT of aromatic surface complex.[14,15] In this chapter, we utilized an LMCT excitation of surface peroxo complex on TiO_2 to achieve high selectivity of photocatalytic organic transformation involving the generation of ROS. We chose Minisci-type functionalization of pyridine with tetrahydrofuran (THF) by using hydrogen peroxide in acidic conditions as the first trial (eq. 1).[8] The effect of irradiation wavelength on the reaction was investigated and several scavenging tests were also carried out to clarify the reaction mechanism. We found that that selective excitation of the peroxo surface complex by visible light can improve the selectivity of the cross-coupling by suppressing the undesired oxidation of H_2O_2.

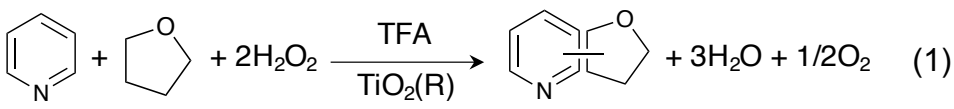

(1)

Experimental

Catalyst preparation

A rutile TiO_2 powder sample (JRC-TIO-6, 100 m^2 g^{-1}) donated by the Catalysis Society of Japan was employed. In some experiments, 0.1 wt% Pd-loaded TiO_2 catalyst was used since our previous studies showed the positive effect of Pd cocatalyst for some organic reactions.[16–18] The catalysts were referred to as Pd/TiO_2.

Reaction test

Materials. All the chemicals employed for the photocatalytic reaction tests were of analytical grade and were used without further purification; pyridine (Nacalai Tesque, 99.7 %), tetrahydrofuran (THF, Nacalai Tesque, >99.5%), hydrogen peroxide (Nacalai Tesque, 30%), trifluoroacetic acid (TFA, Santa Cruz Biotechnology, >99%).

Procedure for the reaction tests. Typical procedure is as follows. Before a photocatalytic reaction test, a photocatalyst sample (TiO_2 or Pd/TiO_2, 50 mg) in a Pyrex glass tube (20 mL or 50 mL) was subjected to pre-treatment for 30 min under the light from a ceramic xenon lamp (PE300BUV, 300 W) to clean its surface. Then, a reaction mixture (2.054 mL in total) of pyridine, THF, H_2O_2 aqueous solution (30%), and TFA were added into the test tube. The resultant mixture was a yellowish suspension. After that, the test tube was sealed with a rubber septum and the mixture was bubbled by argon for 10 min under magnetic stirring to remove the air. The reaction mixture was irradiated by using another 300 W xenon lamp (Asahi Spectra Co., Ltd. MAX-302) with stirring for a desired reaction time at room temperature. The irradiation wavelength was limited by a band-pass filter (MX0360 (λ = 360±10 nm), MX0400 (λ = 400±10 nm), MX0420 (λ = 420±10 nm)). After the irradiation, 0.5 mL of the gaseous phase was collected by an air-tight syringe and analyzed by a GC-TCD (Shimadzu, GC-8A). The reaction mixture in the liquid phase was sampled by a syringe with a PTFE filter to remove the photocatalyst, and then analyzed by a GC-MS (Shimadzu, GCMS-QP2020). The analysis was carried out without neutralization.

Desired product, tetrahydrofuranylpyridine (TP), was quantified by using a GC-MS calibration curve of 2-cyclohexylpyridine. Three peaks for the isomers of TP were obtained and their peak areas were always in a ratio of 3:1:1, sum of which was treated as the desired products (TPs) in the present study and used to calculate the TPs yield in the reaction tests. By-products observed were some oxidized THF (OTs: 2-hydroxytetrahydrofuran, γ-butyrolactone,

and α-hydroxy-γ-butyrolactone), which were quantified using the calibration curve of authentic samples purchased from companies. The remaining H_2O_2 in the reaction mixture was quantified by iodometry.

Diffuse reflectance UV-vis spectroscopy

UV-vis spectra of the powder samples were recorded in a diffuse reflectance (DR) mode. The samples were diluted 100 times by $BaSO_4$. For the samples with an adsorbate, 50 μL of the reaction mixture (a mixture of pyridine, THF, TFA, and H_2O_2 aq.) or 30 % H_2O_2 aqueous solution was added to the diluted samples, followed by 10 min of mixing. Then, desired amount of the sample was taken into the cell to fix the amount of TiO_2 in the samples and the spectrum was measured using a UV-vis spectrophotometer (JASCO V-570) equipped with an integrating sphere, where $BaSO_4$ was used as a reference.

Results and discussion

Diffuse reflectance UV-vis spectroscopy

The visible-light responsive species in this system was first confirmed by diffuse reflectance UV-vis spectroscopy (Fig. 1). The TiO_2 sample in the presence of the reaction mixture (pyridine, THF, and TFA) without H_2O_2 was white and its spectrum (Fig. 1b) was almost similar with that of the sample without the reaction mixture (Fig. 1a), where the increase in the baseline was probably due to the liquid phase. This suggests that a reported surface complex formed with an acid-base interaction between a pyridine molecule and a Ti cation on TiO_2 surface[15] is not the case in the present acidic conditions. This would be due to protonation of pyridine molecules by the acid (TFA). In contrast, the H_2O_2 containing sample was yellowish and its spectrum showed an additional visible-light absorption band in the range of 400–500 nm in wavelength compared with the other two samples (Fig. 1c). This is attributed to the presence of surface Ti-peroxo species.[19]

It is reported that H_2O_2 is adsorbed on TiO_2 to form some surface Ti-peroxo species and changes the catalyst's color into yellow.[19] Three types of the surface peroxo species have been proposed: end-on, bridged,[20] and side-on (Scheme 1).[21,22] The former two species exist mainly on anatase TiO_2, while the latter does on rutile TiO_2.[21] The color change by H_2O_2 adsorption was also observed in zeolitic titanium-silicate systems[23] and the side-on peroxo is regarded as

the visible-light responsive species because of its similar spectroscopic features with the model compound.[24] Thus, it is suggested that the visible-light responsive species in the present system with the rutile TiO_2 sample is the side-on species. The end-on species is another candidate since the side-on species would be protonated under acidic conditions in the presence of TFA (eq. 2). Since TiO_2 is excited by UV light only, the reaction under visible light would start from the photoexcitation of the surface peroxo species.

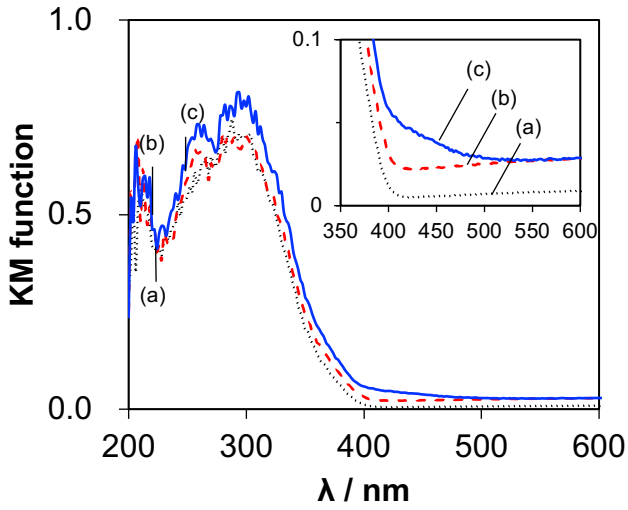

Fig. 1 DR UV-vis spectra of (a) the TiO_2 sample diluted by $BaSO_4$, (b) the diluted sample with the reaction mixture (pyridine, THF, TFA) except for H_2O_2, and (c) that with the reaction mixture including H_2O_2.

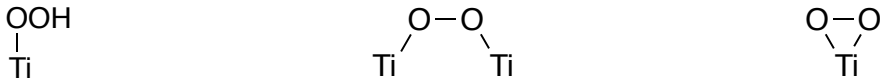

(a) (b) (c)

Scheme 1 Possible structure of surface Ti-peroxo species: (a) end-on, (b) bridged, and (c) side-on.

$$O_2\text{–Ti (side-on)} + H^+ \rightleftarrows \text{HOO–Ti (end-on)} \qquad (2)$$

Reaction tests

Next, reaction tests were carried out using the pristine rutile TiO_2 sample under the light of variously limited wavelength (Table 1). The reaction took place under UV light (λ = 360±10 nm) and afforded 1.8 μmol of tetrahydrofuranylpyridine (TPs) as the cross-coupling products, which corresponds to 0.85% yield in 1 h (Table 1, entry 1). By-products from pyridine such as 2,2'-bipyridyl, 2,3'-bipyridyl, and 2,4'-bipyridyl were not observed. This means that the selectivity to TPs based on pyridine (S_{py}) was >99%. On the other hand, 6.8 μmol of some

oxidized by-products of THF (OTs) was obtained, in which the selectivity to TPs based on THF (S_{THF}) was low such as 19% even in the initial stage of the reaction.

When the reaction test was carried out under visible light (λ = 400±10 nm, Table 1, entry 2), the amount of the products was higher than that under UV light due to higher light intensity from the lamp; 8.6 μmol of TPs and 15 μmol of OTs were produced. The yield and S_{THF} were five and two times higher than that under UV-light such as 4.3% and 37%, respectively. The TPs selectivity based on pyridine was as high as the case under UV light (S_{py} >99%). The reaction proceeded even under longer-wavelength light (λ = 420±10 nm) and the selectivity obtained was the highest such as 40% among them (Table 1, entry 3). The higher S_{THF} under visible light than that under UV light means that the formation of OTs was suppressed under visible light irradiation. The amount of H_2O_2 in the solution was decreased after reaction in all cases. The yield of TPs was drastically decreased in the absence of H_2O_2 under both UV and visible light (Table 1, entries 4 and 5), which indicates that H_2O_2 is essential as an oxidant to produce TPs. The reaction also hardly proceeded in the air without H_2O_2 under UV light (Table 1, entry 6)**.** TPs were not produced in the absence of TFA in both light conditions (Table 1, entries 7 and 8), suggesting that TPs are formed through a Minisci-type mechanism, which involves protonation of pyridine by TFA, an attack of a THF radical to a pyridinium ion (discussed below), and subsequent elimination of a hydrogen atom (Scheme 2). The active species produced from H_2O_2 could promote production of THF radical.

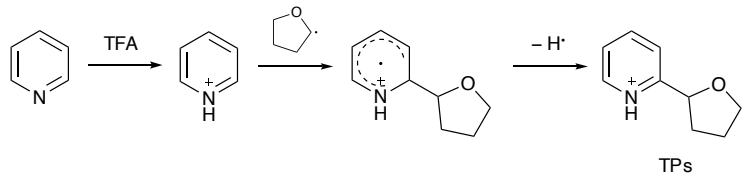

Scheme 2 Minisci reaction between pyridine and THF in the presence of TFA. 2,2'-tetrahydrofuranylpyridine was chosen a representative example for TPs.

In these reaction tests (Table 1, entries 1–3), the amount of consumed H_2O_2 was much larger than the product yield. Thus, it must be noted that H_2O_2 molecules and the surface peroxo species would largely decompose during the reaction in vain. We carried out a long-time reaction test under visible light (Fig. 2A), where the reaction scale was two times larger than usual. The reaction stopped and the yellowish color of the catalyst disappeared after 8 h when the yield of TPs and conversion of H_2O_2 reached 14 % and 81 %, respectively. As suggested from the result of DR UV-vis spectroscopy, the reaction under visible light would start from not the photoexcitation of TiO_2 photocatalyst but the photoexcitation of the surface Ti-peroxo species. The termination of the reaction with the decolorization also indicates that the surface

Table 1 Results of reaction tests under photoirradiation with the light of variously limited wavelength[a]

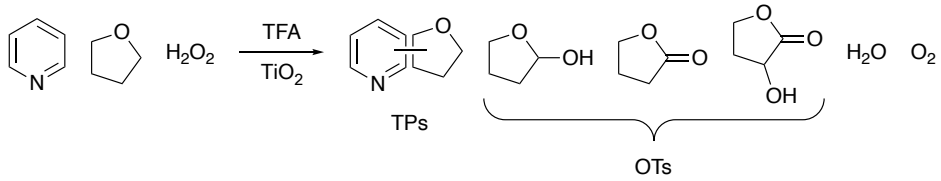

Entry	Additive / mmol		λ / nm	Light intensity[b] / mW cm^{-2}	Products[c] / μmol		Consumed H_2O_2[d] / μmol	Yield of TPs[e]	Conversion of H_2O_2 (%)	Selectivity[f] (%)	
	H_2O_2	TFA			TPs	OTs				S_{py}	S_{THF}
1	0.2	0.2	360	1	1.8	6.9	63	0.85	31	>99	19
2	0.2	0.2	400	9	8.6	15	100	4.3	50	>99	37
3	0.2	0.2	420	13	6.9	10	82	3.5	41	>99	40
4	0	0.2	360	1	0.14	1.8	-	0.068	-	>99	7.1
5	0	0.2	420	13	0.26	1.8	-	0.13	-	>99	12
6[h]	0	0.2	360	1	n.d.[g]	n.d.[g]	-	0	-	0	0
7	0.2	0	360	1	n.d.[g]	16	81	0	40	0	0
8	0.2	0	420	13	n.d.[g]	22	97	0	49	0	0
9	0.2	0.2	dark	-	n.d.[g]	3.4	18	0	9.2	0	0
10[i]	0.2	0.2	dark	-	n.d.[g]	3.6	12	0	5.9	0	0
11	0.2	0	dark	-	n.d.[g]	8.1	54	0	27	0	0
12[j]	0.2	0	dark	-	n.d.[g]	11	82	0	41	0	0

[a] Reaction conditions: pyridine (0.2 mmol), THF (24 mmol), 30 % H_2O_2 aq. (0–22.5 μl, 0–0.2 mmol of H_2O_2), and TFA (0–0.2 mmol) with the TiO_2 photocatalyst (50 mg) were used and the reaction time was 1 h. The reaction tests were carried out in a Pyrex test tube (20 mL). [b] The light intensity was measured at 355 ± 45 nm for 360-nm UV light and at 415 ± 55 nm for 400- or 420-nm visible light in wavelength. [c] TPs: total amount of tetrahydrofuranylpyridine. OTs: total amount of 2-hydroxytetrahydrofuran, γ-butyrolactone, and α-hydroxy-γ-butyrolactone. [d] The amount of consumed H_2O_2 after reaction calculated as (amount of added H_2O_2 (μmol)) – (amount of H_2O_2 in the reaction solution after reaction) (μmol)). [e] Yield of TPs based on the introduced pyridine. [f] Selectivity to TPs. The selectivity based on pyridine was calculated as S_{py} = [100 × TPs (μmol)]/[(TPs + byproducts from pyridine) (μmol)]; the selectivity based on THF was calculated as S_{THF} = [100 × TPs (μmol)]/[(TPs + OTs) (μmol)]. [g] Not detected. [h] Reaction in the air. [i] Reaction time was 8 h. [j] Reaction time was 4 h.

peroxo species is necessary to promote the reaction under visible-light irradiation, *i.e.*, the reaction cannot proceed without the surface peroxo species. Since the peroxo species would be present on the surface in an equilibrium with the H_2O_2 molecules in the liquid phase,[23] it should almost disappear when the H_2O_2 concentration in liquid phase decreased. As another possibility, the surface peroxo species might decompose during the reaction. Additional long-time reaction test was carried out with a Pd loaded sample (Fig. 2B), followed by the addition of H_2O_2 after 12 h. It was found that the addition of 0.4 mmol of H_2O_2 after the reaction termination recovered the catalyst's color and the activity. This indicates that the surface Ti-peroxo species can be regenerated when H_2O_2 was supplied. However, further addition of H_2O_2 after 21 h did not improve the yield but promoted a successive reaction to give several bifunctionalized pyridines with two THF molecules. This means that the products should be separated before the successive reaction takes place to obtain higher yield.

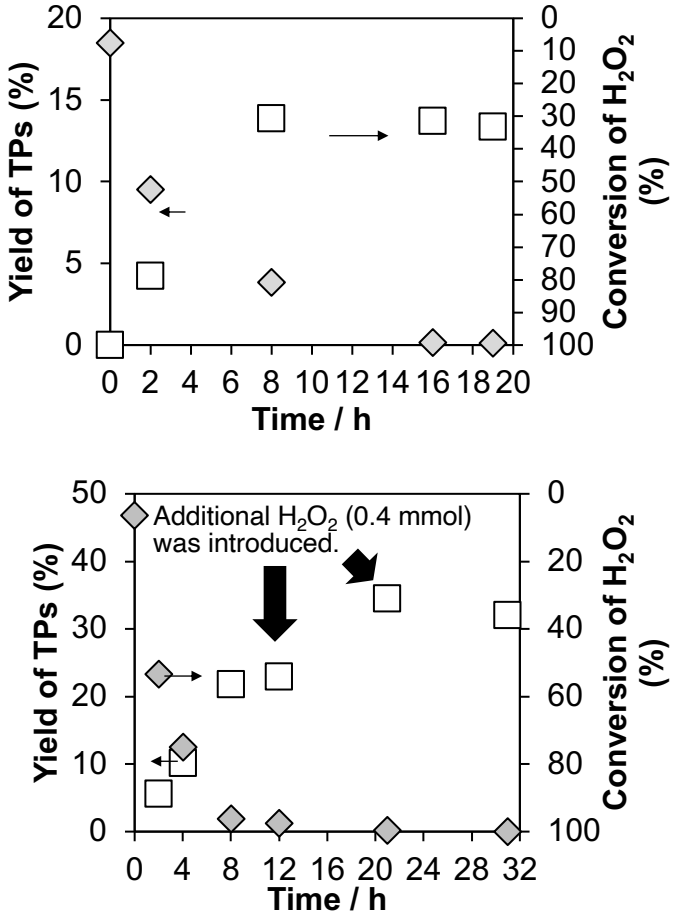

Fig. 2 Time course of the Minisci reaction between pyridine and THF using the pristine TiO_2 (A) or Pd/TiO_2 sample (B). Pyridine (0.4 mmol), THF (48 mmol), H_2O_2 (0.4 mmol), and TFA (0.4 mmol) were used. Irradiation wavelength was λ = 420±10 nm. The reaction tests were carried in a Pyrex glass tube (50 mL). In the reaction using Pd/TiO_2 (B), additional H_2O_2 (0.4 mmol) was introduced after 12 h and 21 h.

Under visible light, a ligand-to-metal-charge-transfer (LMCT) take places in the Ti-peroxo species to transfer an electron from its peroxo oxygen (O^-) to Ti(IV) cation, producing $O^{\bullet}$ (hole) and Ti(III) cation (electron) in the surface complex (Scheme 3).[23] The photoexcited electron would be further transferred to the conduction band of TiO_2 to react with the substrates. It is reported that visible-light excitation of surface Ti-peroxo species produces hydroxyl radical in H_2O_2-TiO_2 system through the reduction of a H_2O_2 molecule in liquid phase by the photoexcited electron (eq. 3).[25] Therefore, it is also possible that the photogenerated electron formed from the Ti-peroxo species through the LMCT excitation reduces another H_2O_2 molecule to produce a hydroxyl radical. This hydroxyl radical would be the major active species for the reactions under visible light. The hole ($O^{\bullet}$) would also activate the substrates or decompose the surface Ti-peroxo species. The higher selectivity under visible light than that under UV light suggests the presence of the decomposition path before the oxidation of the substrates to OTs.

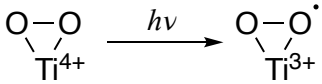

Scheme 3 Photoexcitation of side-on peroxo species.

Under UV light, TiO_2 is excited to generate photogenerated electrons and holes in the TiO_2, which can activate the substrates. The photogenerated electrons and holes would react with H_2O_2 and THF to produce radical species such as a hydroxyl radical ($^{\bullet}OH$), a hydroperoxyl radical ($^{\bullet}O_2H$), and a THF radical ($^{\bullet}C_4H_7O$) (eq. 3–5). Thus, under UV light conditions, these radical species would form some kinds of oxidation products (OTs) as the major by-products. Meanwhile, hole oxidation of pyridine would be difficult since pyridine molecules are in a cationic form. The hydroxyl radical would also produce a THF radical (eq. 6) while the hydroxyl radical and the hydroperoxyl radical accelerate the production of 2-hydroxytetrahydrofuran (eq. 7, 8), of which a subsequent oxidation gives other OTs species.

$$H_2O_2 + e^- \rightarrow {}^{\bullet}OH + OH^- \quad (3)$$

$$H_2O_2 + h^+ \rightarrow {}^{\bullet}O_2H + H^+ \quad (4)$$

$$C_4H_8O\ (THF) + h^+ \rightarrow {}^{\bullet}C_4H_7O + H^+ \quad (5)$$

$$C_4H_8O\ (THF) + {}^{\bullet}OH \rightarrow {}^{\bullet}C_4H_7O + H_2O \quad (6)$$

$${}^{\bullet}C_4H_7O + {}^{\bullet}OH \rightarrow C_4H_8O_2\ (OTs) \quad (7)$$

$${}^{\bullet}C_4H_7O + {}^{\bullet}O_2H \rightarrow C_4H_8O_2\ (OTs) + 1/2O_2 \quad (8)$$

When the reaction test was carried out in dark, OTs was initially produced with the consumption of H_2O_2 (Table 1, entry 9) but the amount of OTs did not increase with time (Table 1, entry 10). On the other hand, the amount of OTs and consumed H_2O_2 were larger in the absence of TFA in the dark (Table 1, entry 11) and they increased with time (Table 1, entry 12). This means that OTs can be produced upon a decomposition of H_2O_2, and TFA suppresses the decomposition. The OTs would be produced from a reaction between THF and $^{\bullet}OH$ adsorbed on the TiO_2 surface.[26] TFA would suppress the decomposition of H_2O_2 by poisoning the active sites for it on the TiO_2 surface. The suppression effect was also observed in the reaction under UV light (Table 1, entries 1 and 7) or visible light (Table 1, entries 3 and 8). Since TFA also promotes the production of TPs, two roles can be expected for TFA in the present system: protonation of pyridine for the Minisci reaction and suppression of thermal decomposition of H_2O_2.

Scavenging test

UV light irradiation induces band-to-band transition in TiO_2 (Fig. 3A) while visible light irradiation does the LMCT transition in the surface Ti-peroxo species (Fig. 3B). In both cases, photoexcited electron is generated in the conduction band of TiO_2 while hole is generated in the valence band of TiO_2 in the former case and on the surface peroxo species in the latter case. The presence of the photoexcited electrons in the conduction band of TiO_2 is necessary and enough to promote the aimed coupling reaction since they can activate hydrogen peroxide to start the reaction through the formation of hydroxyl radical and then THF radical, as mentioned above. The properties of the excited electron are common in both cases. Thus, the different selectivity under different wavelength-light would be due to the different property of the photogenerated hole.

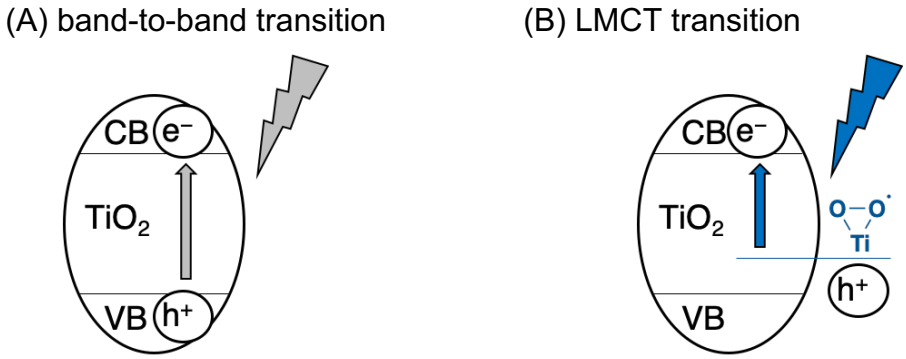

Fig. 3 Difference of the photogenerated hole between the band-to-band transition in TiO_2 (A) and the LMCT transition in the surface Ti-peroxo species (B).

If that is the case, the selectivity under UV light might be improved by suppressing hole oxidation of the substrates. Therefore, we carried out some reaction tests under UV light in the presence of methanol as a hole scavenger (Table 2, entries 2 and 3). As expected, the production of OTs was suppressed with increasing the amount of methanol, leading to higher selectivity such as 46 % with 16 mmol of methanol (Table 2, entry 3). H_2O_2 consumption was also suppressed by the addition of methanol. Although alcohols can also perform Minisci-coupling,[27,28] such kinds of products were not observed. Methanol can consume the hole efficiently and suppress the oxidation of the substrates sacrificially. The increase in the selectivity with the suppression of H_2O_2 consumption indicates that the oxidation of H_2O_2 (eq. 4) is responsible for the formation of by-products. In addition, the yield of TPs was not changed so much by the addition of methanol. It indicates that methanol consumed only holes on TiO_2 selectively and the photoexcited electrons were used for the TPs formation (eq. 3).

Table 2 Effect of a hole scavenger (MeOH) and a hydroxyl radical scavenger (2-PrOH) on the product yield and the amount of consumed H_2O_2 after reaction under UV light[a]

Entry	Scavenger / mmol		Products[b] / μmol		Consumed H_2O_2[c] / μmol	Selectivity[d] (%)	
			TPs	OTs		S_{py}	S_{THF}
1	-	-	1.8	6.9	63	>99	19
2	MeOH	8	1.7	4.7	57	>99	27
3	MeOH	16	1.9	2.2	7	>99	46
4	2-PrOH	8	1.2	11	67	>99	10

[a] Reaction conditions: pyridine (0.2 mmol), THF (24 mmol), 30 % H_2O_2 aq. (22.5 μL, 0.2 mmol of H_2O_2), TFA (0.2 mmol), and a scavenger with the TiO_2 photocatalyst (50 mg) were used, irradiation wavelength was 360 ± 10 nm, and reaction time was 1 h. The reaction tests were carried out in a Pyrex test tube (20 mL). [b,c,d] See the caption in Table 1.

Instead of methanol, the addition of 2-propanol was examined under UV light irradiation. 2-propanol is often used as a hydroxyl radical scavenger while in some cases it is regarded as a hole scavenger. As a result, the amount of obtained OTs increased from 6.9 to 11 (Table 2, entry 4), which is opposite to the case of methanol addition. It is clarified that 2-propanol cannot act as a hole scavenger in the present conditions although the reason for the increase was uncovered. On the other hand, the obtained TPs decreased from 1.8 to 1.2 μmol (Table 2, entry 4), meaning that 2-propanol reacted with a hydroxyl radical in this system in competition with THF. It also confirms that hydroxyl radical participates in the formation of TPs; hydroxyl radical would produce THF radical which attacks to a protonated pyridine. Therefore, it is suggested that the THF radical is generated mainly from the reaction of THF with hydroxyl radical (eq. 6), not with the photogenerated hole (eq. 5). This would be due to high reactivity of THF with hydroxyl radical. The rate constant for the reaction with hydroxyl radical in aqueous solution is higher for THF (4.0×10^9) than that of 2-propanol (1.9×10^9),[29]

which is a well-known hydroxyl radical scavenger and used in the present study. Therefore, THF would mainly react with hydroxyl radical before reacting with the photogenerated hole.

Scavenging tests were also carried out under visible light to get a further insight into the reaction mechanism (Table 3). The yield of TPs decreased with increasing the amount of 2-propanol (Table 3, entries 1–3) as with the case in the UV-light, confirming that hydroxyl radical activates THF to form TPs. The yield of TPs also decreased with increasing the amount of an electron scavenger, $AgNO_3$ aqueous solution (Table 3, entries 1 and 4–6) while the addition of the same amount of water did not decrease the yield of TPs (Table 3, entry 7). This means that the decrease in the yield of TPs by the addition of $AgNO_3$ aqueous solution is due to electron scavenging by Ag^+ cation. Thus, it is also confirmed that the hydroxyl radical is produced via reduction of H_2O_2 by the photogenerated electron and activates THF molecules under visible light.

Table 3 Effect of a hydroxyl radical scavenger (2-PrOH), an electron scavenger (Ag^+), and a hole scavenger (MeOH) on the product yield and the amount of consumed H_2O_2 after reaction under visible light[a]

Entry	Scavenger / mmol		Products[b] / μmol		Consumed	Selectivity[d] (%)	
			TPs	OTs	H_2O_2[c] / μmol	S_{py}	S_{THF}
1	-	-	6.9	10	82	>99	40
2	2-PrOH	4	4.7	11	75	>99	29
3	2-PrOH	8	3.2	9.1	74	>99	26
4[e]	$AgNO_3$	0.03	4.8	4.1	84	>99	54
5[e]	$AgNO_3$	0.1	1.6	4.6	86	>99	26
6[e]	$AgNO_3$	0.2	n.d.	5.8	78	0	0
7[f]	-	-	8.0	7.4	92	>99	52
8	MeOH	8	2.8	3.1	67	>99	48

[a] Reaction conditions: Irradiation wavelength was 420 ± 10 nm. Other conditions were the same with those described in Table 2. [b,c,d] See the caption in Table 1. [e] 0.15 M $AgNO_3$ aq. was used. [f] Same amount of water with entry 4 (0.2 mL) was added.

The addition of 0.03 mmol of $AgNO_3$ also decreased the OTs production from 10 to 4.1 μmol (Table 3, entries 1 and 4), suggesting that the photoexcited electron also produces OTs. However, it started to increase slightly by further increase of $AgNO_3$ (Table 3, entries 5 and 6) and 5.8 μmol of OTs was still observed at the addition of 0.2 mmol of $AgNO_3$ (Table 3, entry 6), which completely inhibited the production of TPs. Since OTs can be produced in dark (Table 1, entry 8), the OTs observed in these conditions would be produced by dark reactions between THF and H_2O_2 thermally catalyzed by TiO_2 or Ag metal species photodeposited on the TiO_2.

The reaction test under visible light was also carried out using the hole scavenger (Table 3, entry 8). If hole oxidation of H_2O_2 takes place under visible light, the addition of the hole scavenger would improve the selectivity as with the reaction under UV light. However,

the selectivity was hardly improved; the amounts of both TPs and OTs were decreased, which is different from the UV-light case. This different effect of the hole scavenger under visible light with that under UV light supports the conclusion in the reaction tests under the light of variously limited wavelength: hole oxidation of H_2O_2 takes place majorly under UV light while it seems less major under visible light. The decrease in the amounts of both products would be due to inhibition of the adsorption of H_2O_2 on TiO_2 by methanol.

Finally, reaction tests were carried out using quinoline instead of pyridine to investigate the generality of the present system (Table 4). Derivatives of quinoline are known as important molecules in the field of pharmacy. The reaction successfully proceeded to afford mainly two isomers of tetrahydrofuranylquinoline (TQs) in a ratio of 3 : 2. The selectivities to TQs under UV light were high such as >99% based on quinoline (S_{quino}) and 84% based on THF (S_{THF}) (λ = 360 ± 10 nm, Table 4, entry 1), suggesting that THF radicals are selectively used for the functionalization of quinoline even under UV light irradiation. Thus, the use of visible light to improve the selectivity was not so effective; S_{quino} and S_{THF} under visible light (λ = 400 ± 10 nm, Table 4, entry 2) were >99% and 87%, respectively. The yield in 2 h was 14 % under UV light and 20 % under visible light, which is much higher than that of the reaction with pyridine (Table 1, entries 1 and 2). Thus, it is noticed that the present reaction system using visible light has a certain limitation for available substrates.

Table 4 Results of reaction tests of quinoline and THF[a]

Entry	λ / nm	Products[b] / μmol		Yield of TQs[c] (%)	Selectivity[d] (%)	
		TQs	OTs		S_{quino}	S_{THF}
1	360	28	1.2	14	>99	84
2	400	39	1.4	20	>99	87

[a] Reaction conditions: quinoline (0.2 mmol), THF (24 mmol), 30 % H_2O_2 aq. (22.5 μL, 0.2 mmol of H_2O_2), and TFA (0.2 mmol) with the 0.1 wt% Pd-loaded TiO_2 photocatalyst were used, and the reaction time was 2 h. [b] TQs: total amount of tetrahydrofuranylquinoline. OTs: total amount of 2-hydroxytetrahydrofuran, γ-butyrolactone, and α-hydroxy-γ-butyrolactone. [c] Yield of TQs based on the introduced quinoline. [d] Selectivity to TQs. The selectivity based on pyridine was calculated as S_{quino} = [100 × TQs (μmol)]/[(TQs + byproducts from quinoline) (μmol)]; the selectivity based on THF was calculated as S_{THF} = [100 × TPs (μmol)]/[(TPs + OTs) (μmol).

Reaction mechanism

Based on all of the results discussed above, a tentative reaction mechanism is proposed as follows. Under UV light (Fig. 4A), TiO_2 is excited to generate photoexcited electron and hole in the conduction and valence bands, respectively. The electron and hole migrate the surface to react with the substrates. The former reduces hydrogen peroxide to produce hydroxyl

radical (eq. 3) while the latter oxidizes hydrogen peroxide into radical species such as hydroperoxo radical (eq. 4). The hydroxyl radical subtracts a hydrogen atom from THF molecule to produce THF radical (eq. 5) and this radical attacks to pyridinium ion protonated by TFA. Removal of a hydrogen atom from the transition state gives TPs. The hydroperoxo radical produces OTs by reacting with THF (eq. 6).

Under visible light (Fig. 4B), the surface Ti-peroxo species absorbs the light via LMCT excitation from the peroxy oxygen atom to the Ti atom. The electron on the Ti atom is further transferred to the conduction band of TiO_2 and reduces hydrogen peroxide into hydroxyl radical, which produces THF radical and finally TPs. This reaction in TPs formation is the same as with the UV-light case. The hole, on the other hand, is generated on the peroxy oxygen. This positively-charged peroxy oxygen would decompose although it also oxidizes the substrates. The presence of the decomposition path suppresses the oxidation of H_2O_2 and thus the formation of OTs, leading to higher TPs selectivity (S_{THF}).

In both cases, TFA promotes the production of TPs and suppresses the thermal decomposition of H_2O_2.

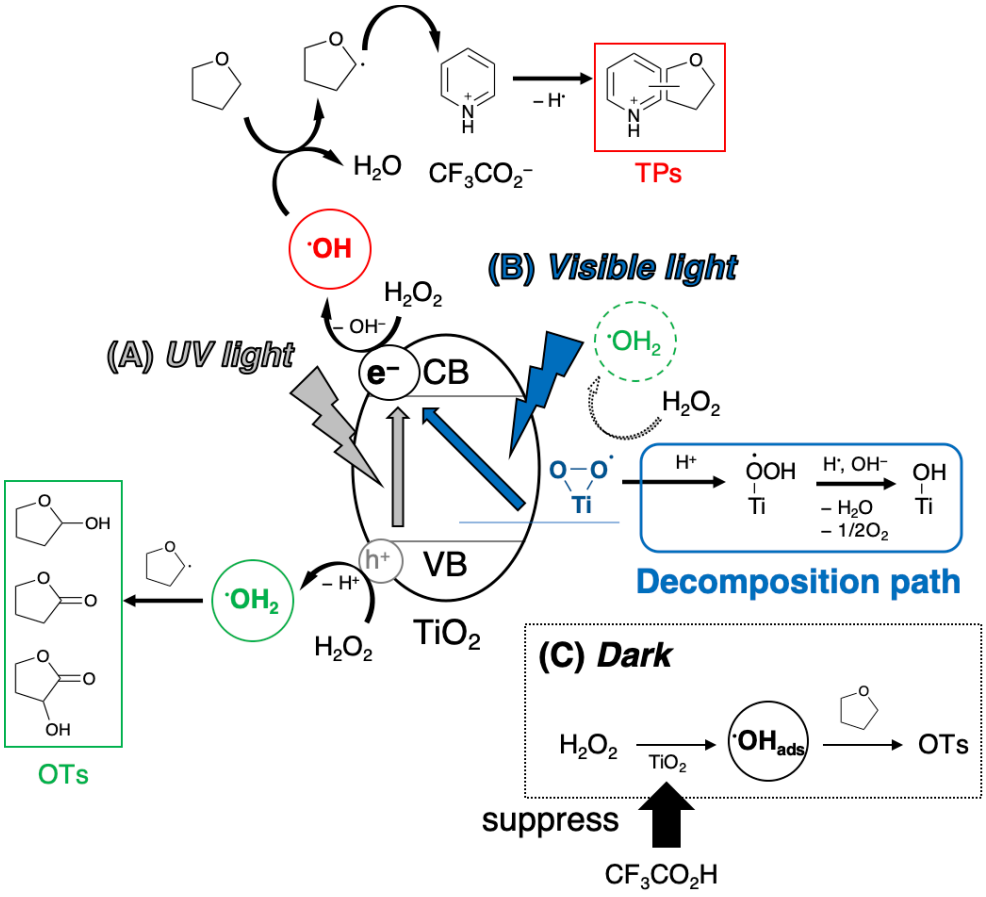

Fig. 4 Schematic illustration of the reaction mechanism under UV light (A), visible light (B), and in dark (C).

Conclusion

The use of the LMCT excitation of surface Ti-peroxo species can be used for the selective Minisci-type functionalization of pyridine. Both H_2O_2 and TFA are necessary to promote this reaction. The Ti-peroxo species decompose after photoexcitation, and this vulnerability of the photogenerated hole suppresses the oxidation of H_2O_2, leading to higher selectivity.

The yield in the present system is not satisfactory and thus a further study is required to improve the yield by some methods such as continuous addition of H_2O_2 with separation of the products from the system. Nevertheless, this study provided a unique way to improve the selectivity of photocatalysis involving ROS generation. We anticipate the present study to trigger studies to expand the application of aerobic photocatalysis as an efficient and selective organic reaction system.

References

1. Nakata, K. & Fujishima, A. TiO_2 photocatalysis: Design and applications. *J. Photochem. Photobiol. C Photochem. Rev.* **13**, 169–189 (2012).
2. Schneider, J. *et al.* Understanding TiO_2 photocatalysis: Mechanisms and materials. *Chem. Rev.* **114**, 9919–9986 (2014).
3. Hirakawa, T. & Nosaka, Y. Properties of $O_2^{\bullet-}$ and $OH^{\bullet}$ Formed in TiO_2 aqueous suspensions by photocatalytic reaction and the influence of H_2O_2 and some ions. *Langmuir* **18**, 3247–3254 (2002).
4. Hirakawa, T., Yawata, K. & Nosaka, Y. Photocatalytic reactivity for $O_2^{\bullet-}$ and $OH^{\bullet}$ radical formation in anatase and rutile TiO_2 suspension as the effect of H_2O_2 addition. *Appl. Catal. A Gen.* **325**, 105–111 (2007).
5. Cho, M., Chung, H., Choi, W. & Yoon, J. Linear correlation between inactivation of E. coli and OH radical concentration in TiO_2 photocatalytic disinfection. *Water Res.* **38**, 1069–1077 (2004).
6. Rivera, A. P., Tanaka, K. & Hisanaga, T. Photocatalytic degradation of pollutant over TiO_2 in different crystal structures. *Appl. Catal. B, Environ.* **3**, 37–44 (1993).
7. Caronna, T. *et al.* Sunlight-induced functionalisation reactions of heteroaromatic bases with aldehydes in the presence of TiO_2: A hypothesis on the mechanism. *J. Photochem. Photobiol. A Chem.* **189**, 322–328 (2007).
8. Caronna, T., Gambarotti, C., Palmisano, L., Punta, C. & Recupero, F. Sunlight-induced reactions of some heterocyclic bases with ethers in the presence of TiO_2. A green route for the synthesis of heterocyclic aldehydes. *J. Photochem. Photobiol. A Chem.* **171**, 237–242 (2005).

9. Zhang, G., Kim, G. & Choi, W. Visible light driven photocatalysis mediated via ligand-to-metal charge transfer ({LMCT}): an alternative approach to solar activation of titania. *Energy Environ. Sci.* **7**, 954–966 (2014).
10. Higashimoto, S. *et al.* Selective photocatalytic oxidation of benzyl alcohol and its derivatives into corresponding aldehydes by molecular oxygen on titanium dioxide under visible light irradiation. *J. Catal.* **266**, 279–285 (2009).
11. Higashimoto, S. *et al.* Selective Photocatalytic Oxidation of Benzyl Amine By O_2 Into N-Benzylidenebenzylamine on TiO_2 Using Visible Light. *Curr. Org. Chem.* **17**, 2374–2381 (2013).
12. Lang, X. *et al.* Visible-light-induced selective photocatalytic aerobic oxidation of amines into imines on TiO_2. *Chem. - A Eur. J.* **18**, 2624–2631 (2012).
13. Lang, X. *et al.* Tertiary amine mediated aerobic oxidation of sulfides into sulfoxides by visible-light photoredox catalysis on TiO_2. *Chem. Sci.* **6**, 5000–5005 (2015).
14. Yamamoto, A., Ohara, T. & Yoshida, H. Visible-light-induced photocatalytic benzene/cyclohexane cross-coupling utilizing a ligand-to-metal charge transfer benzene complex adsorbed on titanium oxides. *Catal. Sci. Technol.* **8**, 2046–2050 (2018).
15. Naniwa, S., Tyagi, A., Yamamoto, A. & Yoshida, H. Visible-light photoexcitation of pyridine surface complex, leading to selective dehydrogenative cross-coupling with cyclohexane. *Phys. Chem. Chem. Phys.* **20**, 28375–28381 (2018).
16. Tyagi, A., Matsumoto, T., Kato, T. & Yoshida, H. Direct C–H bond activation of ethers and successive C–C bond formation with benzene by a bifunctional palladium-titania photocatalyst. *Catal. Sci. Technol.* **6**, 4577–4583 (2016).
17. Yoshida, H., Fujimura, Y., Yuzawa, H., Kumagai, J. & Yoshida, T. A heterogeneous palladium catalyst hybridised with a titanium dioxide photocatalyst for direct C-C bond formation between an aromatic ring and acetonitrile. *Chem. Commun.* **49**, 3793–3795 (2013).
18. Wada, E. *et al.* Direct cyanomethylation of aliphatic and aromatic hydrocarbons with acetonitrile over a metal loaded titanium oxide photocatalyst. *Catal. Sci. Technol.* **7**, 2457–2466 (2017).
19. Boonstra, A. H. & Mutsaers, C. A. H. A. Adsorption of hydrogen peroxide on the surface of titanium dioxide. *J. Phys. Chem.* **79**, 1940–1943 (1975).
20. Nakamura, R. & Nakato, Y. Primary Intermediates of Oxygen Photoevolution Reaction on TiO_2 (Rutile) Particles, Revealed by in Situ FTIR Absorption and Photoluminescence Measurements. *J. Am. Chem. Soc.* **126**, 1290–1298 (2004).
21. Ohno, T., Masaki, Y., Hirayama, S. & Matsumura, M. TiO_2-Photocatalyzed Epoxidation of 1-Decene by H_2O_2 under Visible Light. *J. Catal.* **204**, 163–168 (2001).
22. Shiraishi, Y. *et al.* Selective hydrogen peroxide formation by titanium dioxide photocatalysis with benzylic alcohols and molecular oxygen in water. *ACS Catal.* **3**,

2222–2227 (2013).

23. Bonino, F. *et al.* Ti-Peroxo Species in the TS-1/H_2O_2/H_2O System. *J. Phys. Chem. B* **108**, 3573–3583 (2004).
24. Bordiga, S. *et al.* The structure of the peroxo species in the TS-1 catalyst as investigated by Resonant Raman spectroscopy. *Angew. Chemie - Int. Ed.* **41**, 4734–4737 (2002).
25. Li, X., Chen, C. & Zhao, J. Mechanism of photodecomposition of H_2O_2 on TiO_2 surfaces under visible light irradiation. *J. Am. Chem. Soc.* **17**, 4118–4122 (2001).
26. Lousada, C. M., Johansson, A. J., Brinck, T. & Jonsson, M. Mechanism of H_2O_2 decomposition on transition metal oxide surfaces. *J. Phys. Chem. C* **116**, 9533–9543 (2012).
27. Jin, J. & MacMillan, D. W. C. Alcohols as alkylating agents in heteroarene C-H functionalization. *Nature* **525**, 87–90 (2015).
28. Vijeta, A. & Reisner, E. Carbon nitride as a heterogeneous visible-light photocatalyst for the Minisci reaction and coupling to H_2 production. *Chem. Commun.* **55**, 14007–14010 (2019).
29. Buxton, G. V., Greenstock, C. L., Helman, W. P. & Ross, A. B. Critical Review of rate constants for reactions of hydrated electrons, hydrogen atoms and hydroxyl radicals ($^{\cdot}OH/^{\cdot}O^-$ in Aqueous Solution. *J. Phys. Chem. Ref. Data* **17**, 513–886 (1988).

Chapter 3

Ligand-to-metal charge transfer of pyridine surface complex on TiO_2 for selective dehydrogenative cross-coupling with benzene

Abstract

Dehydrogenative cross-coupling (DCC) between pyridine and benzene proceeded selectively using TiO_2 photocatalyst under visible light irradiation at optimized concentrations of the substrates. Visible light induces ligand-to-metal charge transfer (LMCT) between pyridine and TiO_2 surface to give pyridine radical cation, which produces pyridyl radical by its deprotonation or oxidation of another pyridine molecule. The pyridyl radical attacks a benzene ring to form an $sp^2C–sp^2C$ bond and a hydrogen atom is subsequently removed to complete DCC. Selective excitation of the pyridine LMCT complex in the presence of an excess amount of benzene would be the key for higher selectivity.

Introduction

Photocatalytic organic transformation is a promising reaction system which can achieve unique and highly difficult reaction such as dehydrogenative cross-coupling (DCC) under ambient conditions. DCC is one of the most environmental-friendly and thus important reaction in organic synthesis.[1,2] Many DCC systems have been reported both in homogeneous and heterogeneous catalysis, usually utilizing heat or light as a driving force.[3–7] The reaction often proceeds in oxidative manner by using external oxidant such as molecular oxygen, in which the byproduct is water.[8] In semiconductor photocatalysis, however, DCC can be achieved in dehydrogenative manner under ambient pressure and temperture,[9–12] where the byproduct is hydrogen gas, which is a promising energy carrier.[13] Therefore, photocatalytic DCC by semiconductor material has a great potential and should be explored.

Photocatalytic DCC typically proceeds through a reaction between radical species generated by hole oxidation of organic molecules. Especially over TiO_2, one of the most practical photocatalysts with enough oxidation power to oxidize various molecules,[14–18] the reaction often proceeds through a radical-radical coupling mechanism,[11,12,19] which also allows undesired reactions such as homo-coupling. To improve the selectivity of DCC by TiO_2 photocatalysis, unselective oxidation of the substrate should be avoided. One of the ways to suppress unselective oxidation in TiO_2 photocatalysis is to utilize ligand-to-metal charge transfer (LMCT) between TiO_2 surface and adsorbed molecules.[20,21] In this system, photogenerated hole generates on the adsorbed molecule. Since the oxidative potential of this hole is less positive than that of excited TiO_2 photocatalyst, undesired oxidation tends to be limited, allowing selective oxidation of the substrate. Although few studies were available on the utilization of the LMCT system to DCC, we have recently reported selective DCC between benzene or pyridine and cyclohexane through LMCT between TiO_2 and the aromatics.[22,23] In our systems, an aromatic radical cation generated by the LMCT of aromatic-TiO_2 surface complex oxidizes cyclohexane into cyclohexyl radical. The radical attacks an aromatic molecule to complete DCC between sp^2C–sp^3C through a radical addition and elimination mechanism. Formation of such surface complexes on TiO_2 surface has been reported with various molecules like as alcohols,[24,25] amines,[26,27] sulfides,[28] and aromatics.[22,23,29,30] Therefore, in order to extend the application of the LMCT-based system, we need to investigate how the system performs and whether the selectivity can

be improved even in the presence of multiple adsorbates for surface complexation. Moreover, the scope of the previous systems was limited to cross-coupling between sp^2C–sp^3C. Cross-coupling between sp^2C– sp^2C such as the formation of arene–arene linkage is also important in organic synthesis because of a large number of important compounds containing the linkage in pharmaceutical, agrochemical, and natural product chemistry.[31] In the present study, we report a new LMCT-based DCC between sp^2C–sp^2C in the presence of two adsorbates for surface complexation: pyridine and benzene. We found that selective DCC between these molecules can be achieved through an LMCT excitation of the pyridine surface complex at optimized concentrations of the substrates in which an excess amount of benzene exists.

Experimental section

Catalyst preparation

Various TiO_2 powder samples were employed, which were donated by the Catalysis Society of Japan and denoted as JRC-TIO-2 (anatase phase, 18 $m^2\ g^{-1}$), JRC-TIO-6 (rutile phase, 100 $m^2\ g^{-1}$), JRC-TIO-7 (anatase phase, 279 $m^2\ g^{-1}$), JRC-TIO-9 (anatase phase, 290–310 $m^2\ g^{-1}$), JRC-TIO-12 (anatase phase, 290 $m^2\ g^{-1}$), JRC-TIO-13 (anatase phase, 59 $m^2\ g^{-1}$), and JRC-TIO-14 (anatase phase, 338 $m^2\ g^{-1}$). All metal-loaded TiO_2 catalysts were prepared by a photodeposition method using TiO_2 powder and an aqueous methanolic solution of an appropriate metal precursor such as $PdCl_2$ (Kishida, 99%) or $H_2PtCl_6{\cdot}6H_2O$ (Wako, 99.9%) as follows. TiO_2 powder (4.0 g) was dispersed in ion-exchanged water (300 mL) and irradiated using a ceramic xenon lamp (PE300BUV) for 30 min. Then, methanol (100 mL) and the desired amount of the metal precursor solution were added to the suspension, and the contents were magnetically stirred for 15 min without irradiation, followed by stirring under light for 1 h. The amount of the metal precursor solution was determined so as to fix the metal loading amount to 0.1 wt%. The product was then filtered by suction, washed with ion-exchanged water, and dried at 323 K for 12 h to obtain metal-loaded TiO_2 photocatalysts. The catalysts were referred to as M/TiO_2, where M represents Pd or Pt.

Reaction tests

All of the chemicals were of analytical grade and were used without further purification. Before

a photocatalytic reaction test, the M/TiO_2 sample (0.1 g) in a Pyrex glass tube (20 mL) was subjected to pre-treatment for 30 min under the xenon lamp light so as to clean its surface. Then, the reactants were added into the test tube, followed by 10 minutes of Ar bubbling, and stirring under light for the desired reaction time at room temperature. The light intensity was 160 mW cm^{-2} measured at 415 ± 55 nm in wavelength. After irradiation, 0.5 mL of the gaseous phase was collected by an air-tight syringe and was analyzed by a GC-TCD (Shimadzu, GC-8A). The reaction mixture was sampled by a syringe with a PTFE filter to separate the M/TiO_2 sample, and then analyzed by a GC-MS (Shimadzu, GCMS-QP5050A). The amounts of products were determined from the GC-MS calibration curve of the authentic samples procured from the industries.

Diffuse reflectance UV-vis spectroscopy

The UV-vis spectra of the powder samples were recorded in a diffuse-reflectance mode. A Pd/TiO_2 sample was diluted with $BaSO_4$ by a factor of 100. For samples with an adsorbate, 50 mL of pyridine or benzene was added to 0.15 g of the diluted sample, followed by stirring for 30 min. Then, the desired amount of the sample (typically 0.13 g) was placed in a cell to fix the amount of the Pd/TiO_2 in the sample, and the spectrum was recorded using a UV-vis spectrophotometer (Jasco V-570) equipped with an integrating sphere, where $BaSO_4$ was used as a reference.

Results and discussion

Photocatalytic reaction tests

A Pd/TiO_2 sample was examined for the reaction tests under photoirradiation with light of various limited wavelength ranges (Table 1, entries 1–3). Several products were obtained such as 2-phenylpyridine (2-PhP), 3-phenylpyridine (3-PhP), and 4-phenylpyridine (4-PhP) as the DCC products (PhPs) as well as homo-coupled products formed from pyridine (bipyridyls (BPs): 2,2'-BP, 2,3'-BP, and 2,4'-BP) and benzene (biphenyl: BPh). The regioselectivity for the three PhPs was almost identical in most cases regardless of the irradiation wavelength, *i.e.*, about 90% of 2-PhP, 4% of 3-PhP, and 6% of 4-PhP were formed. This is consistent with the C–H bond dissociation energy (BDE) of pyridine (439.3 kJ mol^{-1} for site 2 and 468.6 kJ mol^{-1} for sites 3 and 4).

Trimers from two pyridine molecules and one benzene molecule or one pyridine and two benzene molecules were not observed. The formation of BPh indicates that benzene was also activated during the reaction. Thus, a certain amount of polymers could be formed although they cannot be detected by GC. The reaction did not proceed in the dark or in the absence of the photocatalyst, which confirmed the reaction proceeds photocatalytically. Concomitant hydrogen production also confirmed the reaction took place dehydrogenatively.

Under photoirradiation of both UV and visible light (λ > 350 nm, Table 1, entry 1), PhPs, BPs and BPh were obtained unselectively, where the selectivities to PhPs were calculated as 44% and 42% based on the products formed from pyridine (S_{Py}) and benzene (S_{Be}), respectively. The unselective products formation suggests that both pyridyl ($^{\bullet}C_5H_4N$) and phenyl ($^{\bullet}C_6H_5$) radicals were formed by the photocatalytic oxidation of the reactants by holes generated on the UV-light-activated TiO_2 photocatalyst, followed by successive radical-radical coupling.

Table 1 Results of reaction tests performed under photoirradiation with light of various limited wavelength ranges[a]

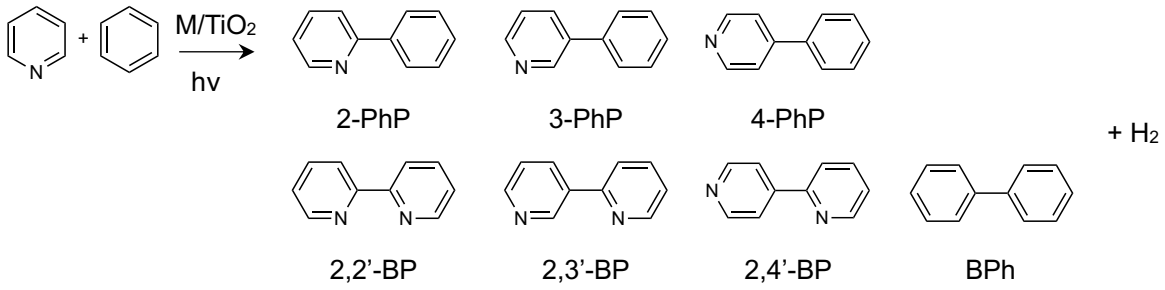

Entry	λ / nm	Time / h	Metal	Products[b] / μmol			Yield of PhPs[c] (%)	Selectivity to PhPs[d] (%)	
				PhPs	BPs	BPh	Y_{Py}	S_{Py}	S_{Be}
1	> 350	0.2	Pd	1.7	0.99	1.2	0.14	44	42
2	> 400	0.5	Pd	1.6	0.17	0.32	0.13	84	73
3	> 422	6	Pd	1.7	trace	0.09	0.14	>99	90
4	> 400	2	Pd	5.2	0.49	0.96	0.43	84	73
5	> 400	2	Pt	6.1	1.1	1.1	0.51	73	73
6	> 400	2	-	1.6	0.14	0.12	0.13	85	87

[a] Reaction conditions: pyridine (0.10 mL, 1.2 mmol) and benzene (1.9 mL, 21 mmol) were used with a M/TiO_2 photocatalyst (JRC-TIO-14, 0.1 g), and the light intensity was 160 mW cm^{-2} measured at a wavelength of 415 ± 55 nm. [b] PhPs: total amount of 2-PhP, 3-PhP, and 4-PhP. BPs: total amount of 2,2'-BP, 2,3'-BP, and 2,4'-BP. [c] Yield of PhPs based on the introduced pyridine. [d] Selectivity of DCC. The selectivity based on pyridine was calculated as S_{Py} = [100 × PhPs (mmol)]/[(PhPs + 2 × BPs) (mmol)]; the selectivity based on benzene was calculated as S_{Be} = [100 × PhPs (mmol)]/[(PhPs + 2 × BPh) (mmol)].

Under visible light (λ > 400 nm, Table 1, entry 2), in contrast, PhPs as cross-coupling products were successfully obtained as main products, which led to a higher selectivity (S_{Py} = 84% and S_{Be} = 73%) than that under irradiation including UV light, although the production rates were lower due to the limited photon number for the limitation of wavelength range. The selectivity was further improved under more-limited-wavelength light (λ > 422 nm, Table 1, entry 3) such as >99 % for S_{Py} and 90 % for S_{Be}. This result indicates a different reaction mechanism under visible light from that in the presence of UV light.

The effect of metal co-catalyst was also investigated (Table 1, entries 4 and 5). Generally, it is considered that metal co-catalyst on photocatalysts can suppress the recombination of photogenerated electrons and holes to enhance the photocatalytic activity.[32–34] Both Pd and Pt loaded samples showed higher activity than a pristine TiO_2 sample (Table 1, entry 6), which suggests that these metals actually work as a charge separator. At the same time, metal deposition decreased the selectivity. The Pd/TiO_2 sample showed higher S_{py} (Table 1, entry 4) than the Pt metal loaded sample (Table 1, entry 5). We have previously reported that Pd cocatalyst on TiO_2 can act as a catalyst which promote the radical addition to benzene in some cross-coupling reactions.[9,10,12,22] Thus, the higher selectivity of the Pd-loaded sample in the present system would be also contributed from the presence of Pd metal catalysis.

The reaction tests were also carried out with various pristine TiO_2 samples under visible light irradiation (λ > 400 nm). The results are shown in Table 2. The yield of PhPs increased with increasing the surface area of TiO_2 (Table 2, entries 1–6) and JRC-TIO-14 (Table 2, entry 6), which has the largest surface area, gave the largest amount of PhPs. A rutile sample showed comparable activity to JRC-TIO-14 (Table 2, entry 7). We employed JRC-TIO-14 as the TiO_2 photocatalyst in the following experiments. The larger specific surface area would be favorable to the surface complex formation.

Table 2 Results of the reaction tests under photoirradiation with various pristine TiO_2 photocatalysts[a]

Entry	TiO_2	Crystal phase	Specific surface area / $m^2\ g^{-1}$	Products / μmol [b]			Selectivity to PhPs (%) [d]	
				PhPs	BPs	BPh	S_{Py}	S_{Be}
1	TIO-2	Anatase	18	n.d.[c]	n.d.[c]	n.d.[c]	-	-
2	TIO-13	Anatase	59	0.25	n.d.[c]	0.09	>99	59
3	TIO-7	Anatase	279	0.48	0.05	0.04	83	86
4	TIO-12	Anatase	290	0.58	0.03	0.08	88	78
5	TIO-9	Anatase	290–310	0.56	0.03	0.05	92	85
6	TIO-14	Anatase	338	1.6	0.14	0.12	85	88
7	TIO-6	Rutile	100	1.4	0.14	0.11	83	86

[a] Reaction conditions: the reaction time was 2 h, the irradiation wavelength was $\lambda > 400$ nm, and other conditions were same with those described in Table 1. [b,d] See the caption of Table 1. [c] Not detected.

Next, we investigated the effect of concentration of the reactants on the reaction under visible light (Table 3). We carried out reaction tests with a fixed volume of the reaction solution (2.0 mL) but with different ratio of pyridine and benzene. Compared to the ratio used above (Table 3, entry 1), an increase of the ratio of pyridine to benzene decreased S_{Py} but increased S_{Be} (Table 3, entries 2–5) and a decrease of the ratio increased S_{Py} but decreased S_{Be} (Table 3, entries 6 and 7). These results were plotted in Fig. 1. Low concentration of pyridine is necessary to achieve the selective cross-coupling with high S_{Py} under visible light. The ratio of 0.05 with 1.2 mmol of pyridine and 21 mmol of benzene provided moderately high values in both selectivities, S_{Py} and S_{Be}, which was thus employed as standard conditions in the present study. This means that selective DCC can be achieved even in the presence of two adsorbates for surface complexation by optimizing their concentration. When a long-time reaction test was carried out under the optimized conditions, higher selectivities were maintained after 12 h and the yield reached 1.0 % (Fig. 2). Any successive reaction products such as trimers were still not observed. We also calculated the apparent quantum efficiency (AQE) based on the following equation: AQE (%) = 100 × (Amount of PhPs) / (Number of incident photons irradiated to the reactor). The AQE at 400 nm was 0.22 %.

Table 3 Results of the reaction tests with various concentration of pyridine and benzene under visible light[a]

Entry	Substrate / mmol		Ratio of pyridine to benzene	Products[b] / μmol			Selectivity[c] (%)	
	Pyridine	Benzene		PhPs	BPs	BPh	S_{Py}	S_{Be}
1[d]	1.2	21	0.050	5.2	0.49	0.96	84	73
2	6.0	18	0.25	4.5	2.8	0.35	45	87
3	12	12	0.50	3.1	5.7	0.11	22	93
4	18	6.0	0.75	1.5	8.9	trace	10	>99
5	24	0.50	0.98	0.10	9.7	trace	0.50	>99
6	0.48	24	0.020	3.4	0.23	0.98	88	63
7	0.24	24	0.010	1.9	trace	0.99	>99	49

[a] Reaction conditions: pyridine and benzene were used with a Pd/TiO_2 photocatalyst (JRC-TIO-14, 0.1 g), the reaction time was 2 h, the irradiation wavelength was $\lambda > 400$ nm, and the light intensity was 160 mW cm^{-2} measured at a wavelength of 415 ± 55 nm. [b,c] See the caption of Table 1. [d] This data was the same as that in Table 1 entry 4.

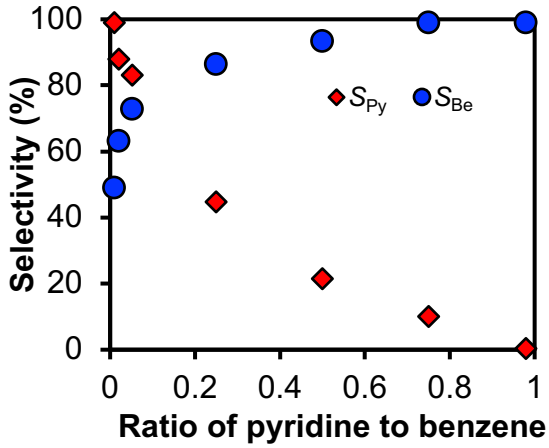

Fig. 1 Selectivities based on pyridine (S_{py}) or benzene (S_{Be}) in the reaction tests with various ratio of pyridine to benzene in visible light. Data were from Table 2.

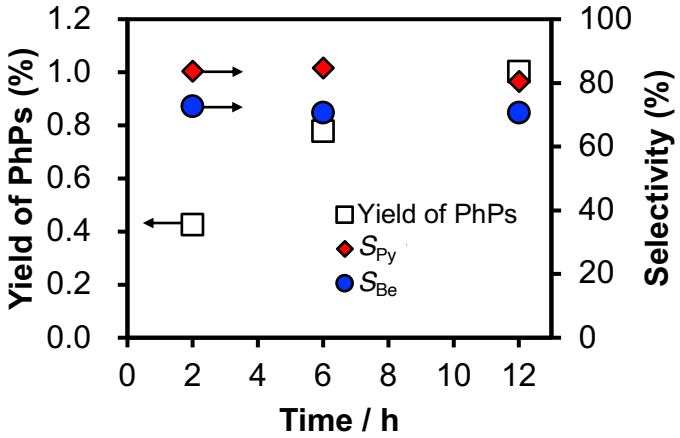

Fig. 2 Time course of the cross-coupling reaction between pyridine and benzene. Pyridine (0.1 mL, 1.2 mmol) and cyclohexane (1.9 mL, 21 mmol) with the Pd/TiO_2 photocatalyst (0.1 g) were used. The irradiation wavelength was $\lambda > 400$ nm. See the caption of Table 1 for the definitions of the selectivity of DCC, S_{Py} and S_{Be}.

The bare TiO_2 promoted the DCC reaction (Table 1, entry 6), and TiO_2 photocatalyst and these molecules, pyridine and benzene, do not absorb visible light when they have no interactions. These facts propose that other visible-light responsive species must be generated in this system. According to our previous reports, both pyridine[23] and benzene[22] can form surface complex with TiO_2 and absorb visible light ($\lambda > 400$ nm) to be excited; the former forms through an acid-base interaction and the latter does through a π interaction with the surface. Thus, many reaction routes are possibly speculated. Since both homo-coupling products (BPs and BPh) were produced, both pyridine and benzene should be activated in the present conditions. Further, to confirm which is the major active surface complex to produce PhPs under visible light conditions, we carried out the following experiments.

We first measured DR UV-vis spectra of pyridine or benzene adsorbed on a Pd/TiO_2 sample (Fig. 3). The Pd/TiO_2 sample was diluted with $BaSO_4$ for accurate measurement. The Pd/TiO_2 sample without adsorption of the reactants showed no photoabsorption beyond 400 nm in wavelength (Fig. 3A(a) and Fig. 3B(a)). The sample of pyridine adsorbed on the Pd/TiO_2 exhibited a large absorption band in the UV region (Fig. 3A(b)), and the additional absorption band of low intensity appeared beyond 400 nm (Fig. 3B(b)). The band which centers around 260 nm is attributed to pyridine molecules adsorbed physically or in the liquid phase and that centers around 300 nm and extends beyond 400 nm is LMCT excitation of the surface complex of adsorbed pyridine and the TiO_2 surface.[23] On the other hand, the sample adsorbing benzene (Fig. 3A(c)) showed a slightly larger absorption band compared with the Pd/TiO_2 (Fig. 3A(a)) but much lower than the sample adsorbing pyridine (Fig. 3A(b)), indicating a weaker interaction of benzene with TiO_2 than that of pyridine.

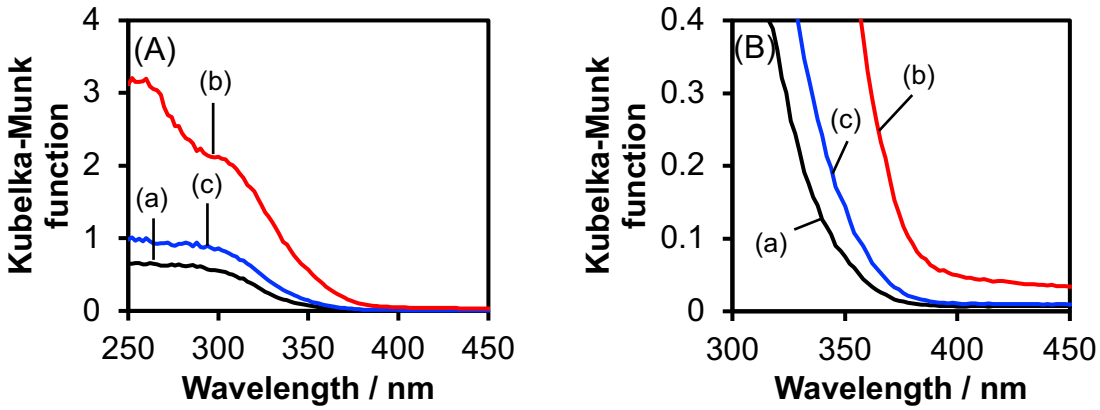

Fig. 3 (A) DR UV-vis spectra of (a) the Pd/TiO_2 sample (JRC-TIO-14) diluted with $BaSO_4$, (b) pyridine adsorbed on the diluted Pd/TiO_2 sample, (c) benzene adsorbed on the diluted Pd/TiO_2 sample. (B) Enlarged view of Fig. 3A.

Next, we carried out adsorption tests to compare the abilities of pyridine and benzene to form surface complex with TiO_2 (Table 4). Hexane was used as a solvent. When 24 μmol of pyridine was introduced, more than half of the introduced pyridine adsorbed on TiO_2 (Table 4, entry 1). When 27 μmol of benzene was introduced, only 2.0 μmol of benzene adsorbed (Table 4, entry 2). These results confirmed that pyridine is adsorbed on TiO_2 more preferentially than benzene, which could be due to the stronger interaction of pyridine with the surface.

Table 4 Results of adsorption tests[a]

Entry	Initial / μmol		After / μmol		Adsorbed[b] / μmol	
	Pyridine	Benzene	Pyridine	Benzene	Pyridine	Benzene
1	24	0	11	0	13	-
2	0	27	0	25	-	2.0

[a] Conditions: hexane was used as a solvent. The solution (2.0 mL, 12 μM pyridine or 14 μM benzene) was mixed with a TiO_2 photocatalyst (JRC-TIO-14, 50 mg), and then stirred for 1 h without photoirradiation. [b] Adsorbed amount was calculated as: (Initial (μmol)) − (After (μmol)).

We also carried out reaction tests with neat substrates under photoirradiation (Table 6). In the light including UV light, both reaction tests gave homo-coupling products, and the ratio of BPs to BPh was 2.2 (Table 5, entries 1 and 2), meaning that photoexcited TiO_2 photocatalyst promote the homocoupling reaction of pyridine with two times higher rate. In visible light, the amount of the homo-coupling products was much larger with pyridine (Table 5, entry 1) than with benzene (Table 5, entry 2) and the ratio of BPs to BPh was 11 (Table 5, entries 3 and 4). When we consider the photoinduced DCC proceeds through adsorption, photoexcitation, and reaction of the radical species with other radical or molecule, the large difference in the ratio of BPs to BPh in the homo-coupling reaction tests under the two photoirradiation conditions would be determined by the difference of photoexcitation process in these light conditions since adsorption and the reaction would be in common. These results suggest that pyridine can form the surface complex more easily and produce the homo-coupling product under visible-light irradiation in the presence of TiO_2 than benzene. Therefore, it is suggested that the major visible-light-excited species in the mixture of pyridine and benzene would be the pyridine-TiO_2 surface complex. As discussed previously,[23] pyridine adsorbs on the TiO_2 surface through an acid-base interaction between N atom in the pyridine ring and Ti cation on the surface. At the LMCT, lone pair electron on the N atom would be excited to localized 3d orbital on the Ti cation, and the excited state should be pyridine radical cation ($C_5H_5N^{\bullet+}$) adsorbed on the surface. The visible-light induced reaction will start with the generation of this surface radical cation species.

Table 5 Results of the photocatalytic reaction tests with neat pyridine or benzene under different wavelength light[a]

Entry	λ / nm	Substrate	Products[b] / μmol		Ratio of BPs to BPh
			BPs	BPh	
1	> 350	Pyridine	57	n.d.	2.2
2		Benzene	n.d.	26	
3	> 400	Pyridine	19	n.d.	11
4		Benzene	n.d.	1.7	

[a] Reaction conditions: pyridine or benzene (24 mmol) was used with a Pd/TiO_2 photocatalyst (0.1 g), the reaction time was 2h, and the light intensity was 120 mW cm^{-2} measured at a wavelength of 395 ± 35 nm. [b] See the caption in Table 1.

Isotope experiments

To get an insight into the reaction mechanism under each wavelength light, we carried out isotope experiments (Table 6). In the presence of UV light, the yields of PhPs in the reaction with pyridine-d_5 (Table 6, entry 2) were smaller than those in the reaction with normal reagents (Table 6, entry 1). The k_H/k_D value was greater than unity such as 1.9, which is recognized as kinetic isotope effect (KIE). This means that the rate-determining step (RDS) in the formation of PhPs is the C–H bond cleavage in pyridine under irradiation including UV light. This indicates that the C–H bond cleavage by the photogenerated hole takes place mainly in pyridine for the formation of PhPs, which gives a pyridyl radical ($C_5H_4N^{\bullet}$). A step of radical formation of benzene should not be included in the major reaction of the pyridine radical since the C–H bond cleavage is more difficult in benzene than in pyridine in terms of their C–H BDEs. Thus, the pyridyl radical ($C_5H_4N^{\bullet}$) radical attacks a molecular benzene ring to from sp^3-like transition state (eqn (1)), which would release a hydrogen atom to give PhPs (eqn (2)). Small KIE observed in the reaction with benzene-d_6 (Table 6, entry 3, k_H/k_D value was 1.1) indicates the presence of another route to form PhPs which involves the C–H bond cleavage in benzene. KIEs for BPs in the reaction with pyridine-d_5 and for BPh in that with benzene-d_6 (Table 6, entries 2 and 3) also evidenced that RDSs in the formation of BPs and BPh are the C–H bond cleavage in pyridine and benzene, respectively.

Table 6 Results of isotope experiments[a]

Entry	λ / nm	Deuterated compound	Product / μmol, (k_H/k_D)[b]		
			PhPs	BPs	BPh
1	> 350	-	17	4.3	3.0
2		C_6D_5N	8.8 (1.9)	1.5 (2.9)	4.1 (0.74)
3		C_6D_6	15 (1.1)	6.3 (0.70)	0.76 (4.0)
4	> 400	-	5.2	0.45	0.80
5		C_6D_5N	2.7 (1.9)	0.27 (1.7)	1.1 (0.71)
6		C_6D_6	4.3 (1.2)	0.47 (0.96)	0.12 (7.0)

[a] Reaction conditions: pyridine (0.05 mL, 0.62 mmol) and benzene (0.95 mL, 11 mmol) with the Pd/TiO_2 photocatalyst (0.1 g) were used, the reaction time was 1 h. [b] The values in parentheses: k_H/k_D = (amount of the products in entry 1) / (that in entry 2 or 3) or (that in entry 4) / (that in entry 5 or 6).

On the other hand, the k_H/k_D value was less than unity for the homo-coupling of non-deuterated compound (Table 6, BPh in entry 2 and BPs in entry 3), that is, inverse KIEs were observed. This can be interpreted by competitive oxidation of pyridine and benzene. During the reaction, the two molecules are supposed to competitively consume the limited number of photogenerated hole in TiO_2. Since C–D bond is stronger than C–H bond, the use of deuterated compound instead of the normal compound would slow down the oxidation of the corresponding compound. This would increase the availability of the hole for the counter compound and accelerate its oxidation, resulting in the higher yield of the homo-coupling products of non-deuterated compound. Thus, together with the discussion for the result of PhPs, it is suggested that at least two processes take place for the cross-coupling in the presence of UV light; radical addition and elimination between pyridyl radical and benzene ring (eqns (1) and (2)), and minor radical-radical coupling between pyridyl radical and phenyl radical (eqn (3)). Another possible process is radical addition and elimination between pyridine and phenyl radical (eqns (4) and (5)). The lower selectivity in the presence of UV light (Table 1, entry 1) than that under visible light (Table 1, entry 2, 3) suggests that large numbers of pyridyl and phenyl radical species give these products through many reaction routes.

$$^{\bullet}C_5H_4N + C_6H_6 \rightarrow [C_5H_4N–C_6H_6]^{\bullet} \quad (1)$$

$$[C_5H_4N–C_6H_6]^{\bullet} \rightarrow C_{11}H_9N\ (PhPs) + H^{\bullet} \quad (2)$$

$$^{\bullet}C_5H_4N + {}^{\bullet}C_6H_5 \rightarrow C_5H_5N–C_6H_5 \quad (3)$$

$$C_5H_5N + {}^{\bullet}C_6H_5 \rightarrow [C_5H_5N–C_6H_5]^{\bullet} \quad (4)$$

$$[C_5H_5N–C_6H_5]^{\bullet} \rightarrow C_{11}H_9N\ (PhPs) + H^{\bullet} \quad (5)$$

Under visible light, the k_H/k_D values for PhPs and BPs in the reaction with pyridine-d_5 were 1.9 and 1.7, respectively (Table 6, entry 5) and the k_H/k_D value for BPh in that

with benzene-d_6 was 7.0 (Table 6, entry 6). These KIEs confirmed that RDSs in their formations under visible light are the same as discussed above in the UV light case: RDS in the formation of PhPs and BPs is C–H bond cleavage in pyridine, while RDS in the formation of BPh is that in benzene. Simultaneously, it was suggested that the C–H bond dissociation by the hole takes place only in pyridine during the formation of PhPs by considering their C–H BDEs. On the other hand, the yield of BPs was not changed in the reaction with benzene-d_6 (Table 6, entry 6, the k_H/k_D value was 0.96) while inverse KIE was still observed for BPh in the reaction with pyridine-d_5 (Table 6, entry 5, the k_H/k_D value was 0.71). This different result from the UV light case suggests that the competitive oxidation of pyridine and benzene is not the case in this condition. Reaction under visible light would be initiated by the LMCT excitation of pyridine-TiO_2 surface complex as suggested from larger adsorption amount and higher visible-light activity of pyridine than benzene (Table 4 and Table 5). The surface radical cation produces pyridyl radical by its deprotonation or oxidation of another pyridine molecule, and the radical attacks benzene ring. The cross-coupling proceeds through a radical addition and elimination mechanism. The use of excess amount of benzene to pyridine would allow selective addition of the pyridyl radical to benzene due to high collision frequency between the radical and benzene. Due to the low concentration of pyridine, homo-coupling of pyridyl radicals to form BPs would also be suppressed for the same reason. The low rate for BPh formation suggests the less reactivity of the pyridine radical cation to benzene for phenyl radical formation. The inverse KIE for BPh in the reaction with pyridine-d_5 could be due to faster formation of phenyl radical through the oxidation of benzene instead of pyridine by the pyridine radical cation.

Proposed reaction mechanism

Based on all the results, tentative reaction mechanism is proposed as follows. Since the different light conditions gave different results, it is obvious that the UV light and the visible light give different reaction mechanisms.

In the light including both UV and visible light, the contribution by the UV light excitation would be much predominant (Fig. 4A). The UV light excited the TiO_2 photocatalyst to give photogenerated electrons and holes in the conduction band and valence band, respectively. The electrons are transferred to the Pd nanoparticles, while the holes are trapped on the TiO_2 surface (step i). Pyridine and benzene are

competitively oxidized by the holes to the corresponding radical species (steps ii and iii). Then, the radical–radical coupling of these radicals affords the DCC products (PhPs, step iv) as well as the homo-coupled products (BPs and BPh, steps v and vi). Protons are reduced by electrons on the Pd cocatalyst to give molecular hydrogen (step vii). This is a two-photon process (Fig. 4A). Another possible route to form the cross-coupling product is the radical addition–elimination: addition of the pyridyl radical to a benzene molecule to form an sp^3-centered transition state, and the elimination of a hydrogen radical from this transition state (steps viii and ix). In this case, the proton is reduced by the electron on the Pd nanoparticles, followed by a reaction with the hydrogen radical to give molecular hydrogen (step x). The step ix itself would be thermodynamically favorable since the molecule can regain its aromaticity by releasing a H radical. Therefore, acceleration of a H radical elimination by other species or proton elimination by further photoexcitation of the transition state would not be necessary.

Under visible-light irradiation (Fig. 4B), the surface complex consisting of adsorbed pyridine and a Ti cation, in which an acid–base N–Ti coordinate bond is formed using the lone pair on the nitrogen atom (step xi), is photoexcited to generate an excited electron from the lone pair. The electron is injected into the conduction band of TiO_2 via the surface Ti cation, followed by transfer to the deposited Pd nanoparticles, while a hole remains as a pyridine radical cation (step xii). The radical cation is deprotonated (step xiii) or oxidizes another pyridine molecule (step xiv) to produce a pyridyl radical and a proton, and the DCC reaction proceeds through the radical addition–elimination process between the pyridyl radical and a benzene molecule (step xv and xvi). The adsorbed pyridine molecules would not be static on the surface but rather dynamic in an adsorption-desorption equilibrium, that is, they act not only as a visible-light-harvesting group but also as a substrate. Apart from the LMCT sites, the proton is reduced by the electron on the Pd nanoparticles, followed by a reaction with the hydrogen radical to give molecular hydrogen (step xvii). The reaction under visible light should be a one-photon process (Fig. 4B). In this mechanism, pyridine radical cation forms selectively instead of the photogenerated holes, suppressing the formation of phenyl radical. Therefore, the homo-coupling of benzene is suppressed. In addition, the attack of pyridine radical to benzene ring is dominant due to excess amount of benzene, suppressing the homo-coupling of pyridine.

Under UV light

$$Pd/TiO_2 + h\nu \rightarrow e^-_{Pd} + h^+_{TiO2} \quad \text{(i)}$$

$$C_5H_5N + h^+_{TiO2} \rightarrow {}^{\bullet}C_5H_4N + H^+ \quad \text{(ii)}$$

$$C_6H_6 + h^+_{TiO2} \rightarrow {}^{\bullet}C_6H_5 + H^+ \quad \text{(iii)}$$

$${}^{\bullet}C_5H_4N + {}^{\bullet}C_6H_5 \rightarrow C_{11}H_9N\ (PhPs) \quad \text{(iv)}$$

$${}^{\bullet}C_5H_4N + {}^{\bullet}C_5H_4N \rightarrow C_{10}H_8N_2\ (BPs) \quad \text{(v)}$$

$${}^{\bullet}C_6H_6 + {}^{\bullet}C_6H_6 \rightarrow C_{12}H_{12}\ (BPh) \quad \text{(vi)}$$

$$2H^+ + 2e^-_{Pd} \rightarrow H_2 \quad \text{(vii)}$$

$${}^{\bullet}C_5H_4N + C_6H_6 \rightarrow [C_5H_5N–C_6H_6]^{\bullet} \quad \text{(viii)}$$

$$[C_5H_5N–C_6H_6]^{\bullet} \rightarrow C_{11}H_9N\ (PhPs) + H^{\bullet} \quad \text{(ix)}$$

$$H^+ + H^{\bullet} + e^-_{Pd} \rightarrow H_2 \quad \text{(x)}$$

Under visible light

$$C_5H_5N + TiO_2 \rightarrow C_5H_5N–TiO_2\ (\text{surface complex}) \quad \text{(xi)}$$

$$C_5H_5N–TiO_2\ (\text{surface complex}) \rightarrow C_5H_5N^{\bullet+} + TiO_2\ (e^-_{Pd}) \quad \text{(xii)}$$

$$C_5H_5N^{\bullet+} \rightarrow {}^{\bullet}C_5H_4N + H^+ \quad \text{(xiii)}$$

$$C_5H_5N^{\bullet+} + C_5H_5N \rightarrow C_5H_5N + {}^{\bullet}C_5H_4N + H^+ \quad \text{(xiv)}$$

$${}^{\bullet}C_5H_4N + C_6H_6 \rightarrow [C_5H_5N–C_6H_6]^{\bullet} \quad \text{(xv)}$$

$$[C_5H_5N–C_6H_6]^{\bullet} \rightarrow C_{11}H_9N\ (PhPs) + H^{\bullet} \quad \text{(xvi)}$$

$$H^+ + H^{\bullet} + e^-_{Pd} \rightarrow H_2 \quad \text{(xvii)}$$

(A)

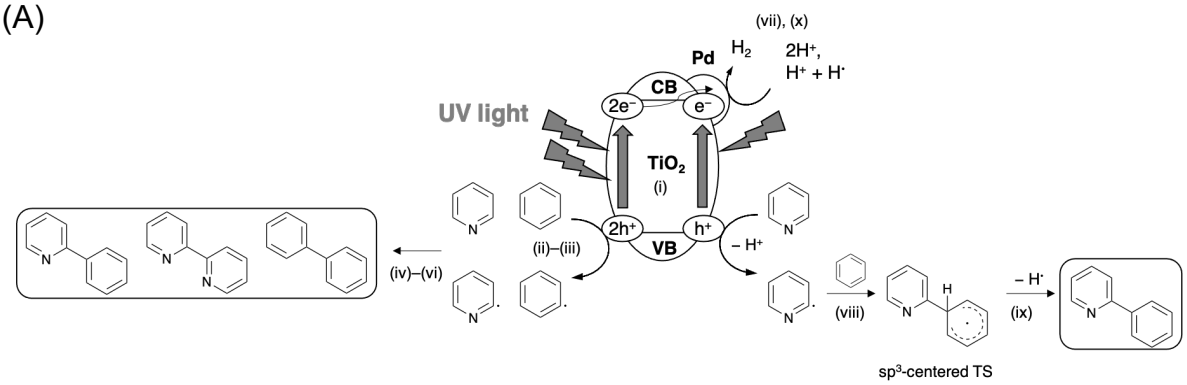

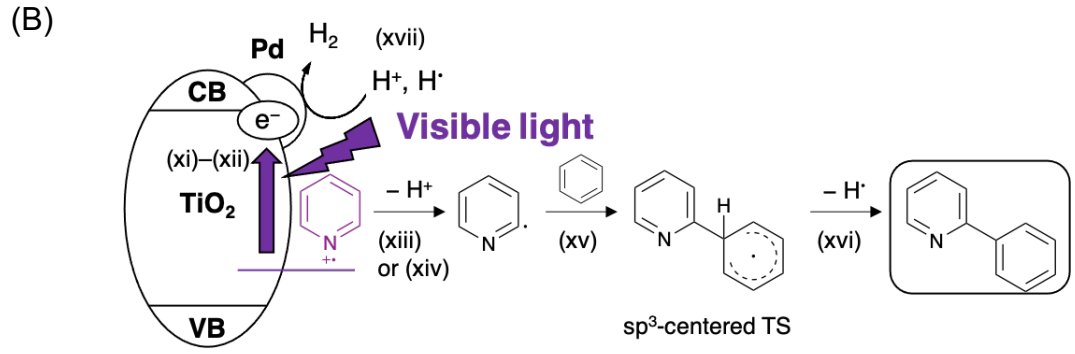

Fig. 4 Schematic image of tentative reaction mechanism under UV and visible light (A), and visible light (B). 2-PhP and 2,2'-BP were chosen as representative products among PhPs and BPs, respectively.

Conclusion

LMCT excitation of the pyridine-TiO_2 surface complex by visible light was utilized to promote DCC between pyridine and benzene. The presence of the excess amount of benzene is important to obtain high selectivity. The selective formation of radical species due to the unique mechanism was successfully demonstrated. Although the efficiency of the reaction and product yield are not satisfactory, this study expanded the possible use of aromatic-semiconductor surface complex systems for DCC reactions, in which the selectivity can be improved merely by changing the irradiation wavelength without any additives or modifications of the photocatalyst.

References

1. Yeung, C. S. & Dong, V. M. Catalytic dehydrogenative cross-coupling: Forming carbon-carbon bonds by oxidizing two carbon-hydrogen bonds. *Chem. Rev.* **111**, 1215–1292 (2011).
2. Li, C. Cross-Dehydrogenative Coupling (CDC): Exploring C–C Bond Formations beyond Functional Group Transformations. *Acc. Chem. Res.* **42**, 335–344 (2009).
3. Girard, S. A., Knauber, T. & Li, C. J. The cross-dehydrogenative coupling of C_{sp^3}-H bonds: A versatile strategy for C-C bond formations. *Angew. Chemie - Int. Ed.* **53**, 74–100 (2014).
4. Xie, J., Jin, H., Xu, P. & Zhu, C. When C-H bond functionalization meets visible-light photoredox catalysis. *Tetrahedron Lett.* **55**, 36–48 (2014).
5. Rueping, M. *et al.* Light-mediated heterogeneous cross dehydrogenative coupling reactions: Metal oxides as efficient, recyclable, photoredox catalysts in C-C bond-forming reactions. *Chem. - A Eur. J.* **18**, 3478–3481 (2012).

6. Yi, H. *et al.* Photocatalytic Dehydrogenative Cross-Coupling of Alkenes with Alcohols or Azoles without External Oxidant. *Angew. Chemie - Int. Ed.* **56**, 1120–1124 (2017).
7. Liu, Q. *et al.* Reactivity and mechanistic insight into visible-light-induced aerobic cross-dehydrogenative coupling reaction by organophotocatalysts. *Chem. - A Eur. J.* **18**, 620–627 (2012).
8. Liu, C. *et al.* Oxidative Coupling between Two Hydrocarbons: An Update of Recent C-H Functionalizations. *Chem. Rev.* **115**, 12138–12204 (2015).
9. Yoshida, H., Fujimura, Y., Yuzawa, H., Kumagai, J. & Yoshida, T. A heterogeneous palladium catalyst hybridised with a titanium dioxide photocatalyst for direct C-C bond formation between an aromatic ring and acetonitrile. *Chem. Commun.* **49**, 3793–3795 (2013).
10. Tyagi, A., Matsumoto, T., Kato, T. & Yoshida, H. Direct C–H bond activation of ethers and successive C–C bond formation with benzene by a bifunctional palladium-titania photocatalyst. *Catal. Sci. Technol.* **6**, 4577–4583 (2016).
11. Tyagi, A., Yamamoto, A., Kato, T. & Yoshida, H. Bifunctional property of Pt nanoparticles deposited on TiO_2 for the photocatalytic sp^3 C–sp^3 C cross-coupling reactions between THF and alkanes. *Catal. Sci. Technol.* **7**, 2616–2623 (2017).
12. Wada, E. *et al.* Direct cyanomethylation of aliphatic and aromatic hydrocarbons with acetonitrile over a metal loaded titanium oxide photocatalyst. *Catal. Sci. Technol.* **7**, 2457–2466 (2017).
13. Mazloomi, K. & Gomes, C. Hydrogen as an energy carrier: Prospects and challenges. *Renew. Sustain. Energy Rev.* **16**, 3024–3033 (2012).
14. Hoffmann, N. Photocatalysis with TiO_2 Applied to Organic Synthesis. *Aust. J. Chem* **68**, 1621–1639 (2015).
15. Oi, L. E. *et al.* Recent advances of titanium dioxide (TiO_2) for green organic synthesis. *RSC Adv.* **6**, 108741–108754 (2016).
16. Liu, A., Lu, C., Chen, C., Li, S. & Ma, D. TiO_2 photocatalysis for C–C bond formation. *Catal. Sci. Technol.* **8**, 2030–2045 (2018).
17. Wang, Y. *et al.* TiO_2 Photocatalyzed C–H Bond Transformation for C–C Coupling Reactions. *Catalysts* **8**, 355 (2018).
18. Park, S., Jeong, J., Fujita, K. I., Yamamoto, A. & Yoshida, H. Anti-Markovnikov Hydroamination of Alkenes with Aqueous Ammonia by Metal-Loaded Titanium Oxide Photocatalyst. *J. Am. Chem. Soc.* **142**, 12708–12714 (2020).
19. Tyagi, A., Yamamoto, A., Yamamoto, M., Yoshida, T. & Yoshida, H. Direct cross-coupling between alkenes and tetrahydrofuran with a platinum-loaded titanium oxide photocatalyst. *Catal. Sci. Technol.* **8**, 2546–2556 (2018).
20. Zhang, G., Kim, G. & Choi, W. Visible light driven photocatalysis mediated via ligand-to-metal charge transfer ({LMCT}): an alternative approach to solar activation of titania.

Energy Environ. Sci. **7**, 954–966 (2014).

21. Franchi, D. & Amara, Z. Applications of Sensitized Semiconductors as Heterogeneous Visible-Light Photocatalysts in Organic Synthesis. *ACS Sustain. Chem. Eng.* **8**, 15405–15429 (2020).
22. Yamamoto, A., Ohara, T. & Yoshida, H. Visible-light-induced photocatalytic benzene/cyclohexane cross-coupling utilizing a ligand-to-metal charge transfer benzene complex adsorbed on titanium oxides. *Catal. Sci. Technol.* **8**, 2046–2050 (2018).
23. Naniwa, S., Tyagi, A., Yamamoto, A. & Yoshida, H. Visible-light photoexcitation of pyridine surface complex, leading to selective dehydrogenative cross-coupling with cyclohexane. *Phys. Chem. Chem. Phys.* **20**, 28375–28381 (2018).
24. Higashimoto, S. *et al.* Selective photocatalytic oxidation of benzyl alcohol and its derivatives into corresponding aldehydes by molecular oxygen on titanium dioxide under visible light irradiation. *J. Catal.* **266**, 279–285 (2009).
25. Zhu, S. *et al.* Ultrathin nanosheets of molecular sieve SAPO-5: A new photocatalyst for efficient photocatalytic reduction of CO_2 with H_2O to methane. *Appl. Catal. B Environ.* **187**, 11–18 (2016).
26. Higashimoto, S. *et al.* Selective Photocatalytic Oxidation of Benzyl Amine By O_2 Into N-Benzylidenebenzylamine on TiO_2 Using Visible Light. *Curr. Org. Chem.* **17**, 2374–2381 (2013).
27. Lang, X. *et al.* Visible-light-induced selective photocatalytic aerobic oxidation of amines into imines on TiO_2. *Chem. - A Eur. J.* **18**, 2624–2631 (2012).
28. Lang, X. *et al.* Tertiary amine mediated aerobic oxidation of sulfides into sulfoxides by visible-light photoredox catalysis on TiO_2. *Chem. Sci.* **6**, 5000–5005 (2015).
29. Kamegawa, T., Seto, H., Matsuura, S. & Yamashita, H. Preparation of hydroxynaphthalene-modified TiO_2 via formation of surface complexes and their applications in the photocatalytic reduction of nitrobenzene under visible-light irradiation. *ACS Appl. Mater. Interfaces* **4**, 6635–6639 (2012).
30. Kamegawa, T., Matsuura, S., Seto, H. & Yamashita, H. A visible-light-harvesting assembly with a sulfocalixarene linker between dyes and a Pt-TiO_2 photocatalyst. *Angew. Chemie - Int. Ed.* **52**, 916–919 (2013).
31. Hassan, J., Sévignon, M., Gozzi, C., Schulz, E. & Lemaire, M. Aryl-aryl bond formation one century after the discovery of the Ullmann reaction. *Chem. Rev.* **102**, 1359–1469 (2002).
32. Wang, C. M., Heller, A. & Gerischer, H. Palladium catalysis of O_2 reduction by electrons accumulated on TiO_2 particles during photoassisted oxidation of organic compounds. *J. Am. Chem. Soc.* **114**, 5230–5234 (1992).
33. Subramanian, V., Wolf, E. E. & Kamat, P. V. Catalysis with TiO_2/Gold Nanocomposites. Effect of Metal Particle Size on the Fermi Level Equilibration. *J. Am. Chem. Soc.* **126**,

4943–4950 (2004).

34. Yang, J., Wang, D., Han, H. & Li, C. Roles of cocatalysts in photocatalysis and photoelectrocatalysis. *Acc. Chem. Res.* **46**, 1900–1909 (2013).

Part II

Relationship between Specific Surface Area, Carrier Lifetime and Photocatalytic Activity

Introduction of Part II

Photocatalysis is a multistep reaction in which chemical reactions at a solid surface and the dynamics of photoexcited carriers are intertwined in a complicated manner. Thus, the activity of photocatalysts is influenced by various structural and physicochemical parameters. Understanding the relationship between these parameters and photocatalytic activity is the key to designing efficient photocatalytic systems. Among those affecting photocatalytic activity, specific surface area (SSA) and carrier lifetime are decisive parameters since the former correlates with the concentration of reactants adsorbed on the surface of the photocatalyst and the latter does with that of the photoexcited carriers.

Specific Surface Area, Particle Size, and Photocatalytic Activity

SSA, which is defined as surface area per gram of a photocatalyst, or particle size is one of the most studied parameters. SSA is usually determined by Brunauer-Emmett-Teller (BET) analysis on nitrogen adsorption measurements while particle size is determined by several methods such as X-ray powder diffraction (XRD) and electron microscopy. They often have a negative correlation with each other; the larger SSA, the smaller particle size.

The expected role of SSA and particle size in photocatalysis is slightly different from that in conventional thermal catalysis. In thermal catalysis, they often correspond to the number of active sites per unit mass of the catalyst. On the other hand, the definition of active sites is not clear in photocatalysis since the active sites in photocatalysis are not specific surface sites but the photoexcited carriers trapped on the surface atoms, and currently, there is no way to directly quantify the number of these carriers participate in the reaction. In this way, photocatalytic activity is often evaluated just as a reaction rate, not as the rate per active site (turnover frequency, TOF) like in thermal catalysis. Nevertheless, an increase in SSA (a decrease in particle size) increases the number of adsorption sites for the reactants per unit mass and should improve photocatalytic activity. Many researchers reported a positive effect of SSA on photocatalytic activity.[1–4] Importantly, the effect of SSA is different depending on the photocatalyst and the reaction condition. For example, a plateau or a volcano-shaped effect is sometimes observed.[5–8] This is often explained by a change in the rate-determining step from the adsorption of the reactant to other steps such as photoabsorption of the photocatalyst or the effect of other factors. Different effect of SSA depending on the photocatalyst is also reported.[4]

They reported that fluorine- and boron-doped TiO_2 samples calcined at high temperature showed a larger effect of SSA than that samples, which is explained by higher crystallinity to increase the lifetime of photoexcited carriers. All the explanations on the contribution of other parameters are made qualitatively in these examples. Such a qualitative explanation is often observed to explain a complex dependence of photocatalytic activity on the target parameter.

Carrier Lifetime and Photocatalytic Activity

The dynamics of photoexcited carriers is also important in photocatalysis. Especially, carrier lifetime is regarded as one of the decisive factors of photocatalytic activity since it strongly correlates with the concentration of photocarriers, which activate the reactants adsorbed on the photocatalyst. Carrier lifetime can be estimated by several methods such as photoluminescence (PL),[9–12] time-resolved microwave conductivity (TRMC),[13–16] X-ray photoelectron spectroscopy (XPS),[17,18] and transient absorption (TA) spectroscopy.[19–27] Since these methods depend on a different principle, carrier lifetime varies from a few picoseconds to milliseconds depending on the method as well as the measurement condition such as time resolution and excitation laser intensity. This sometimes causes a discrepancy between results in different papers, making it difficult to find a general and quantitative relationship between carrier lifetime and photocatalytic activity. Nevertheless, many researchers have studied the relationship by employing different methods for the estimation of carrier lifetime. Ideally, a long carrier lifetime should improve the photocatalytic activity since it provides more photoexcited carriers to activate the reactant.[28,29] However, such a clear correlation is not always observed. Especially in powder photocatalysts, which are commonly used in the study of photocatalysis, the effect is often non-linear[29,30] or sometimes negligible.[31,32] This is often explained by the effects of other factors such as SSA or the adsorption properties of the photocatalyst in a qualitative manner.

Structural Parameters and Carrier Lifetime

Carrier lifetime is an important parameter for photocatalytic activity. Thus, understanding the relationship between structural parameters and carrier lifetime is important for the better design of photocatalysts. Various structural parameters can affect carrier lifetime. Generally, lattice defects in photocatalysts such as oxygen vacancies and interstitial atoms can act as a trapping center of photoexcited carriers to promote the recombination of the carriers.

Since these defects mainly exist near the surface of photocatalysts, large SSA usually decreases carrier lifetime.[14,20] This indicates that the effects of SSA and carrier lifetime on photocatalytic activity are in a trade-off relationship, in which large SSA not only increases but also decreases the activity by decreasing carrier lifetime.[33] Currently, however, there is no quantitative explanation for this trade-off relationship.

Other factors than SSA can also affect carrier lifetime. The most common way to increase carrier lifetime is the loading of metal cocatalysts.[34] Metal nanoparticles such as Pt and Pd can receive photoexcited electrons to suppress the charge recombination. Crystal structure also affects carrier lifetime.[35,36] In anatase TiO_2, most of the electrons survive as free or shallowly trapped electrons, which explains the high activity of anatase TiO_2 for reduction processes. In rutile TiO_2, in contrast, electrons are deeply trapped within a few picoseconds after photoexcitation. The deep trapping of photoexcited electrons elongates the lifetime of holes, making rutile TiO_2 highly active for multi-oxidation processes such as water oxidation. The different lifetime of free electrons leads to the different energy states of photoexcited carriers depending on the crystal structure.

Outlines of Part II

Obviously, photocatalytic activity cannot be explained by a single parameter even if the parameter is regarded as decisive one such as SSA or carrier lifetime. Thus, there is a need to elucidate how much each of these parameters contribute to photocatalytic activity. However, their contributions are discussed mostly in a qualitative manner, in which the effect of each parameter is discussed individually, failing to give a quantitative understanding on their contributions. In Part II, we used a statistical approach to study a quantitative relation of SSA and carrier lifetime to photocatalytic activity of anatase TiO_2 as well as time-resolved absorption spectroscopy to study the relationship between SSA and dynamics of photoexcited carriers.

In Chapter 4, time-resolved visible-to-midIR absorption spectroscopy was carried out to investigate the effect of SSA on the energy states and dynamics of photoexcited carriers. We found that most of the carriers exist as trapped carriers when SSA is large while they survive as free carriers when SSA is small, and both free and trapped electrons exist when SSA is moderate.

In Chapter 5, we used a statistical approach based on a simple kinetic model to elucidate the quantitative relation of SSA and carrier lifetime (τ) to the activity of anatase TiO_2

photocatalysts. The activities of 21 different TiO_2 photocatalysts were examined in the dehydrogenative homo-coupling of benzene. We found that these activities can be explained by a simple kinetic model which has SSA and τ as variables. The model quantitatively explained the relation of SSA and τ to the photocatalytic activity as well as their interdependency. It also suggested that their effect on the activity can be varied depending on the value of their product (SSA•τ); the effect becomes nonlinear, linear, and negligible with increasing the value of their product. Thus, the product of SSA and carrier lifetime was proposed as a quantitative indicator of their effect on photocatalytic activity.

References

1. Xu, N. *et al.* Effects of particle size of TiO_2 on photocatalytic degradation of methylene blue in aqueous suspensions. *Ind. Eng. Chem. Res.* **38**, 373–379 (1999).
2. Amano, F., Nogami, K., Tanaka, M. & Ohtani, B. Correlation between surface area and photocatalytic activity for acetaldehyde decomposition over bismuth tungstate particles with a hierarchical structure. *Langmuir* **26**, 7174–7180 (2010).
3. Strauss, M., Pastorello, M., Sigoli, F. A., De Souza E Silva, J. M. & Mazali, I. O. Singular effect of crystallite size on the charge carrier generation and photocatalytic activity of nano-TiO_2. *Appl. Surf. Sci.* **319**, 151–157 (2014).
4. Dozzi, M. V., Artiglia, L., Granozzi, G., Ohtani, B. & Selli, E. Photocatalytic activity vs structural features of titanium dioxide materials singly doped or codoped with fluorine and boron. *J. Phys. Chem. C* **118**, 25579–25589 (2014).
5. Yamazoe, S., Okumura, T., Teramura, K. & Tanaka, T. Development of the efficient TiO_2 photocatalyst in photoassisted selective catalytic reduction of NO with NH_3. *Catal. Today* **111**, 266–270 (2006).
6. Tryba, B., Toyoda, M., Morawski, A. W., Nonaka, R. & Inagaki, M. Photocatalytic activity and OH radical formation on TiO_2 in the relation to crystallinity. *Appl. Catal. B Environ.* **71**, 163–168 (2007).
7. Carneiro, J. T., Savenije, T. J., Moulijn, J. A. & Mul, G. Toward a physically sound structure-activity relationship of TiO_2-based photocatalysts. *J. Phys. Chem. C* **114**, 327–332 (2010).
8. Murakami, N., Kawakami, S., Tsubota, T. & Ohno, T. Dependence of photocatalytic activity on particle size of a shape-controlled anatase titanium(IV) oxide nanocrystal. *J. Mol. Catal. A Chem.* **358**, 106–111 (2012).
9. Wakabayashi, K., Yamaguchi, Y., Sekiya, T. & Kurita, S. Time-resolved luminescence spectra in colorless anatase TiO_2 single crystal. *J. Lumin.* **112**, 50–53 (2005).
10. Hashimoto, T., Takahashi, K., Kunugita, H., Sakama, H. & Ema, K. Dynamics of photo-

excited carriers in anatase TiO_2 thin film investigated by pump-probe method. *J. Phys. Conf. Ser.* **193**, (2009).

11. Cavigli, L., Bogani, F., Vinattieri, A., Faso, V. & Baldi, G. Volume versus surface-mediated recombination in anatase TiO_2 nanoparticles. *J. Appl. Phys.* **106**, (2009).
12. Brüninghoff, R. *et al.* Time-Dependent Photoluminescence of Nanostructured Anatase TiO_2 and the Role of Bulk and Surface Processes. *J. Phys. Chem. C* **123**, 26653–26661 (2019).
13. Micic, O. I., Zhang, Y., Cromack, K. R., Trifunac, A. D. & Thurnauer, M. C. Trapped holes on titania colloids studied by electron paramagnetic resonance. *J. Phys. Chem.* **97**, 7277–7283 (1993).
14. Colbeau-Justin, C., Kunst, M. & Huguenin, D. Structural influence on charge-carrier lifetimes in TiO_2 powders studied by microwave absorption. *J. Mater. Sci.* **38**, 2429–2437 (2003).
15. Warman, J. M. *et al.* Electronic processes in semiconductor materials studied by nanosecond time-resolved microwave conductivity-III. Al_2O_3, MgO and TiO_2 powders. *Int. J. Radiat. Appl. Instrumentation. Part* **37**, 433–442 (1991).
16. Schindler, K. M. & Kunst, M. Charge-carrier dynamics in TiO_2 powders. *J. Phys. Chem.* **94**, 8222–8226 (1990).
17. Ozawa, K. *et al.* What Determines the Lifetime of Photoexcited Carriers on TiO_2 Surfaces? *J. Phys. Chem. C* **120**, 29283–29289 (2016).
18. Ozawa, K., Yamamoto, S., Mase, K. & Matsuda, I. A surface science approach to unveiling the TiO_2 photocatalytic mechanism: Correlation between photocatalytic activity and carrier lifetime. *e-Journal Surf. Sci. Nanotechnol.* **17**, 130–147 (2019).
19. Rothenberger, G., Moser, J., Gratzel, M., Serpone, N. & Sharma, D. K. Charge carrier trapping and recombination dynamics in small semiconductor particles. *J. Am. Chem. Soc.* **107**, 8054–8059 (1985).
20. Serpone, N., Lawless, D., Khairutdinov, R. & Pelizzetti, E. Subnanosecond relaxation dynamics in TiO_2 colloidal sols (particle sizes R_p = 1.0-13.4 nm). Relevance to heterogeneous photocatalysis. *J. Phys. Chem.* **99**, 16655–16661 (1995).
21. Colombo, D. P. & Bowman, R. M. Does interfacial charge transfer compete with charge carrier recombination? A femtosecond diffuse reflectance investigation of TiO_2 nanoparticles. *J. Phys. Chem.* **100**, 18445–18449 (1996).
22. Furube, A., Asahi, T., Masuhara, H., Yamashita, H. & Anpo, M. Femtosecond diffuse reflectance spectroscopy on some standard TiO_2 powder catalysts. *Chem. Lett.* 735–736 (1997).
23. Furube, A., Asahi, T., Masuhara, H., Yamashita, H. & Anpo, M. Charge carrier dynamics of standard TiO_2 catalysts revealed by femtosecond diffuse reflectance spectroscopy. *J. Phys. Chem. B* **103**, 3120–3127 (1999).

24. Yamakata, A., Ishibashi, T. A. & Onishi, H. Water- and oxygen-induced decay kinetics of photogenerated electrons in TiO_2 and Pt/TiO_2: A time-resolved infrared absorption study. *J. Phys. Chem. B* **105**, 7258–7262 (2001).
25. Yamakata, A., Ishibashi, T. aki, Takeshita, K. & Onishi, H. Time-resolved infrared absorption study of photochemical reactions over metal oxides. *Top. Catal.* **35**, 211–216 (2005).
26. Ruckebusch, C., Sliwa, M., Pernot, P., de Juan, A. & Tauler, R. Comprehensive data analysis of femtosecond transient absorption spectra: A review. *J. Photochem. Photobiol. C Photochem. Rev.* **13**, 1–27 (2012).
27. Freire, J. A. & Emidio, G. A. What can transient absorption spectroscopy reveal about the trap distribution in a semiconductor? *J. Photochem. Photobiol. A Chem.* **393**, 112439 (2020).
28. Xu, M. *et al.* Photocatalytic activity of bulk TiO_2 anatase and rutile single crystals using infrared absorption spectroscopy. *Phys. Rev. Lett.* **106**, 1–4 (2011).
29. Miyasato, R., Fujiwara, M., Sato, H., Yano, T. & Hashimoto, H. Correlation between surface carrier dynamics and water oxidation activity of commercially available rutile-type TiO_2 powders. *Chem. Phys. Lett.* **712**, 123–127 (2018).
30. Dozzi, M. V., D'Andrea, C., Ohtani, B., Valentini, G. & Selli, E. Fluorine-doped TiO_2 materials: Photocatalytic activity vs time-resolved photoluminescence. *J. Phys. Chem. C* **117**, 25586–25595 (2013).
31. Wilke, K. & Breuer, H. D. The influence of transition metal doping on the physical and photocatalytic properties of titania. *J. Photochem. Photobiol. A Chem.* **121**, 49–53 (1999).
32. Paola, A. Di, Ikeda, S., Marcì, G., Ohtani, B. & Palmisano, L. Transition metal doped TiO_2: physical properties and photocatalytic behaviour. *Int. J. Photoenergy* **3**, 171–176 (2001).
33. Emilio, C. A., Litter, M. I., Kunst, M., Bouchard, M. & Colbeau-Justin, C. Phenol photodegradation on platinized-TiO_2 photocatalysts related to charge-carrier dynamics. *Langmuir* **22**, 3606–3613 (2006).
34. Bard, A. J. Photoelectrochemistry. *Science (80-.).* **207**, 139–144 (1980).
35. Yamakata, A., Vequizo, J. J. M. & Matsunaga, H. Distinctive Behavior of Photogenerated Electrons and Holes in Anatase and Rutile TiO_2 Powders. *J. Phys. Chem. C* **119**, 24538–24545 (2015).
36. Yamakata, A. & Vequizo, J. J. M. Curious behaviors of photogenerated electrons and holes at the defects on anatase, rutile, and brookite TiO_2 powders: A review. *J. Photochem. Photobiol. C Photochem. Rev.* **40**, 234–243 (2019).

Chapter 4

Effect of specific surface area on the energy states of photoexcited carriers in anatase TiO_2 nanoparticles

Abstract

Heterogeneous photocatalysis is a promising technology for artificial photosynthesis and environmental remediation. The development of efficient photocatalysts requires a better understanding of the trapping states of photoexcited charge carriers. Although specific surface area (SSA) is an important factor affecting photocatalytic activity, how SSA affects the energy states of the carriers remains unclear. Here we show that SSA changes the population of free and trapped carriers in anatase TiO_2 nanoparticles. We used time-resolved visible to mid-IR absorption spectroscopy to investigate the energy states and dynamics of photoexcited carriers in three TiO_2 samples with different SSA (308, 143, 50 $m^2\ g^{-1}$). We found that in the microsecond region most electrons exist as trapped electrons when SSA is large (308 $m^2\ g^{-1}$) while they survive as free electrons when SSA is small (50 $m^2\ g^{-1}$), and both free and trapped electrons exist when SSA is moderate (143 $m^2\ g^{-1}$). Our results identify SSA as an important factor affecting the energy states of photoexcited carriers in anatase TiO_2 nanoparticles.

Introduction

Heterogeneous photocatalysis is a promising technology for artificial photosynthesis[1–3] and environmental remediation.[4–8] Although a variety of efficient photocatalysts has been developed now, titanium oxide (TiO_2), has still gained much attention both as a base material to develop efficient photocatalysts[9] and as a standard material to understand photocatalysis.[10,11] In photocatalysis, the photocatalyst absorbs light to produce photoexcited charge carriers, which migrate to the surface of the photocatalyst to activate the reactant. During the migration, the carriers can be trapped in various energy states which arise mainly from lattice defects in the photocatalyst, changing their reactivity depending on the energy state. Thus, understanding the behavior and energy states of photoexcited carriers is one of the keys to understand the photocatalytic activity. Recently, we found that different activities of anatase, rutile, and brookite TiO_2 can be explained by different energy states of photoexcited carriers.[12,13] Most electrons survive as free or shallowly trapped electrons in anatase TiO_2. The long lifetime of free electrons is responsible for the high activity of anatase TiO_2, especially in the decomposition of organic molecules,[14–16] in which the reduction of O_2 into superoxide anion radicals would be important. In rutile TiO_2, electrons are deeply trapped within a few picoseconds after photoexcitation. The deep trapping of photoexcited electrons elongates the lifetime of holes, making rutile TiO_2 highly active for multi-oxidation processes such as water oxidation.[15,17,18] Brookite TiO_2 has electron traps with moderate depth between anatase and rutile, retaining moderate activities of both trapped electrons and holes. Thus, it shows higher activity than anatase and rutile TiO_2 in some photocatalytic reactions.[19–21] This result suggested that the energy states of photoexcited carriers is an important factor to determine the photocatalytic activity of TiO_2.

Specific surface area (SSA) of photocatalysts is another important factor to determine photocatalytic activity; larger SSA provides more adsorption sites for the reactant to increase the rate of photocatalytic reactions. On the other hand, larger SSA also offers more surface defects which can promote trapping and recombination of photoexcited carriers.[22] Therefore, SSA should affect the population of free and trapped carriers and thus alter the energy states of photoexcited carriers in the photocatalyst. However, only scattered data are present on how SSA alters the energy states of the photoexcited carriers, despite numbers of studies examining carrier dynamics in TiO_2.[23–28] This is because most of the studies investigated the dynamics of the carrier in a certain energy state or in the limited energy range, failing to elucidate how the carriers are distributed in different energy states at different SSA.

Time-resolved absorption spectroscopy from the visible to mid-IR region is a powerful tool to study the behavior of photogenerated carriers in different energy states. Upon photoexcitation of the photocatalyst, free electrons in the conduction band or those shallowly trapped in the midgap states show a characteristic absorption peak in the mid-IR region[29–34] while holes and deeply trapped electrons give a broad absorption band in the visible to near-IR (NIR) region.[35–39] Simultaneous measurements in the visible to midIR region provide a useful insight into the energy states of these carriers. Moreover, measurements of transient decay of their absorption allow us to investigate trapping processes of the carries in various time resolutions from femtosecond to microsecond, which helps understanding of their resultant energy states by the trapping. In this study, we used time-resolved visible to midIR absorption spectroscopy to investigate the effect of SSA on the energy states of photoexcited carriers in anatase TiO_2 nanoparticles. We examined the energy states of photoexcited carriers in three anatase samples calcined at various temperatures. We found that the trap states of photoexcited carriers depends on SSA; in the microsecond region, most of the carriers exist as trapped carriers when SSA is large while they survive as free carriers when SSA is small, and both free and trapped electrons exist when SSA is moderate. Decay kinetics of photoexcited carriers are also investigated to explain these different energy states of photoexcited carriers.

Experimental

Sample Preparation and Characterization

An anatase TiO_2 powder sample (ST-01, 308 $m^2\ g^{-1}$, 6.3 nm) was supplied by Ishihara Sangyo Kaisha. The sample was calcined at 300 or 600 ºC for 24 h to obtain samples with smaller SSA which are referred to as ST-01_300C (143 $m^2\ g^{-1}$, 14.5 nm) and ST-01_600C (50 $m^2\ g^{-1}$, 28.6 nm). Powder X-ray diffraction (XRD) pattern was recorded by a Shimadzu Lab X XRD-6000 with Cu Kα radiation (40 kV, 30 mA). Their primary particle size was estimated by the Scherrer equation using full width at half maximum of the most intense XRD peaks at ca. 25.3º. Transmission electron microscopy (TEM) images were obtained by a JEOL JEM-2100F(G5) in the Institute for Chemical Research of Kyoto University.

Time-resolved visible to mid-IR absorption measurements

Time-resolved visible to mid-IR absorption measurements were carried out in two

different time resolutions: microsecond and femtosecond. Each TiO_2 powder was fixed on a circular CaF_2 plate with a density of 3 mg cm^{-1} and placed in the closed IR cell for the measurements. Microsecond time-resolved measurements were performed in 20 Torr of N_2, O_2, or methanol vapor by the custom-built spectrometers. In the mid-IR region (6000−1000 cm^{-1}), probe light emitted from a $MoSi_2$ coil was focused on the sample, and the transmitted light was introduced to a grating spectrometer. The monochromated light was detected by an MCT detector (Kolmar), and the output electric signal was amplified with an ac-coupled amplifier (Stanford Research Systems, SR560, 1 MHz). In the visible to NIR region (25000−6000 cm^{-1}), a halogen lamp (50 W) and Si or InGaAs photodiodes were utilized for the probe light and detectors, and the experiments were performed in reflection mode. In each experiment, a 355 nm UV pulse from an Nd:YAG laser (Continuum, Surelite I; duration 6 ns; power 0.5 mJ; repetition rate 5 or 0.5 Hz) was used to excite the band gap of the TiO_2. The time resolution of the spectrometers was limited to 1−2 μs by the bandwidth of the amplifier.

Femtosecond time-resolved measurements were performed in 20 Torr of N_2 using a pump−probe method based on a femtosecond Ti:sapphire laser system (Spectra-Physics, Solstice & TOPAS prime; duration 90 fs; repetition rate 1 kHz). A 355 nm pulse was utilized to excite the photocatalysts with the pulse intensity of 1 μJ. 22000 cm^{-1}, 13000 cm^{-1}, and 2000 cm^{-1} pulses were used for the probe light and detected by a photomultiplier, InGaAs, and an MCT array detector, respectively.

Results and Discussion

Structural Characterization of Anatase TiO_2 Nanoparticles

Figure 1 shows XRD patterns of the samples. All the peaks were assignable to a reference pattern of anatase TiO_2 (ICSD #9852), confirming that the crystal phase of these samples is pure anatase phase. The intensity of these peaks increased and full width at half maximum (FWHM) decreased with increasing calcination temperature (Figure 1(b)–(d)), which evidences a growth of anatase crystals by calcination. This is consistent with the observation in TEM (Figure 2), in which the particle size became larger with increasing the calcination temperature, although accurate determination of particle size was difficult due to strong aggregation of the particles. As a result of the crystal growth, SSA, estimated by the Brunauer–Emmett–Teller (BET) method, decreased from 308 (ST-01) to 143 (ST-01_300C) or 50 $m^{2\ -1}$ (ST-01_600C). The TEM images also showed that ST-01 (Figure 2A, inset) has a turbulent

array of the crystals because of its large SSA and small particle size, while the calcined samples (Figure 2B and C, insets) have a distinct lattice fringe of 0.35 nm, which corresponds to (101) plane of anatase TiO_2. These results confirmed that the samples have different structural properties such as SSA and particle size depending on the calcination temperature, which can affect the energy states of photoexcited carriers.

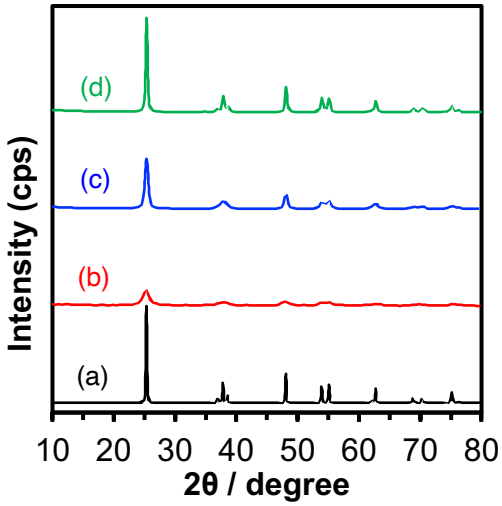

Figure 1. XRD patterns of anatase TiO_2 from a database (ICSD #9852) (a), ST-01 (b), ST-01_300C (c), and ST-01_600C (d).

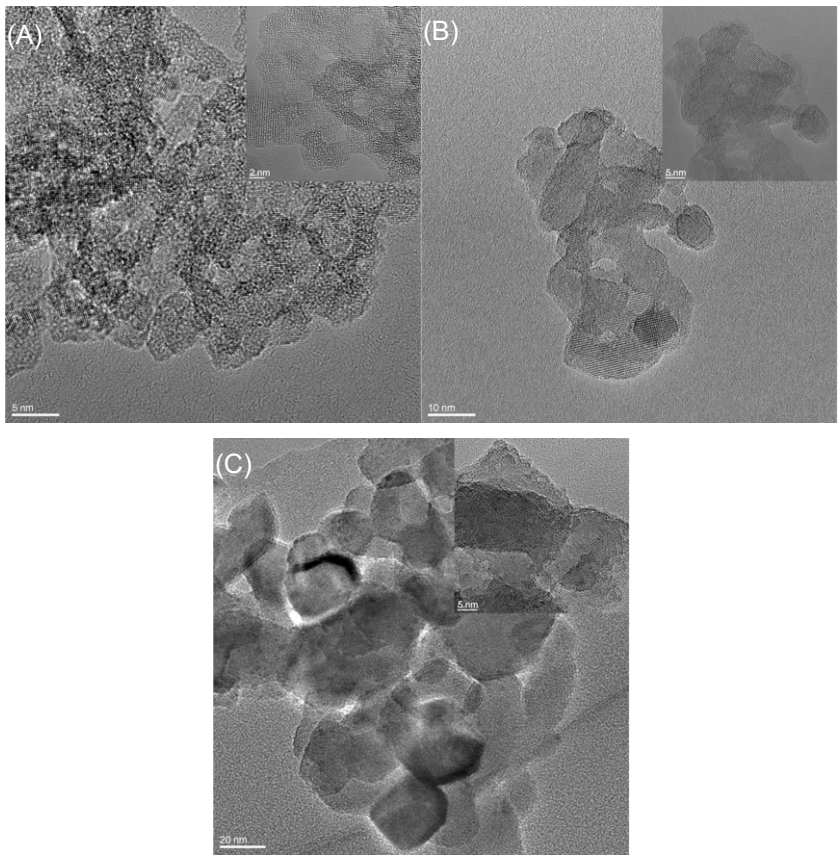

Figure 2. TEM images of ST-01 (A), ST-01_300C (B), and ST-01_600C (C).

Transient Absorption Spectra of Photoexcited Electrons and Holes in Anatase TiO_2 nanoparticles

We next measured transient absorption spectra of photoexcited carriers in these samples (Figure 3). In ST-01 (Figure 3A), a broad absorption band ranging from 25000 to 6000 cm^{-1} (3.1 to 0.7 eV) was observed. This broad band is attributed to absorption by a mixture of trapped electrons and holes.[12,35–38] Since no absorption band of free and/or shallowly trapped electrons were observed below 4000 cm^{-1}, most photoexcited electrons exist as trapped carriers in ST-01. This is probably due to the large SSA of the sample (308 $m^2\ g^{-1}$) which promotes trapping of the carriers on the surface. The absorption of trapped carriers was also observed in a calcined sample (ST-01_300C, 143 $m^2\ g^{-1}$, Figure 3B) but a monotonic absorption band appeared below 4000 cm^{-1}. This monotonic absorption band is ascribed to the intraband transition of free electrons in the conduction band of TiO_2 or the direct transition of shallowly trapped electrons from the midgap states to the conduction band.[29] Since the absorption extends to 1000 cm^{-1} (~0.1 eV), the depth of the shallow traps could be less than 0.1 eV from the bottom of the conduction band (CB), which is sufficiently small for the thermal equilibrium with the free electrons in the CB. Thus, the appearance of the monotonic absorption band means that a part of electrons survive without being trapped in this sample, which is probably due to its smaller SSA than that of ST-01. The absorption intensity of free electrons increased in another calcined sample, ST-01_600C, which has the smallest SSA among three samples (50 $m^2\ g^{-1}$, Figure 3C). Moreover, the absorption of trapped carriers became negligibly smaller in this sample. This means that most electrons exist as free electrons in ST-01_600C. A similar spectral shape was observed in other anatase TiO_2 samples but the absorption of the trapped carriers was not negligible.[12] These samples have larger SSA (76 or 100 $m^2\ g^{-1}$) than ST-01_600C (50 $m^2\ g^{-1}$), which would promote surface trapping of free electrons, resulting in the larger absorbance of the trapped carriers than ST-01_600C. These results suggest that the trapping states of photoexcited carriers in anatase TiO_2 depend on SSA; photoexcited electrons exist as trapped electrons when SSA is large (ST-01, 308 $m^2\ g^{-1}$) while they survive as free electrons when SSA is small (ST-01_600C, 50 $m^2\ g^{-1}$), and both free and trapped electrons exist when SSA is moderate (ST-01_300C, 143 $m^2\ g^{-1}$). The absorbance of free electrons (below 4000 cm^{-1}) increases with decreasing SSA: ST-01 < ST-01_300C < ST-01_600C. This means the lifetime of free electrons in the microsecond region is increased with decreasing SSA. This is probably due to a decrease in the surface defects which promotes the trapping of free electrons. On the other hand, the absorbance of trapped electrons and holes (25000–6000

cm^{-1}) was smallest at the smallest SSA (ST-01_600C) but was largest at moderate SSA, ST01_300C; the order of the absorbance was ST-01_600C < ST-01 < ST-01_300C. This means that large SSA does not necessarily give a large number of trapped carriers. Thus, other factors than SSA should affect the lifetime of trapped carriers.

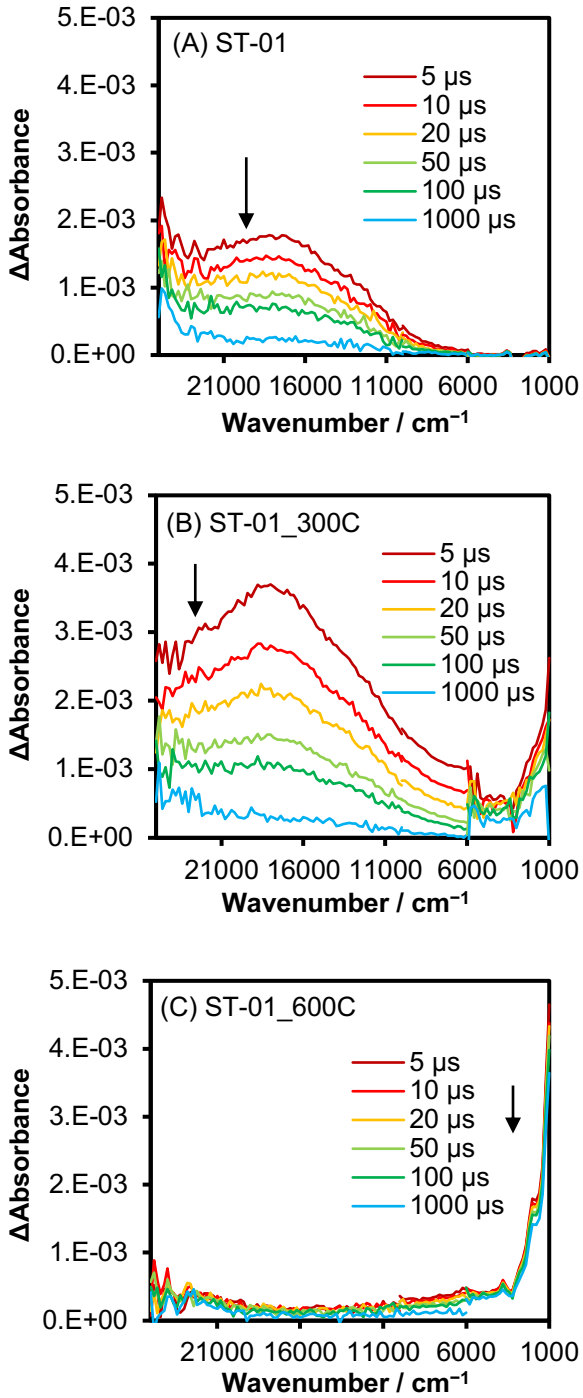

Figure 3. Transient absorption spectra of anatase TiO_2: (A) ST-01 (308 m^2 g^{-1}), (B) that calcined at 300 ºC for 24 h (143 m^2 g^{-1}), and (C) that calcined at 600 ºC for 24 h (50 m^2 g^{-1}) irradiated by UV laser pulses (355 nm, 6 ns duration, 0.5 mJ per pulse, and 5 Hz).

Decay kinetics of Photoexcited Carriers in Anatase TiO_2 nanoparticles

To explain the different energy states of photoexcited carriers, we investigated decay kinetics of transient absorption by the carriers from the picosecond to the microsecond region. 22000, 13000, and 2000 cm^{-1} were chosen as representative wavenumbers of carriers in different energy states.[12] We first checked the assignments of these absorptions by examining their behavior in the presence of an electron scavenger (O_2) or a hole scavenger (methanol) (Figure 4). The absorbance at 2000 cm^{-1} in ST-01 (Figure 4A) decreased by exposure to O_2. This is probably due to the consumption of electrons by O_2. On the other hand, the absorbance increased by exposure to methanol. This can be explained by the consumption of holes by methanol to suppress the recombination with electrons. Similar behavior was observed for other samples (Figure 4B and C). These observations confirmed that the absorbance at 2000 cm^{-1} reflects the number of electrons. On the contrarily, the absorbance at 22000 cm^{-1} (Figure 4D–F) increased upon contact with both O_2 and methanol. This is consistent with previous results that the absorbance is attributed to both trapped electrons and holes.[13] The absorbance at 13000 cm^{-1} in ST-01 (Figure 4G) and ST-01_300C (Figure 4H) showed similar behavior with that at 22000 cm^{-1} but the increase by O_2 was smaller. This indicates that the decrease of the electrons by the reaction with O_2 is larger than 22000 cm^{-1}, implying relatively larger contribution of trapped electrons to the absorption at 13000 cm^{-1}. In ST-01_600C (Figure 4I), the increase by O_2 was relatively larger than in other samples. This indicates the contribution of trapped electrons is smaller than other samples. As shown in the spectrum (Figure 3C), most of the electrons exist as free electrons in this sample. In this case, the number of trapped electrons would be small, making their contribution minor to the absorbance at 13000 cm^{-1}. Therefore, the decrease in the absorbance by exposure to O_2 becomes smaller than that in other samples, resulting in the larger increase upon contact with O_2.

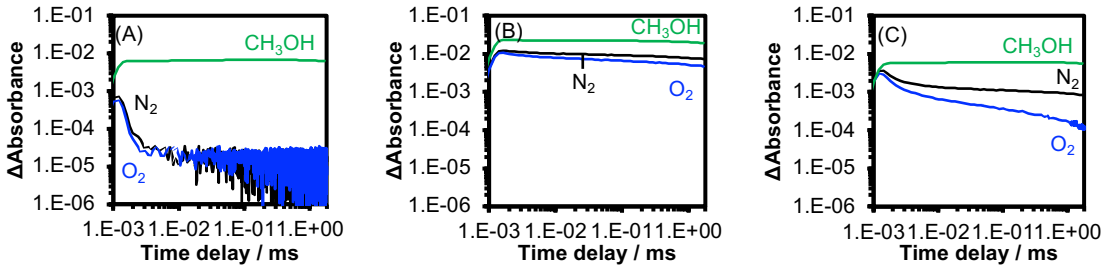

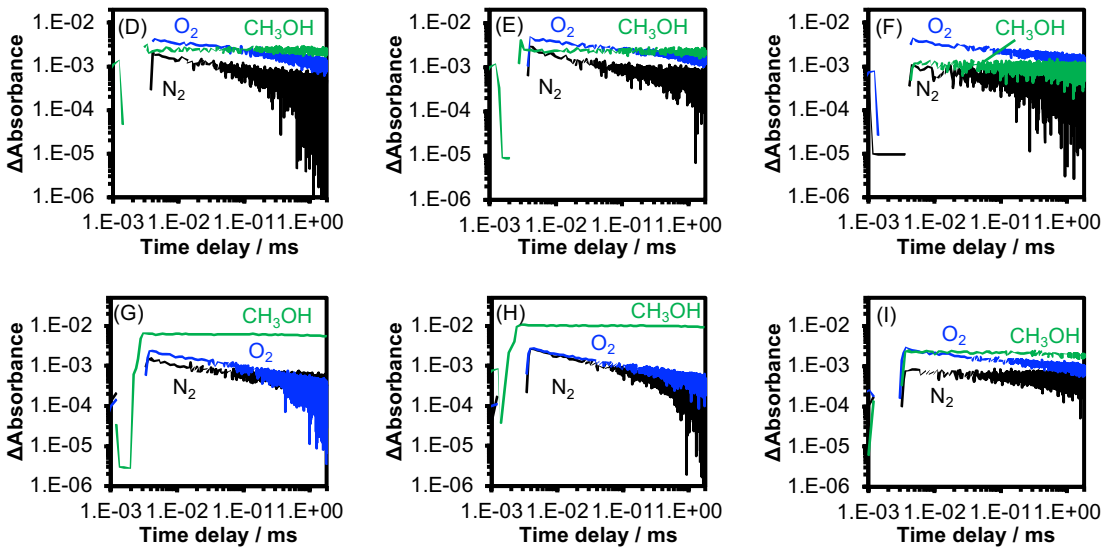

Figure 4. Decay curves of transient absorption by anatase TiO_2 irradiated by UV laser pulses probed at 2000, 22000, and 13000 cm^{-1} in 20 Torr N_2, O_2, and CH_3OH.

These attributions of the transient absorptions of a mixture of electrons and holes can be supported by a numerical simulation using a simple kinetic model.[40] The model is based on the following three assumptions: (i) the recombination rate of the carriers follows the first-order kinetics (eq. 1).[29] (ii) the reaction between an electron–hole pair (e^-–h^+) and an adsorbed scavenger produce the separated carrier (h^-_s or e^-_s) (eq. 2 and 3). (iii) The absorbance reflects the sum of e^-–h^+, h^-_s, and e^-_s. The rates of each step are given by r_1, r_2, and r_3, in which k_1, k_2, k_3, [e^-–h^+], [O_2], and [MeO^-] are the rate constant of the recombination, the electron-consuming reaction, the hole-consuming reaction, and the concentration of electron–hole pairs, oxygen, and methoxy species adsorbed on TiO_2,[31] respectively. Although multiple components were required for the recombination process to reproduce the decay curve, only the single component was considered in this model for the sake of simplicity.

The rate equations for [e^-–h^+], [h^+_s], and [e^-_s] are shown in eq. 4–6, with the use of $k_2' = k_2[O_2]$ and $k_3' = k_3[MeO^-]$ instead of k_2 and k_3. These equations were distilled into their concentrations given by eq. 7–9. In the case of 22000 cm^{-1}, the total number of electrons and holes ([e^-, h^+]$_{total}$), which corresponds to the absorbance, was calculated as [e^-, h^+]$_{total}$ = 2[e^-–h^+] + [h^+_s] + [e^-_s]. The calculated decay curves of [e^-, h^+]$_{total}$ are shown in Figure 5. The curve in N_2 (Figure 5(a)) was calculated with [e^-–h^+]$_0$ = 1, k_1 = 0.01, and k_2 = k_3 = 0 while that in O_2 was done by changing k_2 to 0.001. Figure 5 tells that the decay is decelerated in the presence of O_2 (Figure 5(b)). The same result can be obtained for MeOH by setting k_3 to 0.001 instead of k_2. Thus, the absorbance by a mixture of electrons and holes can be increased by either an electron- or hole-consuming reaction, supporting the attribution of the absorbance at 22000

cm^{-1} to the mixture of electrons and holes. The larger contribution of electrons to the absorbance at 13000 cm^{-1} than that at 22000 cm^{-1} can also be supported by the simulation, where $[e^-, h^+]_{total}$ with larger contribution of electrons was calculated as: $[e^-, h^+]_{total} = 2[e^-–h^+] + 0.5[h^+_s] + 1.5[e^-_s]$ (Figure 5(c)). The increase by O_2 becomes smaller by increasing the contribution of electrons. Therefore, the smaller increase by O_2 of the absorbance at 13000 cm^{-1} indicates larger contribution of electrons than that at 22000 cm^{-1}.

These results confirmed that the absorbance at each wavenumber reflects the number of carriers in different energy states: 2000 cm^{-1} for free electrons, 22000 cm^{-1} for trapped electrons and holes, and 13000 cm^{-1} for trapped electrons and holes but with a larger contribution of trapped electrons except ST-01_600C. In ST-01_600C, the contribution of trapped electrons to the absorbance at 13000 cm^{-1} seems smaller than that in other samples.

$$e^-–h^+ \rightarrow h\nu \text{ and/or } \Delta \qquad r_1 = k_1[e^-–h^+] \qquad (1)$$

$$e^-–h^+ + O_2 \rightarrow h^-_s + O_2^- \qquad r_2 = k_2[O_2][e^-–h^+] \qquad (2)$$

$$e^-–h^+ + MeO^- \rightarrow e^-_s + MeO^\bullet \qquad r_3 = k_3[MeO^-][e^-–h^+] \qquad (3)$$

$$\frac{d[e^- - h^+]}{dt} = -(k_1 + k_2' + k_3')[e^- - h^+] \qquad (4)$$

$$\frac{d[h_s^+]}{dt} = k_2'[e^- - h^+] \qquad (5)$$

$$\frac{d[e_s^-]}{dt} = k_3'[e^- - h^+] \qquad (6)$$

$$[e^- - h^+] = [e^- - h^+]_0 e^{-(k_1+k_2'+k_3')t} \qquad (7)$$

$$[h_s^+] = \frac{[e^- - h^+]_0 k_2'}{k_1 + k_2' + k_3'}\left(1 - e^{-(k_1+k_2'+k_3')t}\right) \qquad (8)$$

$$[e_s^-] = \frac{[e^- - h^+]_0 k_3'}{k_1 + k_2' + k_3'}\left(1 - e^{-(k_1+k_2'+k_3')t}\right) \qquad (9)$$

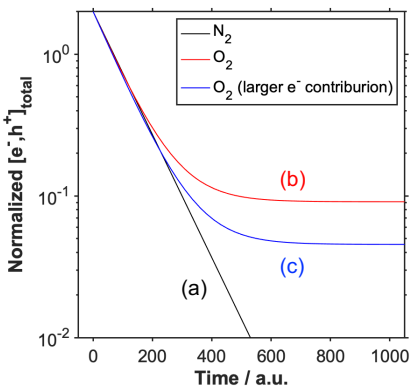

Figure 5 Simulated transient decay curves of electrons and holes. The curves in N_2 (a), O_2 (b), and O_2 with larger contribution of electrons to the absorbance (c).

Next, we compared the decay curves of these different carriers among the samples (Figure 6). Normalized absorbance at 22000 cm^{-1} (Figure 6A) was larger in the order ST-01_600C < ST-01 < ST-01_300C after 1000 ps. This agrees well with the trend in the microsecond region (Figure 6B), where the absorbance increased in the order ST-01_600C < ST-01 < ST-01_300C. The similar trend was observed in 13000 cm^{-1} (Figure 6C, D). In contrast, the decay of 2000 cm^{-1} (Figure 6E) is different from those of 22000 and 1300 cm^{-1}; the decay was fastest in ST-01, followed in order by ST-01_300C and ST-01_600C. This order was consistent with that in the microsecond region (Figure 6F). These observations suggest that the energy states of photoexcited carriers in the microsecond region was determined by carrier dynamics in the picosecond region.

In addition, we observed a rapid decay of free electrons up to 10 ps in ST-01_300C (Figure 7(b)), which has the largest amount of the trapped carriers. The rapid decay was not some artifacts but also observed in another sample calcined at 300 ºC for 12 h (Figure 7(d)). Thus, the rapid decay is seemingly caused by low-temperature calcination such as 300 ºC. Although the reason has not been disclosed yet, it would be due to the presence of coagulated particles consisting of anatase and amorphous TiO_2, caused by low-temperature calcination such as 300 ºC, in which rapid trapping of free electrons from anatase to amorphous phase takes place. Generally, powder TiO_2 samples contain a small amount of amorphous content around 10%.[41,42] This amorphous content would be partially crystallized by calcination at 300 ºC, which is lower than the crystallization temperature of amorphous to anatase TiO_2 (450 ºC),[43] to form the coagulated particles, although they cannot be observed in the TEM image (Figure 2B) due to the strong aggregation of the particles. As will be discussed later, the rapid decay well corresponded to the increase of the trapped carriers, which would explain the large number of trapped carriers in this sample.

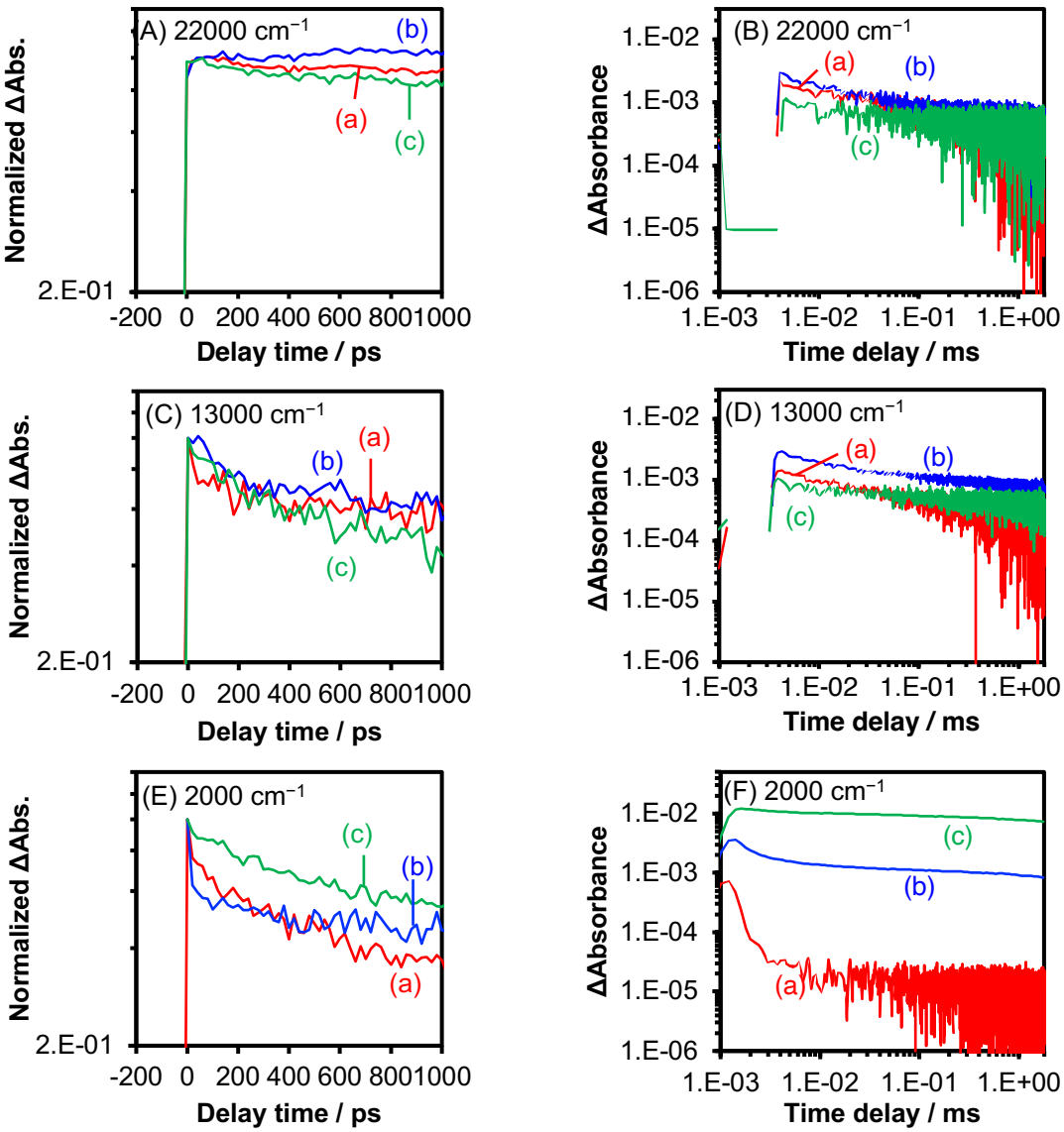

Figure 6 Decay curves of transient absorption by anatase TiO_2 samples irradiated by UV laser pulses probed at 22000 (A, B), 13000 (C, D), and 2000 cm^{-1} (E, F). (a), (b), and (c) are ST-01, ST-01_300C, and ST-01_600C, respectively.

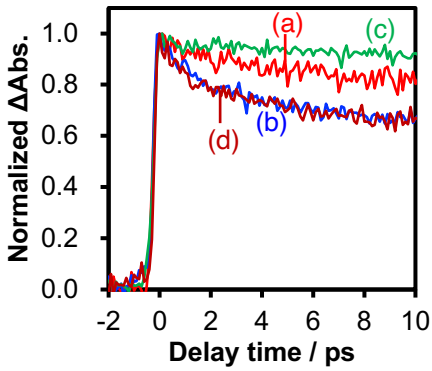

Figure 7. Transient decays of free electrons in the early time region probed at 2000 cm^{-1}. (a), (b), (c), and (d) are ST-01, ST-01_300C, ST-01_600C, and ST-01_300C_12h, respectively.

The difference in dynamics of photoexcited carriers was also obvious in their trapping processes, which can be discussed by comparing the normalized absorbances of different wavenumbers (Figure 8). In ST-01, the absorbance at 2000 cm^{-1} immediately reached its maximum within 0.1 ps and started to decrease while that at 13000 cm^{-1} kept increasing until it reaches its maximum at 0.8 ps (Figure 8A, inset). The correspondence between the decrease of 2000 cm^{-1} and the increase of 13000 cm^{-1} indicates that trapped electrons are produced by trapping of free electrons within few picoseconds, although the decrease of free electrons (2000 cm^{-1}) was much smaller than that in rutile due to the long lifetime of free electrons in anatase TiO_2.[13] Thus, the decrease in the free electrons after 0.1 ps would contain the trapping of free electrons. The difference between 2000 cm^{-1} and 13000 cm^{-1} became obvious after 60 ps (Figure 8A); the decay of 13000 cm^{-1} was slower than that at 2000 cm^{-1}. The absorbance at 22000 cm^{-1} increased until 10 ps, which would reflect the accumulation of electrons into deeper states with time. As a result, the decay became slower in the order 2000, 13000, and 22000 cm^{-1} (Figure 8A). This indicates that carrier recombination or transfer to other energy states becomes difficult as the energy level of the carriers becomes deeper. A similar trend was observed in ST-01_300C (Figure 8B). This suggests rapid trapping of free electrons to produce trapped electrons and would explain the large number of trapped carriers in this sample. In ST-01_600C (Figure 8C), the absorbances at the three wavenumbers were almost identical until 10 ps (Figure 8C, inset). Especially, the decay of 2000 cm^{-1} was slower than that in the other two samples (Figure 7). Since this sample has a small amount of surface defects due to its small SSA, the electron trapping at the surface defects would be slower than other samples. Thus, more free electrons survive without being trapped. Therefore, the number of trapped carriers becomes the smallest among three samples. These results suggested that carrier trapping dynamics depends on SSA of the sample, leading to different energy states in the microsecond region.

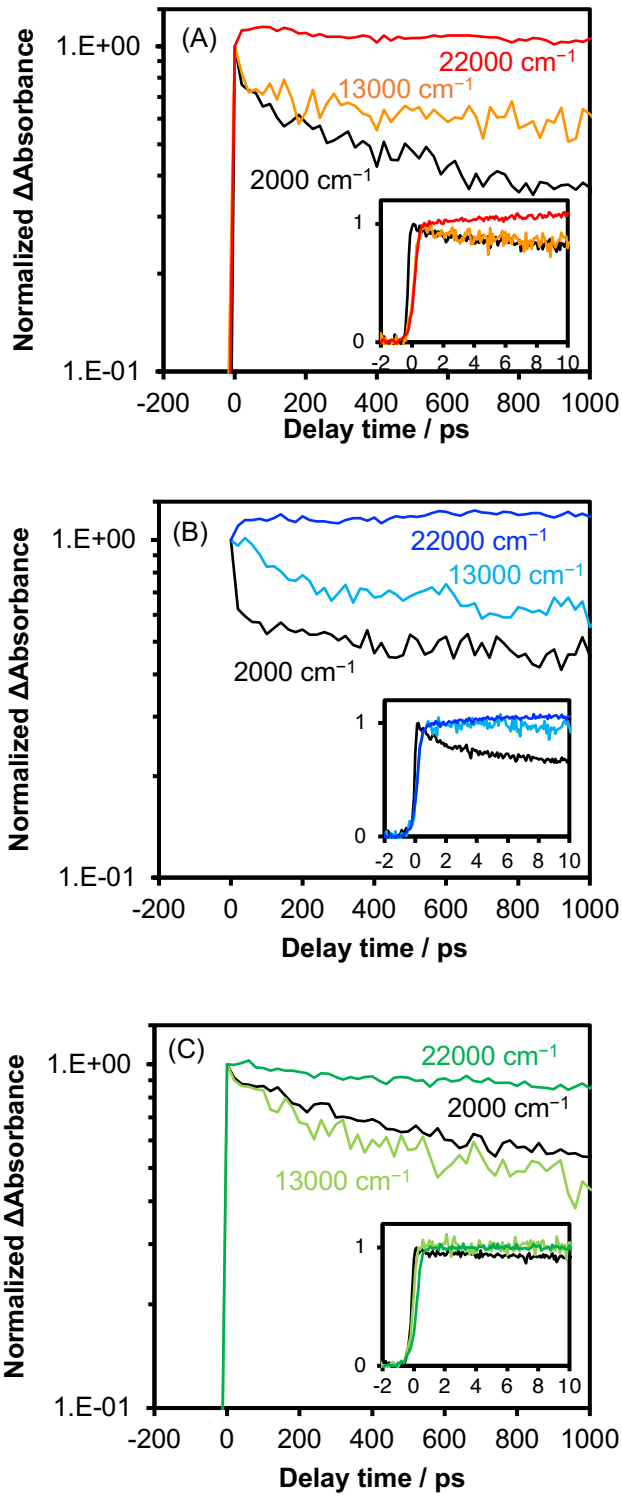

Figure 8 Normalized transient decays of electrons and holes in ST-01 (A), ST-01_300C (B), and ST-01_600C (C) probed at 2000, 13000, and 22000 cm^{-1} in 20 Torr of N_2.

Trapping of Charge Carriers in Anatase TiO_2

Behavior of photoexcited carriers in anatase TiO_2 nanoparticles has been studied well both experimentally and theoretically. Electron paramagnetic resonance (EPR),[44] FT-IR,[45,46] and photoluminescence (PL)[47,48] showed that free electrons are the dominant carrier in anatase TiO_2. Theoretical calculations also supported that the depths of the electron trap in anatase TiO_2 are much shallower than that in rutile TiO_2,[49,50] which allows the delocalization of electrons with conduction-band-like transport.[51] These studies employed anatase samples with relatively small SSA such as 50 to 130 $m^2\ g^{-1}$ or consider only the bulk properties of anatase TiO_2. Our observation is partially consistent with these results; most electrons exist as free electrons in the sample with small SSA (ST-01_600C, 50 $m^2\ g^{-1}$). In contrast, we found that they exist as trapped electrons in the sample with large SSA (ST-01, 300 $m^2\ g^{-1}$), which is probably due to the large number of electron traps located near the surface. The trap sites are generally regarded as crystallite defects such as Ti atoms at the oxygen vacancies and Ti interstitials. As for the surface traps, under-coordinated Ti atoms and Ti atoms nearby bridging hydroxyl groups have been proposed as possible trap sites.[52,53] The trapping depth were calculated as 1.2 eV for penta-coordinated Ti atoms and 1.6 eV for hexa-coordinated Ti atoms between two briging hydroxyl groups, for example. Although the accurate determination of the depth from the absorption band is difficult due to its broadness, the calculated trap depths of these trap sites are within the absorption range of trapped electrons (> 0.7 eV), implying their contributions as the trap sites. Free electrons, which are dominant carrier in anatase TiO_2 with small SSA (Figure 9A), tend to be captured by these surface traps as the SSA increases (Figure 9B), making trapped electrons dominant carrier at large SSA (Figure 9C).

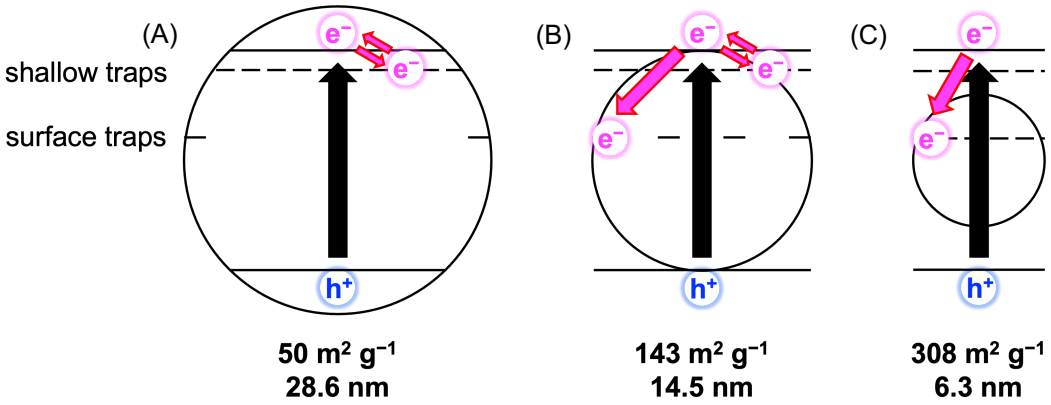

Figure 9 Schematic illustration of behavior of photoexcited carriers in anatase TiO_2 nanoparticles with different SSA and particle size. (A), (B), and (C) are ST-01_600C, ST-01_300C, and ST-01, respectively. As the increase of SSA, the density of the defects increases.

Conclusion

We found that the energy states of various anatase TiO_2 nanoparticles depend on SSA of the samples. Most electrons exist as trapped electrons when SSA is large while they survive as free electrons when SSA is small, and both free and trapped electrons exist when SSA is moderate. These different energy states in the microsecond region are determined by carrier dynamics in the picosecond region. The lifetime of free electrons is increased with decreasing SSA while that of trapped carriers is affected by other factors such as the presence of anatase–amorphous particles. Although SSA of photocatalysts is usually considered as a factor of the number of adsorption sites for reactants, this study proposed another aspect of SSA: a factor to change the energy states of photoexcited carriers. We anticipate that our essay contributes to a better understanding of the structure-property-activity relationship in TiO_2 photocatalysts and thus to the development of highly efficient TiO_2-based photocatalysts.

References

1. Kudo, A. & Miseki, Y. Heterogeneous photocatalyst materials for water splitting. *Chem. Soc. Rev.* **38**, 253–278 (2009).
2. Takanabe, K. Photocatalytic Water Splitting: Quantitative Approaches toward Photocatalyst by Design. *ACS Catal.* **7**, 8006–8022 (2017).
3. Ni, M., Leung, M. K. H., Leung, D. Y. C. & Sumathy, K. A review and recent developments in photocatalytic water-splitting using TiO_2 for hydrogen production. *Renew. Sustain. Energy Rev.* **11**, 401–425 (2007).
4. Gaya, U. I. & Abdullah, A. H. Heterogeneous photocatalytic degradation of organic contaminants over titanium dioxide: A review of fundamentals, progress and problems. *J. Photochem. Photobiol. C Photochem. Rev.* **9**, 1–12 (2008).
5. Rauf, M. A. & Ashraf, S. S. Fundamental principles and application of heterogeneous photocatalytic degradation of dyes in solution. *Chem. Eng. J.* **151**, 10–18 (2009).
6. Konstantinou, I. K. & Albanis, T. A. TiO_2-assisted photocatalytic degradation of azo dyes in aqueous solution: Kinetic and mechanistic investigations: A review. *Appl. Catal. B Environ.* **49**, 1–14 (2004).
7. Dong, H. *et al.* An overview on limitations of TiO_2-based particles for photocatalytic degradation of organic pollutants and the corresponding countermeasures. *Water Res.* **79**, 128–146 (2015).
8. Devi, L. G. & Kavitha, R. A review on non metal ion doped titania for the photocatalytic degradation of organic pollutants under UV/solar light: Role of photogenerated charge carrier dynamics in enhancing the activity. *Appl. Catal. B Environ.* **140**–**141**, 559–587

(2013).
9. Ma, Y. *et al.* Titanium dioxide-based nanomaterials for photocatalytic fuel generations. *Chem. Rev.* **114**, 9987–10043 (2014).
10. Fujishima, A., Zhang, X. & Tryk, D. A. TiO_2 photocatalysis and related surface phenomena. *Surf. Sci. Rep.* **63**, 515–582 (2008).
11. Schneider, J. *et al.* Understanding TiO_2 photocatalysis: Mechanisms and materials. *Chem. Rev.* **114**, 9919–9986 (2014).
12. Yamakata, A., Vequizo, J. J. M. & Matsunaga, H. Distinctive Behavior of Photogenerated Electrons and Holes in Anatase and Rutile TiO_2 Powders. *J. Phys. Chem. C* **119**, 24538–24545 (2015).
13. Yamakata, A. & Vequizo, J. J. M. Curious behaviors of photogenerated electrons and holes at the defects on anatase, rutile, and brookite TiO_2 powders: A review. *J. Photochem. Photobiol. C Photochem. Rev.* **40**, 234–243 (2019).
14. Tanaka, K., Capule, M. F. V. & Hisanaga, T. Effect of crystallinity of TiO_2 on its photocatalytic action. *Chem. Phys. Lett.* **187**, 73–76 (1991).
15. Ohno, T., Haga, D., Fujihara, K., Kaizaki, K. & Matsumura, M. Unique effects of iron(III) ions on photocatalytic and photoelectrochemical properties of titanium dioxide. *J. Phys. Chem. B* **101**, 6415–6419 (1997).
16. Ohno, T., Sarukawa, K. & Matsumura, M. Photocatalytic Activities of Pure Rutile Particles Isolated from TiO₂ Powder by Dissolving the Anatase Component in HF Solution. *J. Phys. Chem. B* **105**, 2417–2420 (2001).
17. Abe, R., Sayama, K., Domen, K. & Arakawa, H. A new type of water splitting system composed of two different TiO_2 photocatalysts (anatase, rutile) and a IO_3^-/I^- shuttle redox mediator. *Chem. Phys. Lett.* **344**, 339–344 (2001).
18. Maeda, K. Direct splitting of pure water into hydrogen and oxygen using rutile titania powder as a photocatalyst. *Chem. Commun.* **49**, 8404–8406 (2013).
19. Ohtani, B., Handa, J., Nishimoto, S. & Kagiya, T. Highly active semiconductor photocatalyst: Extra-fine crystallite of brookite TiO_2 for redox reaction in aqueous propan-2-ol and / or silver sulfate solution. *Chem. Phys. Lett.* **120**, 292–294 (1985).
20. Kandiel, T. A., Feldhoff, A., Robben, L., Dillert, R. & Bahnemann, D. W. Tailored titanium dioxide nanomaterials: anatase nanoparticles and brookite nanorods as highly active photocatalysts. *Chem. Mater.* **22**, 2050–2060 (2010).
21. Ohno, T. *et al.* Dependence of photocatalytic activity on aspect ratio of a brookite TiO_2 nanorod and drastic improvement in visible light responsibility of a brookite TiO_2 nanorod by site-selective modification of Fe^{3+} on exposed faces. *J. Mol. Catal. A Chem.* **396**, 261–267 (2015).
22. Colbeau-Justin, C., Kunst, M. & Huguenin, D. Structural influence on charge-carrier lifetimes in TiO_2 powders studied by microwave absorption. *J. Mater. Sci.* **38**, 2429–

2437 (2003).
23. Rothenberger, G., Moser, J., Gratzel, M., Serpone, N. & Sharma, D. K. Charge carrier trapping and recombination dynamics in small semiconductor particles. *J. Am. Chem. Soc.* **107**, 8054–8059 (1985).
24. Schindler, K. M. & Kunst, M. Charge-carrier dynamics in TiO_2 powders. *J. Phys. Chem.* **94**, 8222–8226 (1990).
25. Warman, J. M. *et al.* Electronic processes in semiconductor materials studied by nanosecond time-resolved microwave conductivity-III. Al_2O_3, MgO and TiO_2 powders. *Int. J. Radiat. Appl. Instrumentation. Part* **37**, 433–442 (1991).
26. Martin, S. T., Herrmann, H., Choi, W. & Hoffmann, M. R. Time-resolved microwave conductivity Part 1.-TiO_2 Photoreactivity and Size Quantization. *J. Chem. Soc. - Faraday Trans.* **90**, 3315–3322 (1994).
27. Serpone, N., Lawless, D., Khairutdinov, R. & Pelizzetti, E. Subnanosecond relaxation dynamics in TiO_2 colloidal sols (particle sizes R_p = 1.0-13.4 nm). Relevance to heterogeneous photocatalysis. *J. Phys. Chem.* **99**, 16655–16661 (1995).
28. Furube, A., Asahi, T., Masuhara, H., Yamashita, H. & Anpo, M. Femtosecond diffuse reflectance spectroscopy on some standard TiO_2 powder catalysts. *Chemistry Letters* 735–736 (1997) doi:10.1246/cl.1997.735.
29. Yamakata, A., Ishibashi, T. A. & Onishi, H. Time-resolved infrared absorption spectroscopy of photogenerated electrons in platinized TiO_2 particles. *Chem. Phys. Lett.* **333**, 271–277 (2001).
30. Yamakata, A., Ishibashi, T. A. & Onishi, H. Water- and oxygen-induced decay kinetics of photogenerated electrons in TiO_2 and Pt/TiO_2: A time-resolved infrared absorption study. *J. Phys. Chem. B* **105**, 7258–7262 (2001).
31. Yamakata, A., Ishibashi, T. A. & Onishi, H. Electron- and hole-capture reactions on Pt/TiO_2 photocatalyst exposed to methanol vapor studied with time-resolved infrared absorption spectroscopy. *J. Phys. Chem. B* **106**, 9122–9125 (2002).
32. Yamakata, A., Ishibashi, T. A. & Onishi, H. Effects of Water Addition on the Methanol Oxidation on Pt/TiO_2 Photocatalyst Studied by Time-Resolved Infrared Absorption Spectroscopy. *J. Phys. Chem. B* **107**, 9820–9823 (2003).
33. Heimer, T. A. & Heilweil, E. J. Direct time-resolved infrared measurement of electron injection in dye-sensitized titanium dioxide films. *J. Phys. Chem. B* **101**, 10990–10993 (1997).
34. Yamakata, A., Ishibashi, T. A. & Onishi, H. Microsecond kinetics of photocatalytic oxidation on Pt/TiO_2 traced by vibrational spectroscopy. *Chem. Phys. Lett.* **376**, 576–580 (2003).
35. Bahnemann, D., Henglein, A., Lilie, J. & Spanhel, L. Flash photolysis observation of the absorption spectra of trapped positive holes and electrons in colloidal TiO_2. *J. Phys.*

Chem. **88**, 709–711 (1984).

36. Bahnemann, D. W., Hilgendorff, M. & Memming, R. Charge carrier dynamics at TiO_2 particles: Reactivity of free and trapped holes. *J. Phys. Chem. B* **101**, 4265–4275 (1997).
37. Yoshihara, T. *et al.* Identification of Reactive Species in Photoexcited Nanocrystalline TiO_2 Films by Wide-Wavelength-Range (400-2500 nm) Transient Absorption Spectroscopy. *J. Phys. Chem. B* **108**, 3817–3823 (2004).
38. Tamaki, Y. *et al.* Direct observation of reactive trapped holes in TiO_2 undergoing photocatalytic oxidation of adsorbed alcohols: Evaluation of the reaction rates and yields. *J. Am. Chem. Soc.* **128**, 416–417 (2006).
39. Wang, X. *et al.* Transient absorption spectroscopy of anatase and rutile: The impact of morphology and phase on photocatalytic activity. *J. Phys. Chem. C* **119**, 10439–10447 (2015).
40. Yamakata, A. *et al.* Morphology-sensitive trapping states of photogenerated charge carriers on $SrTiO_3$ particles studied by time-resolved visible to Mid-IR absorption spectroscopy: The effects of molten salt flux treatments. *J. Photochem. Photobiol. A Chem.* **313**, 168–175 (2015).
41. Ohtani, B., Prieto-Mahaney, O. O., Li, D. & Abe, R. What is Degussa (Evonic) P25? Crystalline composition analysis, reconstruction from isolated pure particles and photocatalytic activity test. *J. Photochem. Photobiol. A Chem.* **216**, 179–182 (2010).
42. Zielińska-jurek, A., Wei, Z., Janczarek, M., Wysocka, I. & Kowalska, E. Size-controlled synthesis of Pt particles on TiO_2 surface: Physicochemical characteristic and photocatalytic activity. *Catalysts* **9**, 940 (2019).
43. Ohtani, B., Ogawa, Y. & Nishimoto, S. Photocatalytic Activity of Amorphous - Anatase Mixture of Titanium (IV) Oxide Particles Suspended in Aqueous Solutions. *J. Phys. Chem. B* **101**, 3746–3752 (1997).
44. Berger, T. *et al.* Light-induced charge separation in anatase TiO_2 particles. *J. Phys. Chem. B* **109**, 6061–6068 (2005).
45. Szczepankiewicz, S. H., Moss, J. A. & Hoffmann, M. R. Slow surface charge trapping kinetics on irradiated TiO_2. *J. Phys. Chem. B* **106**, 2922–2927 (2002).
46. Litke, A., Hensen, E. J. M. & Hofmann, J. P. Role of Dissociatively Adsorbed Water on the Formation of Shallow Trapped Electrons in TiO_2 Photocatalysts. *J. Phys. Chem. C* **121**, 10153–10162 (2017).
47. Vequizo, J. J. M., Kamimura, S., Ohno, T. & Yamakata, A. Oxygen induced enhancement of NIR emission in brookite TiO_2 powders: Comparison with rutile and anatase TiO_2 powders. *Phys. Chem. Chem. Phys.* **20**, 3241–3248 (2018).
48. Knorr, F. J., Mercado, C. C. & McHale, J. L. Trap-state distributions and carrier transport in pure and mixed-phase TiO_2: Influence of contacting solvent and interphasial electron transfer. *J. Phys. Chem. C* **112**, 12786–12794 (2008).

49. Mattioli, G., Filippone, F., Alippi, P. & Amore Bonapasta, A. Ab initio study of the electronic states induced by oxygen vacancies in rutile and anatase TiO2. *Phys. Rev. B* **78**, 241201-1-241201–4 (2008).
50. Mattioli, G., Alippi, P., Filippone, F., Caminiti, R. & Amore Bonapasta, A. Deep versus shallow behavior of intrinsic defects in rutile and anatase TiO_2 polymorphs. *J. Phys. Chem. C* **114**, 21694–21704 (2010).
51. Spreafico, C. & VandeVondele, J. The nature of excess electrons in anatase and rutile from hybrid DFT and RPA. *Phys. Chem. Chem. Phys.* **16**, 26144–26152 (2014).
52. Szczepankiewicz, S. H., Colussi, A. J. & Hoffmann, M. R. Infrared spectra of photoinduced species on hydroxylated titania surfaces. *J. Phys. Chem. B* **104**, 9842–9850 (2000).
53. Di Valentin, C., Pacchioni, G. & Selloni, A. Electronic structure of defect states in hydroxylated and reduced rutile TiO2(110) surfaces. *Phys. Rev. Lett.* **97**, 166803 (2006).

Chapter 5

A quantitative study on the relation of specific surface area and carrier lifetime to photocatalytic activity of anatase TiO_2 nanoparticles

Abstract

Photocatalysis is a multistep reaction of which efficiency is affected by various structural and physicochemical parameters. Understanding the relationship of these parameters and photocatalytic activity is important for the better design of photocatalysts. However, most studies lack a quantitative discussion on the contributions of multiple parameters, failing to elucidate their interdependency, which is essential to understand different effects of the parameters depending on the photocatalyst and reaction. In this study, we show that a statistical approach based on a simple kinetic model can elucidate a quantitative relation of photocatalytic activity, and specific surface area and carrier lifetime, both of which are decisive factors of photocatalytic activity. We carried out dehydrogenative homo-coupling of benzene using 21 anatase TiO_2 photocatalysts with different SSA as well as microsecond-time-resolved infrared absorption spectroscopy to estimate the lifetime of photoexcited carriers. We found that the activities of these photocatalysts can be explained by a simple kinetic model which has SSA and carrier lifetime as variables. The model quantitatively explains the interdependency between SSA and carrier lifetime; the effect of one parameter on the activity depends on another parameter. The present study provides a methodology to understand a quantitative relationship between multiple parameters and photocatalytic activity.

Introduction

Heterogeneous photocatalysis is a promising system for green chemical conversion using light energy. It can decompose pollutants under mild conditions and offer a unique synthetic route of organic molecules. Moreover, photocatalysis can promote endergonic reactions to achieve solar-to-chemical energy conversion. Because of these advantages, photocatalysis has now gained its importance in various fields such as environmental remediation,[1–4] transformations of organic molecules,[5–9] and artificial photosynthesis.[10–15] Photocatalysis is initiated by photoabsorption of the photocatalyst. Upon irradiation of light whose energy equals or exceeds the bandgap of the photocatalyst, electrons in the valance band are excited to the conduction band to leave holes. These photoexcited electrons and holes activate the reactant adsorbed on the surface of the photocatalyst and subsequent reactions of the activated reactant give the product. Because of this multistep reaction mechanism, the efficiency of photocatalysis is influenced by various structural and physicochemical parameters. Understanding the relationship between these parameters and photocatalytic activity is the key to designing efficient photocatalysts.

Among those affecting photocatalytic activity, specific surface area (SSA) and carrier lifetime are decisive parameters since the former correlates with the concentration of the adsorbed reactants and the latter does with that of the photoexcited carriers. Generally, a larger SSA or longer carrier lifetime improves photocatalytic activity.[16–24] However, such a clear correlation is not always observed. The effect of SSA can be non-linear or negligible,[16–18] or even larger[23] depending on the material, reaction, and the value of SSA. The effect of carrier lifetime also tends to be unclear especially in powder photocatalysts, which often have different properties other than carrier lifetime.[25]

These results show that photocatalytic activity cannot be explained by a single parameter even if the parameter is regarded as a decisive one such as SSA and carrier lifetime. Therefore, understanding the photocatalytic activity requires a multidimensional discussion, in which the effects of multiple parameters are discussed altogether. Such a multidimensional discussion is achieved by using a model equation to quantitatively evaluate the contributions of multiple parameters. However, their contributions are often evaluated in a qualitative manner, in which is the effect of each parameter is discussed individually, failing to give a comprehensive understanding of the photocatalytic activity. In this study, we employed a statistical approach based on a simple kinetic model to evaluate the quantitative relation of photocatalytic activity to SSA and carrier lifetime. We examined the activities of 21 different

anatase TiO_2 photocatalysts in dehydrogenative homo-coupling of benzene as a model reaction as well as the lifetime of photoexcited carriers by microsecond time-resolved infrared absorption spectroscopy. We found that their activities can be explained by a simple kinetic rate equation which has SSA and carrier lifetime as variables. The equation tells that the effect of SSA and carrier lifetime can be mathematically equal and quantitatively explains their interdependency, in which the effect of one parameter depends on another. Moreover, the product of SSA and carrier lifetime was proposed as a quantitative indicator to determine their effects on photocatalytic activity.

Experimental

Reaction tests

Materials. 21 different anatase TiO_2 powder samples were employed, which are supplied by Catalysis Society of Japan (TIO-2, 9, 13), Tayca (JA-1, AMT-400), Sigma Aldrich (SAJ first grade), Nacalai Tesque (Nacalai), Ishihara Sangyo Kaisha (ST-01, 21, 41), ACROS organics (ACROS), and Sakai Chemical (SSP-M, SSP-20). Some samples were prepared by calcination of ST-01 (308 $m^2\ g^{-1}$) at various temperatures and times, which are denoted as ST-01_300C_1h for example. If it is not mentioned, the calcination time is 24 h. Specific surface areas of the calcined samples were estimated by Brunauer-Emmett-Teller (BET) method and their crystal phase was confirmed as anatase phase by XRD.

Benzene (Nacalai Tesque, 99%) was dried by molecular sieve 4A before reaction to remove the water content in the solution.

Photocatalytic dehydrogenative homo-coupling of benzene. Dehydrogenative homo-coupling of benzene was performed in a 20 mL Pyrex tube under an argon atmosphere. The typical procedure of reaction tests is as follows. TiO_2 photocatalysts (80 mg) in the test tube sealed with a silicon septum were heated at 180 ºC for 20 min under argon flow to remove adsorbed water on the surface of the photocatalyst. Then, the dried benzene (5 mL) was introduced into the test tube, followed by purging with argon gas for 30 min. The test tube was irradiated by 4.5 W UV LED tapes under stirring for a desired time. After irradiation, 1 mL of the gaseous phase was taken from the tube using an air-tight syringe and analyzed by GC-TCD (Shimadzu, GC-8A). The liquid phase was sampled using a syringe with a PTFE filter to remove the photocatalyst and then analyzed. Products in the liquid phase were identified by GC-MS (Shimadzu, GCMS-QP2020) and quantified by GC-FID (GC-2014) using n-decane as

an internal standard. Formation rates of the products were calculated from slopes of the time course of the product yields.

Characterization and Statistical Analysis

Time-resolved infrared absorption spectroscopy. Time-resolved infrared absorption spectroscopy was carried out in 20 Torr of N_2 to estimate carrier lifetime. Microsecond-time resolved measurements were performed by the custom-built spectrometers. Probe light emitted from a $MoSi_2$ coil was focused on the sample, and the transmitted light was introduced to a grating spectrometer. The monochromated light was detected by an MCT detector (Kolmar), and the output electric signal was amplified with an ac-coupled amplifier (Stanford Research Systems, SR560, 1 MHz). In each experiment, a 355 nm UV pulse from an Nd:YAG laser (Continuum, Surelite I; duration 6 ns; power 0.5 mJ; repetition rate 5 or 0.5 Hz) was used to excite the band gap of the photocatalysts. The time resolution of the spectrometers was limited to 1−2 μs by the bandwidth of the amplifier. Each TiO_2 powder was fixed on a circular CaF_2 plate with a density of 3 mg cm^{-1} and placed in the closed IR cell. Picosecond time-resolved measurements were performed in the same system with the femtosecond measurements (Chapter 4) but with the third harmonic of a Nd:YVO_4 laser (InnoLas Laser, Picolo-1; 1 kHz repetition rate, 800 ps duration, 355 nm with 6 and 1 μJ pulse energy) as a pump. These two laser systems were temporarily synchronized, and the intervals between pump and probe pulses were controlled by a digital delay generator (Stanford Research Systems, DG535). The time resolution of the measurements was 800 ps.

Curve fitting and Non-linear regression analysis. Curve fitting of transient decay curves to estimate carrier lifetime and non-linear regression analysis on results of the reaction tests were performed by Curve Fitting Toolbox in MATLAB.

Results and Discussion

Photocatalytic dehydrogenative homo-coupling of benzene

The reaction proceeded to afford biphenyl (BPh) as a major product. BPh is probably formed through hole oxidation of benzene to produce a phenyl radical and subsequent coupling of two phenyl radicals (eqs. 1–3). The reaction also afforded 2-phenyl-1,4-cyclohexadiene and 3-phenyl-1,4-cyclohexadiene (the sum of them was denoted as PhCs) as byproducts. No hydrogen gas was detected. PhCs would be produced by successive hydrogenation of BPh (eqn. 4). The formation rates of BPh (r_{BPh}) and PhCs (r_{PhCs}) increased with increasing SSA (Figure 1A). Especially, r_{BPh} increased non-linearly with SSA. As a result, their total formation rate (r_{total}), which was calculated as a sum of their formation rates, also increased non-linearly with increasing SSA (Figure 1B). Furthermore, as will be discussed later, some samples deviated from the non-linear trend predicted from a model which considers only SSA as a variable (Figure 1B, dotted line). This indicates that other factors than SSA affect the activity.

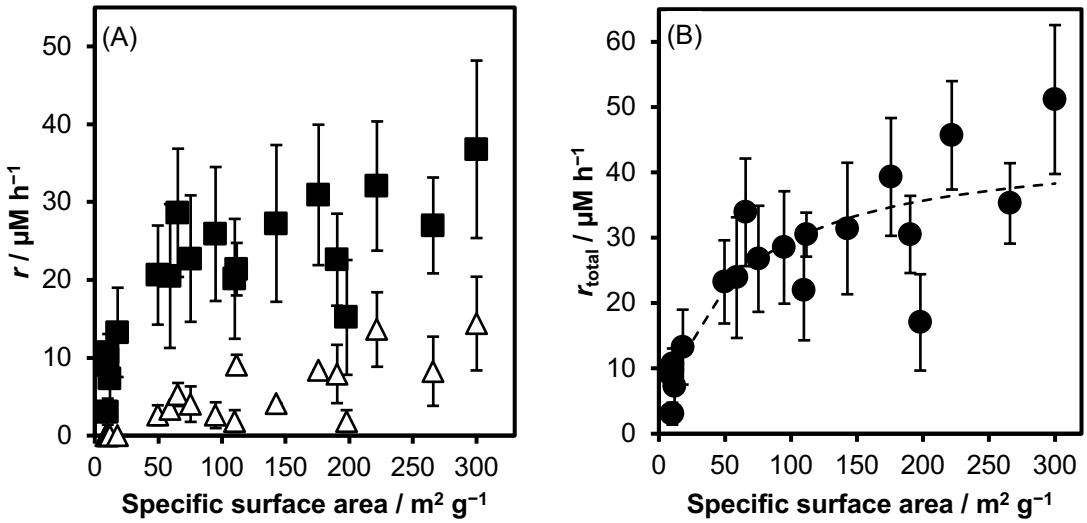

Figure 1. Relationship between specific surface area of anatase TiO_2 samples and (A) formation rate of biphenyl (BPh, ■) or phenylcyclohexadienes (PhCs, ◇) and (B) total formation rate of BPh and PhCs (r_{total}). Error bars represent 95% confidence intervals of the formation rate. A dotted line shows a predicted value from a model that considers only SSA as a variable (Table 3, entry 4).

$$TiO_2 \rightarrow e^- + h^+ \quad (1)$$

$$C_6H_6 + h^+ \rightarrow {}^{\bullet}C_6H_5 + H^+ \quad (2)$$

$$2\ {}^{\bullet}C_6H_5 \rightarrow C_6H_5\text{–}\ C_6H_5\ (BPh) \quad (3)$$

$$C_6H_5\text{–}\ C_6H_5 + 2\ e^- + 2\ H+ \rightarrow C_6H_5\text{–}C_6H_5\ (PhCs) \quad (4)$$

Transient absorption measurement

Generally, large SSA promotes surface recombination to decrease the lifetime of photoexcited carriers. Thus, the samples used in the present study are expected to have different carrier lifetimes. To estimate carrier lifetime, we carried out microsecond time-resolved absorption spectroscopy. In the present system, the homo-coupling of benzene (BPh) was obtained as the main product. BPh would be produced through the oxidation of benzene by photogenerated holes (eq. 2) and subsequent coupling of two phenyl radicals (eq. 3). Thus, a lifetime of holes would be important in this reaction. However, as discussed in Chapter 4, the absorption of holes in TiO_2 usually overlaps with that of deeply trapped electrons, making it difficult to estimate the lifetime of holes. Therefore, we measured the absorption of free electrons. Free electrons in TiO_2 give a monotonic absorption band below 4000 cm^{-1}. Figure 2 shows a representative decay curve of the absorption by free electrons. The absorption prolonged for more than one millisecond, which means that free electrons in this sample can survive in the millisecond region. Decay of the absorption is influenced by the presence of an organic molecule such as methanol (Chapter 4), indicating that the decay contains the recombination process with holes that are trapped on the surface of TiO_2 and can react with organic molecules. Thus, the decay of free electrons was used to estimate the lifetime of photogenerated holes which participate in the present reaction. The decay of the absorption was investigated for 21 samples and the obtained curves were fitted by three exponentials to calculate carrier lifetimes by assuming the first-order kinetics for the recombination process (Table 1). Each carrier lifetime ranges from 4 to 27 μs (τ_1, Figure 3A), 27 to 247 μs (τ_2, Figure 3B), and 2 to 9 ms (τ_3, Figure 3C). As a general trend, these carrier lifetimes decreased with increasing SSA. Some samples deviated from the trend, suggesting that carrier lifetime can be affected by other factors than SSA such as the impurity of the sample. These results evidenced carrier lifetimes are different depending on the sample and these carrier lifetimes, as well as SSA, should affect the activity.

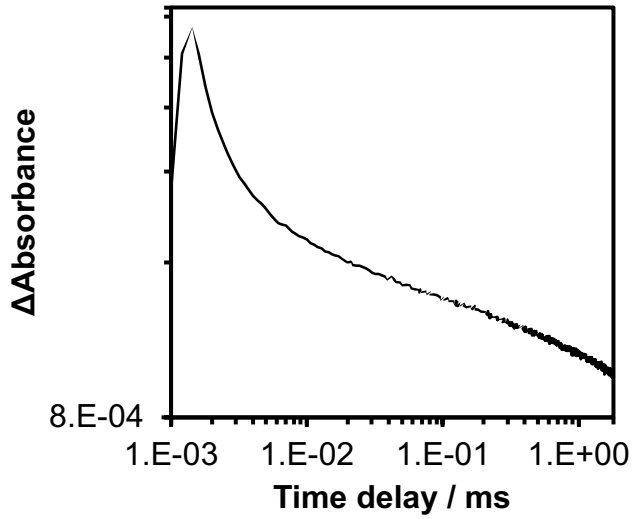

Figure 2. A representative decay curves of transient absorption by photoexcited free electrons in an anatase TiO_2 sample (ST-01_300C) in 20 Torr of N_2.

Table 1. Results of multi-exponential curve fit of decay curves of transient absorption by free electrons in anatase TiO_2 photocatalysts[a]

Entry	Sample	SSA / $m^2\ g^{-1}$	R^{2b}	Carrier lifetime[c]					
				τ_1 / ms (%)		τ_2 / ms (%)		τ_3 / ms (%)	
1	JA-1	9.0	0.955	0.016	(34.5)	0.14	(19.7)	6.4	(45.7)
2	SA 1st	9.2	0.938	0.025	(36.3)	0.25	(21.4)	6.0	(42.3)
3	Nacalai	10.2	0.988	0.014	(31.5)	0.13	(24.1)	4.7	(44.4)
4	ST-41	10.2	0.973	0.012	(15.7)	0.13	(12.5)	7.6	(71.8)
5	Wako_a	10.5	0.967	0.016	(25.9)	0.18	(16.4)	7.5	(57.7)
6	ACROS	11.9	0.958	0.017	(27.9)	0.19	(19.4)	7.1	(52.7)
7	TIO-2	18.0	0.980	0.011	(26.1)	0.12	(14.1)	8.0	(59.9)
8	TIO-13	59.0	0.993	0.022	(17.8)	0.20	(12.4)	9.5	(69.8)
9	ST-21	65.5	0.990	0.027	(16.7)	0.23	(15.5)	7.6	(67.8)
10	SSP-M	95.0	0.939	0.009	(43.1)	0.08	(21.4)	3.9	(35.5)
11	AMT-400	110.0	0.986	0.017	(32.4)	0.16	(19.7)	5.8	(48.0)
12	SSP-20	197.9	0.246	0.004	(57.0)	0.03	(33.0)	2.0	(10.0)
13	TIO-9	300.0	0.198	0.004	(73.5)	0.07	(9.8)	5.2	(16.7)
14	ST-01_600C	49.5	0.999	0.017	(64.6)	0.21	(12.2)	9.2	(23.2)
15	ST-01_500C	75.3	0.998	0.015	(63.2)	0.21	(13.2)	7.4	(23.6)
16	ST-01_400C	111.6	0.997	0.012	(38.8)	0.19	(17.1)	4.4	(44.1)
17	ST-01_300C	142.7	0.995	0.012	(38.1)	0.19	(15.6)	4.6	(46.3)
18	ST-01_300C_12h	175.8	0.989	0.013	(31.8)	0.18	(17.5)	3.5	(50.7)
19	ST-01_300C_4h	190.4	0.955	0.009	(20.8)	0.12	(16.8)	3.6	(62.3)
20	ST-01_300C_1h	221.9	0.929	0.010	(11.1)	0.14	(13.0)	2.9	(75.9)
21	ST-01_300C_15min	265.9	0.657	0.003	(5.5)	0.03	(10.7)	2.1	(83.7)

[a] The fitting was performed by Curve Fitting Toolbox in MATLAB. [b] Coefficient of determination. [c] Carrier lifetimes were estimated by multi-exponential curve fit. The values in parentheses are the contribution of the component.

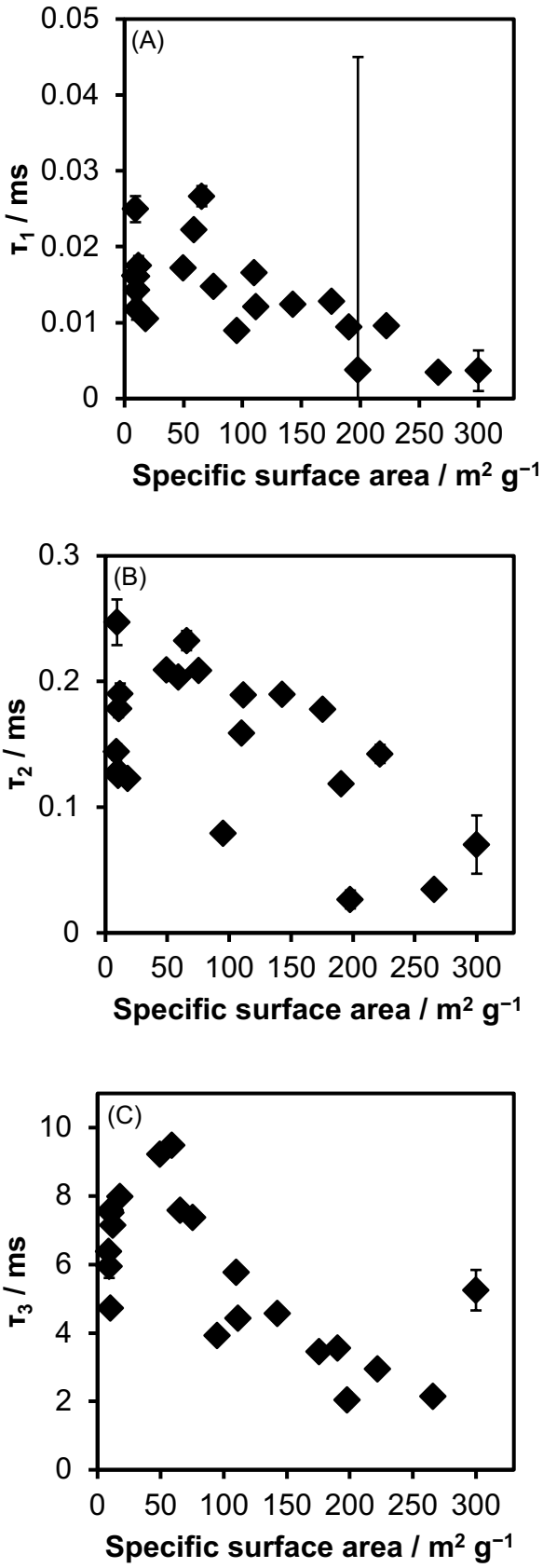

Figure 3. Relationship between specific surface area of anatase TiO_2 samples and lifetimes of photoexcited free electrons (τ_1, τ_2, τ_3) estimated by multi-exponential curve fit of transient decay curves. Error bars are 95% confidence intervals.

Non-linear fit based on a kinetic model

The results of the reaction tests and estimated carrier lifetime were summarized in Table 2. To discuss how SSA and carrier lifetime affect the activity, a simple kinetic model was employed. The model considers only three primary steps in photocatalysis. The first step (eq. 5) is photoabsorption of the photocatalyst to produce the excited reactive sites. The rate of this step is given by $r_1 = \varphi I$, where φ and I are the intrinsic quantum yield and photon flux (μM h^{-1}), respectively. φ corresponds to an efficiency of photoabsorption of anatase TiO_2 to produce photoexcited carriers. The second step (eq. 6) accounts for the recombination process of the carriers of which rate is given by $r_2 = [c_R^*] / \tau$, where $[c_R^*]$ and τ are the concentration of the excited reactive sites and carrier lifetime, respectively. Here, the first-order kinetics is assumed for the recombination process. The third step (eq. 7) is charge transfer from the excited reactive sites to the adsorbed substrate. The rate of this step ($r_3 = k[c_R^*][S]$) corresponds to the overall reaction rate; k and [S] are rate constant of the charge transfer and the concentration of the adsorbed substrate, respectively. Importantly, the present kinetic model considers only the half-reaction (hole oxidation or electron reduction) as the rate-determining step. Similar models are employed in some papers.[26,27] Since the reaction was carried out with neat benzene and sufficiently low light intensity (1.4 mW cm^{-1}), adsorption of benzene would be kept saturated during the reaction. Thus, the concentration of the adsorbed substrate [S] can be assumed as a constant, given as a saturated concentration $s_{sat} = \alpha$•SSA (α is the saturated concentration of adsorbed substrate per unit of specific surface area (μM g m^{-2})). By solving a differential equation for the concentration of the excited reactive sites $[c_R^*]$, the reaction rate r_3 is expressed by eq. 8. Further, by assuming that carrier lifetime τ is so low that the exponential term ($e^{-\left(\frac{1}{\tau}+ks_{sat}\right)t}$) is sufficiently smaller than 1: $1 \gg e^{-\left(\frac{1}{\tau}+ks_{sat}\right)t}$, r_3 can be simplified into eq. 9, which corresponds to the overall reaction rate r. In this equation, k, α, and φ can be considered as constants since all the photocatalysts used in this study were anatase TiO_2. Thus, r is a function of SSA and τ. Non-linear regression analysis was subsequently carried out on the results shown in Table 2 with this model equation using SSA and one of the carrier lifetimes as variables. The fitting results were shown in Table 3. The best result was obtained with the longest carrier lifetime τ_3 (Table 3, entry 1) with the coefficient of determination (R^2) of 0.84, showing that the model reproduces the experimental results well (Figure 4). The exponential term ($e^{-\left(\frac{1}{\tau}+k\alpha SSA\right)t}$) was found to be sufficiently smaller than 1 when it was calculated from

the fitting parameter $k\alpha$ = 4507 (g m^{-2} h^{-1}), proving that the result of the fitting is consistent with the assumption. Moreover, the adjusted R^2 of the two-variable fit (SSA and τ_3, Table 3, entry 1) was larger than that of single variable fits (SSA or τ_3, Table 3, entries 4 or 5). This means that the use of the two variables increases the predictive accuracy of the model. Thus, both SSA and carrier lifetime are necessary to explain the activity of the TiO_2 photocatalysts.

Table 2. Observed formation rates of the products in direct homo-coupling of benzene, specific surface area (SSA), and lifetimes of free electrons estimated by transient absorption measurements.

Entry	Sample	Formation rates[a] / μM h^{-1}			SSA[b] / m^2 g^{-1}	Carrier lifetimes[c]		
		r_{BPh}	r_{CHBs}	r_{sum}		τ_1 / ms	τ_2 / ms	τ_3 / ms
1	JA-1	9.0	0.0	9.0	9.0	0.016	0.14	6.4
2	SA 1st	3.1	0.0	3.1	9.2	0.025	0.25	6.0
3	Nacalai	3.1	0.0	3.1	10.2	0.014	0.13	4.7
4	ST-41	9.9	0.0	9.9	10.2	0.012	0.13	7.6
5	Wako_a	10.7	0.0	10.7	10.5	0.016	0.18	7.5
6	ACROS	7.3	0.0	7.3	11.9	0.017	0.19	7.1
7	TIO-2	13.3	0.0	13.3	18.0	0.011	0.12	8.0
8	TIO-13	20.5	3.4	23.9	59.0	0.022	0.20	9.5
9	ST-21	28.6	5.3	33.9	65.5	0.027	0.23	7.6
10	SSP-M	25.9	2.6	28.5	95.0	0.009	0.08	3.9
11	AMT-400	20.1	1.9	22.0	110.0	0.017	0.16	5.8
12	SSP-20	15.2	1.9	17.0	197.9	0.004	0.03	2.0
13	TIO-9	36.8	14.4	51.2	300.0	0.004	0.07	5.2
14	ST-01_600C	20.6	2.6	23.2	49.5	0.017	0.21	9.2
15	ST-01_500C	22.7	4.0	26.8	75.3	0.015	0.21	7.4
16	ST-01_400C	21.4	9.1	30.5	111.6	0.012	0.19	4.4
17	ST-01_300C	27.3	4.2	31.4	142.7	0.012	0.19	4.6
18	ST-01_300C_12h	30.9	8.4	39.3	175.8	0.013	0.18	3.5
19	ST-01_300C_4h	22.6	7.9	30.5	190.4	0.009	0.12	3.6
20	ST-01_300C_1h	32.1	13.6	45.7	221.9	0.010	0.14	2.9
21	ST-01_300C_15min	27.0	8.3	35.3	265.9	0.003	0.03	2.1

[a] Formation rate of the products in direct homo-coupling of benzene calculated from slopes of the time course of the product yield. r_{BPh}, r_{CHBs}, and r_{sum} are the formation rate of biphenyl (BPh), phenylcyclohexadiene (PhCs), and a sum of them, respectively. [b] Specific surface area. [c] Lifetime of free electrons estimated by transient absorption measurements probed at 2000 cm^{-1}.

$$c_R \rightarrow c_R^* \qquad r_1 = \varphi I \qquad (5)$$

$$c_R^* \rightarrow c_R \qquad r_2 = [c_R^*]/\tau \qquad (6)$$

$$c_R^* + S \rightarrow c_R + P \qquad r_3 = k[c_R^*][S] \qquad (7)$$

$$r_3 = \frac{k\alpha \mathrm{SSA}\tau\phi I}{1 + k\alpha \mathrm{SSA}\tau}\left(1 - e^{-\left(\frac{1}{\tau} + k\alpha \mathrm{SSA}\right)t}\right) \qquad (8)$$

$$1 \gg e^{-\left(\frac{1}{\tau} + k\alpha \mathrm{SSA}\right)t} : r_3 \cong \frac{k\alpha \mathrm{SSA}\tau\phi I}{1 + k\alpha \mathrm{SSA}\tau} \equiv r \qquad (9)$$

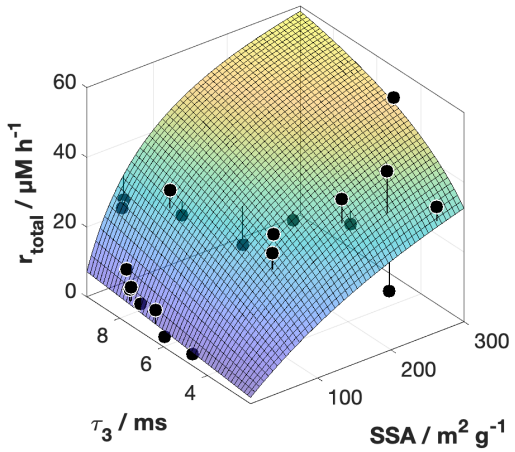

Figure 4. 3D surface plot of the model equation fitted to the experimental data. SSA and τ_3 were used as variables.

Table 3. Comparison of results of the non-linear curve fit using a kinetic equation with different variables[a]

Entry	Variable 1	Variable 2	R^{2b}	$R^2_{adjusted}{}^c$	Fitting parameters		
					$k\alpha$ / g m^{-2} h^{-1}	φ	τ / ms
1	SSA	τ_3	0.84	0.83	4.507×10^3	0.0093	-
2	SSA	τ_2	0.78	0.77	4.075×10^5	0.0061	-
3	SSA	τ_1	0.71	0.69	4.460×10^6	0.0063	-
4	SSA	-	0.78	0.75	6.074×10^4	0.0039	24.6
5[d]	τ_3	-	-	-	-	-	-

[a] The fitting was carried out using Curve Fitting Toolbox in MATLAB. [b] Sum of standard error. [c] Adjusted coefficient of determination. [d] The fitting cannot be carried out.

The reason why the long-living component (τ_3) gave the best fit can be quantitatively explained by calculating the steady-state concentration of photoexcited carriers for each component. The concentration of the long-living component ($[c_R^*]_3$) calculated from the model equation was orders of magnitude larger than that of the shorter-living species ($[c_R^*]_1$ and $[c_R^*]_2$) (Figure 5). This means that the total concentration of the excited reactive sites is determined mainly by $[c_R^*]_3$ (τ_3), explaining the reason why the use of τ_3 reproduced the results well.

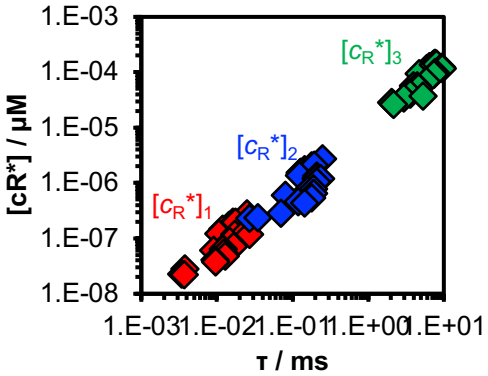

Figure 5. Relationship between carrier lifetime and the concentration of the excited reactive sites for each carrier lifetime. The concentrations of the excited reactive sites were calculated from eq. 9 with the parameters obtained from the non-linear regression analysis.

We also checked the validity of the values of the best-fit parameters (Table 3, entry 1, $k\alpha$ and φ) in a physicochemical sense. α (μM g m^{-2}), the saturated concentration of the adsorbed benzene per unit of specific surface area of anatase TiO_2, was calculated to be 135 by using the molecular size of benzene (0.5 nm) and assuming its monolayer adsorption with parallel adsorption geometry.[28] The second-order rate constant k (μM^{-1} h^{-1}) was calculated as 33.1 by dividing $k\alpha$ (4.507×10^3, Table 3, entry 1) by α. k would correspond to the rate constant of hole oxidation of benzene (eq. 2) since the oxidation would be more difficult than any latter steps of the reaction (eqs. 3 and 4). Unfortunately, a direct comparison of k with reported values is not feasible because of the absence of the reference value. Nevertheless, k is reasonably smaller than that of the oxidation of strong hole scavengers such as methanol or formaldehyde[29] although the measurement conditions such as time-resolution and the excitation laser power should also affect the rate constant. The intrinsic quantum efficiency φ is a representative value of the efficiency of photoabsorption of various anatase TiO_2 to produce photocarriers before the recombination in the microsecond region. Thus, 0.98% of φ (Table 3, entry 1) means that almost 99% of the carriers are lost before the recombination. When picosecond time-resolved measurements were carried out, 80–99% of free electrons were lost within 1 μs (Figure 6). This is in accordance with φ, considering the simplicity of the model used in the regression analysis (eq. 9). Therefore, the values of the fitting parameters seem reasonable in a physicochemical sense.

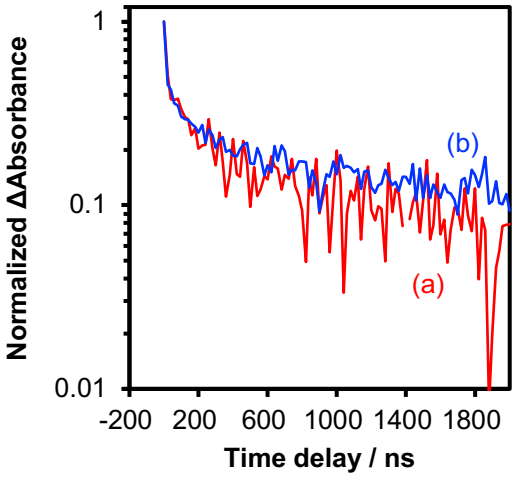

Figure 6. Transient absorption decays of free electrons in several anatase TiO_2 samples probed at 2000 cm^{-1}. (a) and (b) are ST-01_300C and ST-01_600C.

Interdependency between specific surface area and carrier lifetime

The model equation (eq. 9) quantitatively tells the interdependency between SSA and carrier lifetime; the effect of one parameter depends on another parameter. This interdependency is shown in Figure 7, which shows the predicted dependence of r_{total} on SSA at a fixed carrier lifetime (Figure 7A) and that on carrier lifetime at a fixed SSA (Figure 7B). The dependence on SSA or carrier lifetime can be different if the other parameter is different. The samples used in the reaction test have different SSA and carrier lifetime as shown in Table 1 and Figure 3. This necessitates the use of both SSA and carrier lifetime to explain their activity. The equation also tells that the role of SSA and carrier lifetime on the activity can be mathematically equal since the relation of each parameter to r is similarly given in a simple equation $y = bx / (1+ax)$, where x is SSA or τ. Therefore, the product of SSA and τ_3 (SSA•τ_3) can be used to describe their effects including the interdependency. The equation also reveals that the reaction rate has two extreme values depending on SSA•τ_3 (Figure 8). When SSA•τ_3 is sufficiently smaller than $1/k\alpha$, the reaction rate is distilled into $r_{lim,1} = k\alpha SSA\tau\varphi I$. In this case, the rate has a linear dependence on SSA and τ, which means the reaction is governed mainly by the surface reaction. In contrast, when SSA•τ_3 is sufficiently larger than $1/k\alpha$, the rate is distilled into $r_{lim,2} = \varphi I$; the reaction is controlled only by the photoabsorption process and no longer affected by the surface reaction. Requirements of SSA•τ_3 for $r_{lim,1}$ and $r_{lim,2}$ are calculated as SSA•$\tau_3 < 42$ and SSA•$\tau_3 > 15200$, respectively when the difference between r_{total} and each r_{lim} is within 5%. Note that these requirements are not universal in every photocatalytic reaction using anatase TiO_2 because $k\alpha$ depends on the reaction and the reaction condition (I), and carrier lifetime (τ) also does on its measurement condition. Most of the photocatalysts used in the present study do not fulfill the requirements, explaining the non-linear dependence of their activity on SSA•τ_3. In other words, SSA•τ_3 can be used as an indicator of the dependence of photocatalytic activity on specific surface area and carrier lifetime. The value of their product should be considered to compare the effects of SSA and carrier lifetime on activities of different photocatalysts and reactions since the effects can be linear, no-linear, and negligible depending on the value of the product.

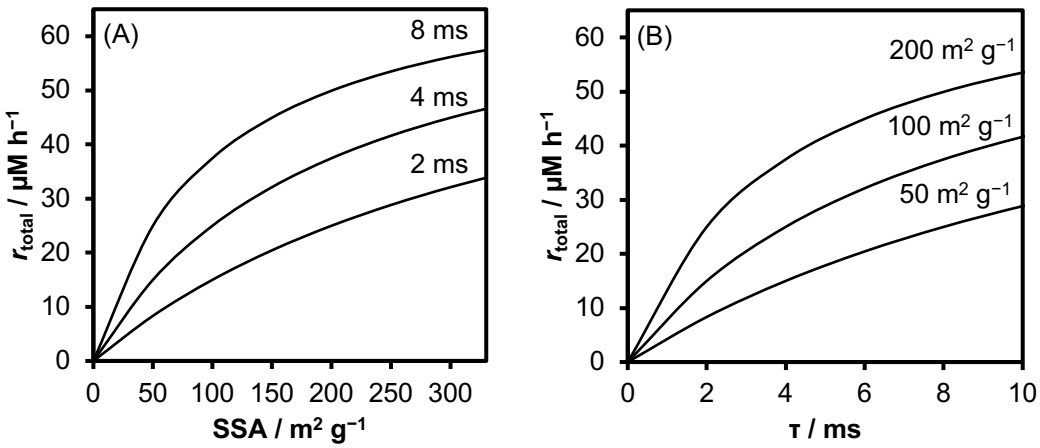

Figure 7. Predicted dependence of the total formation rate (r_{total}) on SSA at different carrier lifetime (A) and that on carrier lifetime at different SSA (B). The rate was calculated using eq. 9 with the fitting parameters in entry 3 in Table 3.

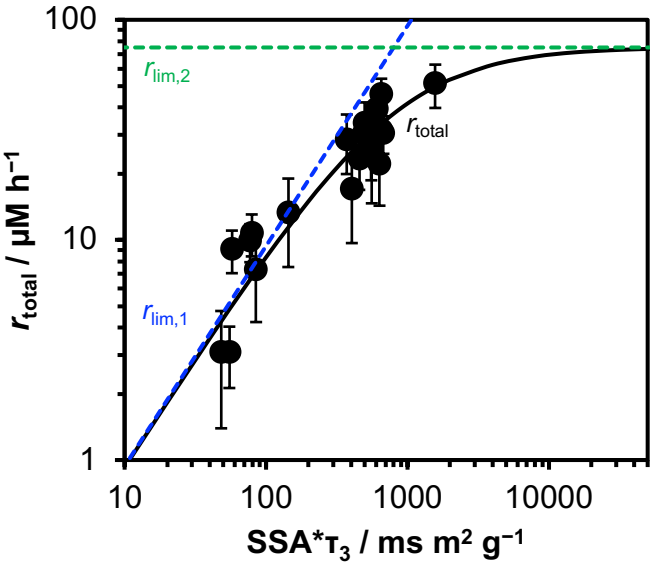

Figure 8. Log-log plot of the relationship between the total formation rate (r_{total}) and the product of specific surface area and carrier lifetime (SSA•τ_3) with two extreme values of r_{total}. Blue and green dotted lines are $r_{lim,1}$ and $r_{lim,2}$, respectively.

Since the model considers only three primary steps which are general in most photocatalytic reactions, it is expected to be applied to other photocatalytic reactions. In this regard, the present model has some issues to be overcome. One of the issues is the effect of light intensity. The model assumes the first-order dependence of the reaction rate on light intensity. This is not always the case especially when the target reaction involves multi-electron transfer processes such as oxidation of water into oxygen[30] and mineralization of organic pollutants into carbon dioxide.[31,32] In fact, the reaction in the present studies also requires two photons to complete the coupling and thus the second-order dependence of the reaction rate on light intensity would be expected. The reason why the present model can explain the results of

the present reaction would be low light intensity. The present study employed much lower light intensity (1.4 mW cm^{-2}) than that employed in most studies on photocatalysis (usually hundreds of mW cm^{-2} to W cm^{-2} order). In this low light intensity region, the difference between the first-order and the second-order dependence of the activity on light intensity would be negligible. Therefore, the model can be modified by changing the dependence of the reaction rate on the concentration of the excited sites ($[c_R^*]$) when much larger intensity of light is employed.

Conclusion

The quantitative relation of specific surface area and carrier lifetime to the activity of anatase TiO_2 photocatalysts is elucidated by a statistical approach based on a simple kinetic model. Activities of 21 anatase TiO_2 photocatalysts in dehydrogenative coupling of benzene were explained by a model equation that has SSA and carrier lifetime as variables. The model quantitatively explains the interdependency of the effects of specific surface area and carrier lifetime on the activity. The effects of the two factors including their interdependency can be distilled into the product of specific surface area and carrier lifetime. The product of SSA and carrier lifetime was proposed as a parameter to understand their different effects on the photocatalytic activity depending on the photocatalyst and reaction. The present study provides a model for a quantitative study on the structure-property-activity relationship in photocatalysis for the better design of efficient photocatalysts.

References

1. Gaya, U. I. & Abdullah, A. H. Heterogeneous photocatalytic degradation of organic contaminants over titanium dioxide: A review of fundamentals, progress and problems. *J. Photochem. Photobiol. C Photochem. Rev.* **9**, 1–12 (2008).
2. Rauf, M. A. & Ashraf, S. S. Fundamental principles and application of heterogeneous photocatalytic degradation of dyes in solution. *Chem. Eng. J.* **151**, 10–18 (2009).
3. Kumar, A. A Review on the Factors Affecting the Photocatalytic Degradation of Hazardous Materials. *Mater. Sci. Eng. Int. J.* **1**, 1–10 (2017).
4. Rivera, A. P., Tanaka, K. & Hisanaga, T. Photocatalytic degradation of pollutant over TiO_2 in different crystal structures. *Appl. Catal. B, Environ.* **3**, 37–44 (1993).
5. Palmisano, G., Augugliaro, V., Pagliaro, M. & Palmisano, L. Photocatalysis: a promising route for 21st century organic chemistry. *Chem. Commun.* **0**, 3425–3437 (2007).
6. Augugliaro, V. *et al.* TiO_2-Based Photocatalysis for Organic Synthesis. in *Environmentally Benign Photocatalysts: Applications of Titanium Oxide-based Materials* 623–645 (2010). doi:10.1007/978-0-387-48444-0.
7. Hoffmann, N. Photocatalysis with TiO_2 Applied to Organic Synthesis. *Aust. J. Chem* **68**, 1621–1639 (2015).
8. Friedmann, D., Hakki, A., Kim, H., Choi, W. & Bahnemann, D. Heterogeneous photocatalytic organic synthesis: state-of-the-art and future perspectives. *Green Chem.* **18**, 5391–5411 (2016).
9. Riente, P. & Noël, T. Application of metal oxide semiconductors in light-driven organic transformations. *Catal. Sci. Technol.* **9**, 5186–5232 (2019).
10. Kudo, A. & Miseki, Y. Heterogeneous photocatalyst materials for water splitting. *Chem. Soc. Rev.* **38**, 253–278 (2009).
11. Hisatomi, T., Takanabe, K. & Domen, K. Photocatalytic Water-Splitting Reaction from Catalytic and Kinetic Perspectives. *Catal. Letters* **145**, 95–108 (2015).
12. Takanabe, K. Photocatalytic Water Splitting: Quantitative Approaches toward Photocatalyst by Design. *ACS Catal.* **7**, 8006–8022 (2017).
13. Ni, M., Leung, M. K. H., Leung, D. Y. C. & Sumathy, K. A review and recent developments in photocatalytic water-splitting using TiO_2 for hydrogen production. *Renew. Sustain. Energy Rev.* **11**, 401–425 (2007).
14. Takata, T. *et al.* Photocatalytic water splitting with a quantum efficiency of almost unity. *Nature* **581**, 411–414 (2020).
15. Habisreutinger, S. N., Schmidt-Mende, L. & Stolarczyk, J. K. Photocatalytic reduction of CO_2 on TiO_2 and other semiconductors. *Angew. Chemie - Int. Ed.* **52**, 7372–7408 (2013).

16. Murakami, N., Kawakami, S., Tsubota, T. & Ohno, T. Dependence of photocatalytic activity on particle size of a shape-controlled anatase titanium(IV) oxide nanocrystal. *J. Mol. Catal. A Chem.* **358**, 106–111 (2012).
17. Almquist, C. B. & Biswas, P. Role of synthesis method and particle size of nanostructured TiO_2 on its photoactivity. *J. Catal.* **212**, 145–156 (2002).
18. Yamazoe, S., Okumura, T., Teramura, K. & Tanaka, T. Development of the efficient TiO_2 photocatalyst in photoassisted selective catalytic reduction of NO with NH_3. *Catal. Today* **111**, 266–270 (2006).
19. Tryba, B., Toyoda, M., Morawski, A. W., Nonaka, R. & Inagaki, M. Photocatalytic activity and OH radical formation on TiO_2 in the relation to crystallinity. *Appl. Catal. B Environ.* **71**, 163–168 (2007).
20. Amano, F., Nogami, K., Tanaka, M. & Ohtani, B. Correlation between surface area and photocatalytic activity for acetaldehyde decomposition over bismuth tungstate particles with a hierarchical structure. *Langmuir* **26**, 7174–7180 (2010).
21. Carneiro, J. T., Savenije, T. J., Moulijn, J. A. & Mul, G. Toward a physically sound structure-activity relationship of TiO_2-based photocatalysts. *J. Phys. Chem. C* **114**, 327–332 (2010).
22. Yamazaki, S., Fujiwara, Y., Yabuno, S., Adachi, K. & Honda, K. Synthesis of porous platinum-ion-doped titanium dioxide and the photocatalytic degradation of 4-chlorophenol under visible light irradiation. *Appl. Catal. B Environ.* **121**–**122**, 148–153 (2012).
23. Dozzi, M. V., Artiglia, L., Granozzi, G., Ohtani, B. & Selli, E. Photocatalytic activity vs structural features of titanium dioxide materials singly doped or codoped with fluorine and boron. *J. Phys. Chem. C* **118**, 25579–25589 (2014).
24. Nishimoto, Y., Hasegawa, Y., Adachi, K. & Yamazaki, S. Factors affecting oxygen evolution through water oxidation on polycrystalline titanium dioxide. *RSC Adv.* **6**, 46994–47000 (2016).
25. Paola, a. Di, Ikeda, S., Marcì, G., Ohtani, B. & Palmisano, L. Transition metal doped TiO_2: physical properties and photocatalytic behaviour. *Int. J. Photoenergy* **3**, 171–176 (2001).
26. Ikeda, S. *et al.* Photocatalytic activity of transition-metal-loaded titanium(IV) oxide powders suspended in aqueous solutions: Correlation with electron-hole recombination kinetics. *Phys. Chem. Chem. Phys.* **3**, 267–273 (2001).
27. Murakami, S. Y. *et al.* Evaluation of electron-hole recombination properties of titanium(IV) oxide particles with high photocatalytic activity. *Res. Chem. Intermed.* **33**, 285–296 (2007).
28. Raza, H., Wincott, P. L., Thornton, G., Casanova, R. & Rodriguez, A. Photoemission studies of the reaction of benzene with TiO_2(100)1 × 1 and 1 × 3. *Surf. Sci.* **402**–**404**,

710–714 (1998).
29. Dimitrijevic, N. M., Shkrob, I. A., Gosztola, D. J. & Rajh, T. Dynamics of interfacial charge transfer to formic acid, formaldehyde, and methanol on the surface of TiO_2 nanoparticles and its role in methane production. *J. Phys. Chem. C* **116**, 878–885 (2012).
30. Takeuchi, S., Takashima, M., Takase, M. & Ohtani, B. Digitally Controlled Kinetics of Titania-photocatalyzed Oxygen Evolution. *Chem. Lett.* **47**, 373–376 (2018).
31. Okamoto, K., Yamamoto, Y., Tanaka, H., Tanaka, M. & Itaya, A. Heterogeneous Photocatalytic Decomposition of Phenol over TiO_2 Powder. *Bulletin of the Chemical Society of Japan* vol. 58 2015–2022 (1985).
32. Wei, T. Y. & Wan, C. C. Heterogeneous Photocatalytic Oxidation of Phenol with Titanium Dioxide Powders. *Ind. Eng. Chem. Res.* **30**, 1293–1300 (1991).

Summary

In this thesis, the author studied TiO_2 photocatalysis for C–C bond formation.

Part I deals selective C–C bond formation through photoexcitation of surface complex. The studies attacked two issues in the surface complex system: low efficiency and the effect of multiple adsorbates. Potential use of the surface complex system for selective C–C bond formation was demonstrated.

In Chapter 1, selective dehydrogenative cross-coupling (DCC) between pyridine and cyclohexane was achieved through the LMCT excitation of the acid-base interacted surface complex consisting of pyridine and TiO_2. The reaction proceeds with high selectivity for a long time without polymerization, which takes place in the previous benzene system, and the yield reached 3.0% after 48 h. Several mechanistic studies suggested that the reaction is achieved by a unique reaction mechanism, in which a pyridine radical cation formed upon the LMCT excitation selectively oxidizes cyclohexane to a cyclohexyl radical for the subsequent radical addition and elimination between the radical and a pyridine molecule to complete the DCC. The potential of the heteroaromatic surface complex systems for selective DCC was demonstrated.

In Chapter 2, the author demonstrated that the use of H_2O_2 in the surface complex system successfully worked to improve both the selectivity and yield of Minisci-type functionalization of pyridine with tetrahydrofuran (THF). The use of visible light improved the selectivity by two times compared with that of UV light and the addition of the optimum amount of H_2O_2 increased the yield by 27 times under visible light. The yield under the optimized condition reached 34% after 31 h with the introduction of additional H_2O_2. DR UV-vis spectroscopy confirmed the formation of surface Ti-peroxo species upon a contact of H_2O_2 with TiO_2, which absorbs visible light to initiate the reaction. Reaction tests with several scavengers indicated that the active species is a hydroxyl radical produced by the reduction of H_2O_2 in the liquid phase by electrons excited from the peroxo species. They also suggested oxidation of H_2O_2 is suppressed under visible light irradiation, which would be due to the decomposition of the peroxo species prior to the oxidation, leading to higher selectivity under visible light than that under UV light. Generally, the photocatalysis with high concentration of reactive oxygen species (ROS) is efficient but unselective. The study provided a potential

approach to allow selective transformation of organic molecules by photocatalysis involving the generation of ROS.

In Chapter 3, the surface complex approach was used to achieve selective DCC between pyridine and benzene, both of which can form the surface complex with TiO_2. Adsorption tests suggested that pyridine preferentially adsorbs on the TiO_2 through the acid-case interaction, which is stronger than π interaction of benzene. This strong ability of pyridine to form the surface complex requires the use of the excess amount of benzene to promote the DCC selectively. The study demonstrated that the concentration of the substrates is a key to achieve selective DCC by the surface complex system in the presence of multiple adsorbates for the surface complexation.

In summary of Part I, the author demonstrated the potential of the surface complex system for C–C bond formation in a synthetic use, in which the selectivity can be improved just by changing the irradiation wavelength without any additives or modification of the photocatalyst.

Part II discusses the relationship between specific surface area (SSA), carrier lifetime, and photocatalytic activity of anatase TiO_2 nanoparticles.

In Chapter 4, the author identified SSA as an important factor affecting the energy states of photogenerated carriers in anatase TiO_2 nanoparticles. Time-resolved visible-to-midIR absorption spectroscopy revealed that in the microsecond region most electrons exist as free carriers when SSA is small (50 $m^2\ g^{-1}$), trapped carriers when SSA is large (308 $m^2\ g^{-1}$), and both free and trapped carries when SSA is middle (150 $m^2\ g^{-1}$). These different energy states in the microsecond region are determined by dynamics of photogenerated carriers in the picosecond region. The author also found that the lifetime of free electrons increased with decreasing SSA while that of trapped carriers is also be affected by other factors than SSA. Generally, the effect of SSA in photocatalysis is discussed in terms of the adsorption sites for the reactants. The study elucidated another aspect of SSA: a factor affecting the energy states of photogenerated carriers, which would also affect the photocatalytic activity.

In Chapter 5, the author proposed a generic model for a quantitative study on the relation of the activity of anatase TiO_2 photocatalysts to SSA and carrier lifetime, both of which are decisive factors of photocatalytic activity. The model reproduced well the activities of different anatase TiO_2 photocatalysts in dehydrogenative homo-coupling of benzene by using

SSA and carrier lifetime as variables. The model revealed that the effect of SSA and carrier lifetime on the photocatalytic activity can be mathematically equal. It also proposed the product of SSA and carrier lifetime as a quantitative indicator of their effects; the effects can be linear, nonlinear, or negligible depending on the value of the product, which is important to understand different effects of SSA and carrier lifetime depending on the material and the reaction.

In summary of Part II, the author demonstrated the clear relationship between SSA and the energy states of photoexcited carriers and the effectiveness of a statistical approach to elucidate the relation of multiple parameters with photocatalytic activity in a quantitative manner. The studies will help to comprehensively understand the structure-property-activity relationship in semiconductor photocatalysis for better design of efficient photocatalysts.

List of Publications

Part I

Chapter 1

1. Shimpei Naniwa, Akanksha Tyagi, Akira Yamamoto, and Hisao Yoshida
   Visible-light photoexcitation of pyridine surface complex, leading to selective dehydrogenative cross-coupling with cyclohexane
   Physical Chemistry Chemical Physics, 2018, **20**, 28375-28381.

Chapter 2

2. Shimpei Naniwa, Akira Yamamoto, and Hisao Yoshida
   Visible light-induced Minisci reaction through photoexcitation of surface Ti-peroxo species
   Catalysis Science & Technology, 2021, **11**, 3376-338.

Chapter 3

3. Shimpei Naniwa, Shinichiro Hishitani, Akira Yamamoto, and Hisao Yoshida
   Ligand-to-metal charge transfer of pyridine surface complex on TiO_2 for selective dehydrogenative cross-coupling with benzene
   Physical Chemistry Chemical Physics, 2021, **23**, 11366-11373.

Part II

Chapter 4

4. Shimpei Naniwa, Kosaku Kato, Akira Yamamoto, Hisao Yoshida, and Akira Yamakata
   Effect of specific surface area on the energy states of photoexcited carriers in anatase TiO_2 nanoparticles
   To be submitted.

Chapter 5

5. Shimpei Naniwa, Kosaku Kato, Akira Yamakata, Akira Yamamoto, and Hisao Yoshida
   A quantitative study on the relation of specific surface area and carrier lifetime to photocatalytic activity of anatase TiO_2 nanoparticles
   To be submitted.

Other publications

6. Akira, Yamamoto, Kazuya Arashiba, Shimpei Naniwa, Kazuo Kato, Hiromasa Tanaka, Kazunari Yoshizawa, Yoshiaki Nishibayashi, and Hisao Yoshida
Structural characterization of molybdenum-dinitrogen complex as key species toward ammonia formation by dispersive XAFS spectroscopy
Physical Chemistry Chemical Physics, 2020, **22**, 12368-12372.

※著作権等